Bauhaus-Universität Weimar

**Vibration-based Monitoring of Concrete Catenary Poles
using Bayesian Inference**

DISSERTATION

Zur Erlangung des akademischen Grades eines

Doktor-Ingenieur

an der Fakultät Bauingenieurwesen

der Bauhaus Universität Weimar

vorgelegt von

Feras Alkam

geboren am 08.05.1977

in Damaskus, Syrien

*This thesis is dedicated to my parents,
my family, and my uncle*

Acknowledgements

My deepest gratitude and appreciation go to my parents, my uncle, my small family (Lina, Marwan, Abd alrahman, Nour, and Hamza); my brother and sister; my family in law. I am grateful for their encouragement, prayers, and infinite support.

Weimar, 2020

Feras Alkam

Abstract

The use of electrified transportation is increasing, particularly regarding global efforts to mitigate greenhouse gas emissions that contribute to climate change and global warming. Questions regarding the integrity of catenary poles (used to carry the overhead electrified wiring for electrified transportation systems) still exist. This study contributes to verifying the characteristics of prestressed spun-cast concrete catenary poles that support the catenary system along high-speed train tracks. Using a stochastic uncertainty quantification framework, this work utilizes the concept of data fusion to optimize the use of data derived from multiple sources of data to verify the behavior of specified catenary poles in service. Three sources of data are used: measurements from experiments conducted on full-scale poles, detailed numerical models, and data recorded using the structural health monitoring system over four years. In this research, a Bayesian sensitivity-based parameter identification approach is newley developed to estimate the actual material properties of the poles using measurements from conducted experiments and numerical models. Implementation of this approach improved the quality of inferred parameters considerably. In addition, a vibration-based status monitoring approach is presented that traces the status of the pole over time. The proposed approach is characterized by ease of use and rapid application, because the required inputs can be derived using simple signal processing, or even using stochastic subspace identification techniques for more informative data. The approach utilizes the benefits of data fusion in merging the informative data from multiple sources and methods to increase the quality and accuracy of the expected results. Further, the proposed approach is introduced within a stochastic uncertainty quantification framework represented in the Bayesian inference, which quantifies the uncertainty resulting from different data sources and methods used in applying this approach. Consequently, the proposed approach and the algorithms achieve the aims of this research by creating a mechanism to trace the status of the poles and provide an alarm when damage occurs. Moreover, it identifies the location and severity of damage with acceptable accuracy, even in cases of high levels of noise.

Contents

List of Figures

LIST OF FIGURES

List of Tables

LIST OF TABLES

Acronyms

ACL   Alarm Control Limit.

CDF   Cumulative Distribution Function.

CDI   Curvature-based Damage Identification.

CI   Confidence Interval.

CoD   Coefficient of Determination.

COMAC   Coordinate Modal Assurance Criterion.

CR   Credible Region.

CSD   Cross-Spectral Density.

DD   Damage Detection.

DFG   Deutsche Forschungsgemeinschaft.

DFT   Discrete Fourier Transform.

DI   Damage Index.

DoE   Design of Experiments.

FBG   Fiber Bragg Grating.

FDI   Frequency-based Damage Identification.

FEM   Finite Element Method.

FFT   Fast Fourier Transform.

FRF   Frequency Response Function.

GRK1462   Research Training Group 1462.

IDT   Inductive Displacement Transducers.

iid   independent and identically distributed.

LHS   Latin Hypercube Sampling.

MAC   Modal Assurance Criterion.

MAP   maximum a posteriori.

MC   Monte Carlo.

MCMC   Markov Chain Monte Carlo.

MH   Metropolis-Hastings.

MLE	Maximum Likelihood Estimator.
ODE	Ordinary Differential Equation.
OMA	Operational Modal Analysis.
PDE	Partial Differential Equation.
PDF	Probability Distribution Function.
PI	Parameter Identification.
PoD	Predicted Coefficient of Determination.
PSD	Power Spectral Density.
QoI	Quantity of Interest.
RFID	Radio-frequency Identification.
RMSE	Root Mean Squared Error.
SA	Sensitivity Analysis.
SHM	Structural Health Monitoring.
SI	System Identification.
SM	Status Monitoring.
SSI	Stochastic Subspace Identification.
STFT	Short-Time Fourier Transform.
TMCMC	Transitional Markov Chain Monte Carlo.
UP	Uncertainty Propagation.
UQ	Uncertainty Quantification.
VTE	Versuchstechnische Einrichtung.
WCL	Warning Control Limit.
WT	Wavelet Transform.

List of Greek Symbols

$\boldsymbol{\alpha}$	The damage severity ratios.
$\hat{\alpha}$	The identified damage severity.
β	The factor β of the standard deviation σ_λ of the damage feature for defining ACL.
Γ_i^{ref}	The reserved extended stochastic controllability matrix.
$\emptyset$	The empty set.
ε_c	The concrete strain at maximum compressive stress.
ε_{PT}	The prestressing initial strain.
$\boldsymbol{\eta}$	The realizations of the total errors $\mathbf{E}$.
γ	The coherence function.
$\gamma^2(\omega)$	The coherence function.
λ	The eigenvalue of the system.
Λ	The eigenvalues matrix of the discrete-time system.
λ_d	The damage feature.
λ_{ck}	The eigenvalues of the continuous system.
λ_k	The eigenvalues of the discrete-time system.
μ_λ	The mean value of the damage feature.
μ_{PT}	The men value of the prestressing strains.
ν	The modal curvature.
ω	The set of possible outcomes of some random experiment.
ω_i	The ith un-damped natural frequencies of the system.
Ω	A sample measure space.
ϕ_i	The ith mode shape of the system.
ϕ_k	The mode shape of the continuous system.
π	The probability density.
Ψ	The eigenvector matrix.
ρ_c	The concrete density.

List of Greek Symbols

σ_λ	The standard deviation of the damage feature.
σ_{E}^2	The variance of the total errors.
σ_{PT}^2	The variance of the prestressing strains.
$\boldsymbol{\theta} \in \Theta$	The hyperparameters of the model.
$\boldsymbol{\vartheta}_a$	The local damages location measured from bottom of the pole.
$\hat{\vartheta}$	The identified damage location.
$\boldsymbol{\vartheta}$	The normalized damage locations.
v_k	The measurement noise.
w_k	The system noise.
$w(t - \tau)$	The time window.
$\boldsymbol{\xi} \in \mathcal{Z}$	The non-physical input parameters.
ζ_k	The damping ratio of the continuous system.

List of Latin Symbols

A	The system matrix of the discrete-time state-space model.
$\mathcal{B}$	Borel set.
C	The viscous damping matrix.
C	The output matrix of the discrete-time state-space model.
c_n	The spectral coefficients of Fourier transform.
$\boldsymbol{d} \in \mathcal{D}$	The well-known deterministic input parameters.
d_{bot}	The outer diameter at the bottom of catenary pole.
DI_i	The damage index of the ith mode.
d_{sn}	The normalized dimensionless distances of the sensors along the pole.
d_{sn}^a	The distances of the sensors along the pole.
d_{top}	The outer diameter at the top of catenary pole.
$\mathbb{E}$	The expectation value.
E_c	The concrete modulus of elasticity.
$f(t)$	The excitation force vector.
f	The natural frequencies of the pole.
$\mathcal{F}$	The set of observable sets of outcomes.
$F[x(t)]$	The Fourier transform of a signal $x(t)$.
f_{cm}	The compressive strength of concrete.
f_{ctm}	The tensile strength of concrete.
$\mathbf{f}_i^d$	The natural frequencies of the ith mode of the damaged pole.
$\Delta\mathbf{f}_i$	The relative natural frequencies of the ith mode of the damaged pole.
f_k	The natural frequency.
$\mathbf{f}_i^u$	The natural frequencies of the ith mode of the un-damaged pole.
$F^{-1}[X(\omega)]$	The inverse Fourier transform.
G	The next-state output correlation matrix.
$H(\omega)$	The Frequency Response Function (FRF).
$\mathcal{IG}$	The inverse gamma probability distribution.

List of Latin Symbols

K	The stiffness matrix.
$\mathcal{L}$	The likelihood function.
L	The length of the catenary pole.
M	The mass matrix.
$\mathcal{M}$	The forward model.
$\mathbb{N}$	The natural numbers.
$\mathcal{N}$	The Gaussian probability distribution.
O_i	The extended observability matrix.
$\mathbf{P}$	A probability measure.
$\mathbb{R}$	The real numbers.
R_i	The output covariance with time lag $i\Delta t$.
$S(z)$	The Sigmoid function.
$\tilde{S}$	The change of Sigmoid indices.
$\tilde{S}_i^d$	The Sigmoid indices of the damaged pole.
$\tilde{S}_i^u$	The Sigmoid indices of the un-damaged pole.
$S_{xx}(\omega)$	The Power Spectral Density (PSD) of a signal $x(t)$.
$S_{yx}(\omega)$	The Cross-Spectral Density (CSD) of signals $x(t)$, $y(t)$.
$\mathrm{T}_{1\|i}^{ref}$	The block Toeplitz matrix.
t_{bot}	The wall thickness at the bottom of catenary pole.
t_{top}	The wall thickness at the top of catenary pole.
$\mathcal{U}$	The uniform probability distribution.
w_{len}	The length of sliding window.
w_{sh}	The shift of sliding window.
$x(t)$	The vector of nodal displacement.
$\dot{x}(t)$	The vector of nodal velocity.
$\ddot{x}(t)$	The vector of nodal acceleration.
$\boldsymbol{x} \in \mathcal{X}$	The input parameters subjected to uncertainty.
$\mathbf{X}$	An input random variable.
x_k	A state vector that describes the system displacement and velocity.
$X(\omega)$	The frequency-domain of a signal $x(t)$ (spectrum).
$X(\tau, \omega)$	The time-frequency map (spectrogram).
$\mathbf{Y}$	An output random variable.
y_k	The measured output vector of the system.
$\tilde{\boldsymbol{y}}$	The realizations of random variables of the observations.
$\tilde{\boldsymbol{Y}}$	The random variables of the observations.
z	The Sigmoid variable.

Chapter 1

Introduction

1.1 Motivation

Today, electric transportation is one of the most promising solutions for mitigating the effects of greenhouse gas emissions that contribute to climate change and global warming [5, 6]. Besides their efficiency within the transportation system, electric trains are considered one of the most eco-friendly and safest means of transportation [7, 8].

With an increasing global trend for reliance on electric transportation, Siemens recently conducted a successful test of electrification of road freight. With the so-called eHighway system, Siemens combines the efficiency of electrified rail routes with the flexibility of trucks to create an innovative hybrid freight–transport solution: efficient, economical, and environmentally friendly [9].

In electrified transportation systems, the electrical power supply is secured by a *catenary system* installed along the transportation route. The catenary system ensures reliable and stable power transmission even at high speeds (such as $330\,\mathrm{km\,h^{-1}}$ in the case of the Intercity-Express (ICE) trains in Germany) [10]. Structural members known as catenary poles suspend the catenary system supplying electric trains, playing a vital role in the entire system, as any damage to one of these members leads to difficulties in the functionality of the whole system. Therefore, questions about their integrity are essential [11].

Catenary poles are used worldwide to support power transmission, telephone and telegraph lines, street lighting, and overhead power lines for electric trains. For many years, poles were made of wood, steel, and concrete [12]. Compared to other types of poles, the prestressed spun-cast concrete poles became a more feasible, cheaper option, with a longer operational life and lower lifetime costs [13, 14]. Recently, prestressed, spun-cast ultrahigh-strength concrete catenary poles have been used widely for electric train systems; for example, thousands of these poles have been installed along the high-speed train tracks

in Germany [3]. In addition, this type of poles has been discussed as an alternative to the current steel-lattice poles used in power transmission lines, in France, Denmark, the Netherlands, Italy, and Germany, even for extra-high voltage transmission [15, 16].

Structural Health Monitoring is a challenging field of science, especially in civil engineering, whereby important constructions are provided with monitoring systems that permanently update the status of these structures, as in the case of protected historical constructions. In addition, extending the operational lifetime of aging constructions means such systems are necessary, as in the case of many bridges around the world. Furthermore, attempts are being made to turn future constructions into so-called *smart structures* [17].

Working with SHM requires the combined efforts of several fields of science, such as System Identification (SI), Damage Detection (DD), signal processing, machine learning, Parameter Identification (PI), Uncertainty Quantification (UQ), and Design of Experiments (DoE) [18]. Despite significant development in this field, there is still much to be done. For instance, many methods have been developed for detecting and identifying damage to certain structures, but these are still inefficient for the DD process for other types of structures. One reason is that each civil structure has its own characteristic features, and is intensively affected by its environment, surrounding boundaries, constantly changing applied actions, material degradation, and more. The elements of interest in this study share some characteristics with *cantilever* structures, such as power transmission lines, antenna masts, chimneys, and wind turbines. However, they also have some distinctive characteristics such as the presence of prestressing forces that close any relatively small cracks that may appear [13].

For these reasons, insufficient attention has been paid to the behavior of catenary poles in the literature, particularly for those used to support train systems. Given the cost of installed poles and their importance to the functionality of these systems, further efforts are needed to verify the life cycle and changes in behavior of these structures. Moreover, a monitoring and early-warning algorithm is needed to track structural integrity over the lifespan, providing early warning when damage is expected.

1.2 Aim of the Work

The aim of this study is to develop an approach for monitoring cantilever structures. The pre-stressed, spun-cast ultrahigh-strength concrete catenary poles installed along high-speed train tracks is chosen as a case study. Monitoring requires poles to be classified into damage cases so that the location and severity of the detected damage can be identified after. Because of the vast number of poles that require monitoring, the proposed approach should be efficient and easy to apply. To build the necessary monitoring algorithm, the actual mate-

rial properties of the poles should be well known, achieved using the PI process, numerical modeling, and an experimental program. In addition, it is necessary to study the behavior of the un-damaged poles by analyzing the outputs of the SHM system attached to the poles on-site. To achieve the primary goal of this study, the following objectives are defined as follows:

1. To identify the actual material properties of the poles by developing a stochastic uncertainty quantification framework based on Bayesian inference, the measurements of multiple experiments, and finite element models.

2. To evaluate the existing status of the poles by implementing system identification using data recorded through an SHM system installed with three poles along the train track.

3. To develop a suitable monitoring algorithm for tracing changes in the behavior of the poles. The algorithm should distinguish between the changes caused by long-term material degradation and changes due to local damage to the pole.

4. To develop an appropriate stochastic damage identification algorithm that can localize the anticipated damage on the pole and determine the severity of the damage, which feeds the subsequent decision-making process with the required information to maintain or replace the damaged pole.

1.3   Outline of the Dissertation

To achieve the objectives of this study, this dissertation is structured into three main parts: the state of the art, the methodology and results, and conclusions and summary. In Part I, the background and literature review for this work are presented in Chapters 2 and 3. Part II contains the methodology, results, and discussion, presented in Chapters 4 to 8. Part III contains the summary and conclusion of this study, as well as future research, presented in Chapter 9.

Chapter 2 highlights the UQ and PI processes. The framework for UQ is detailed by defining the modeling concept of probability theory. The PI approach is explained by defining the concept of inverse problems and the methods available to solve them. Then, the Bayesian inference is introduced for solving PI within a stochastic UQ frame. In addition, different sampling approaches are described, such as the Metropolis-Hastings algorithm and Markov Chain Monte Carlo method.

Chapter 3 provides the background of DD, SHM, SI, and signal processing. This chapter begins by clarifying the concept of DD and the relevant methods for detecting and identifying

damage in civil structures monitored using SHM systems. This is followed by more in-depth information about the SI and vibration-based damage detection methods. Next, the concepts of time and frequency domains within the signal-processing framework is presented.

Chapter 4 focuses on the PI process and the proposed approaches for identifying the parameters of the structure of interest. This is followed by the proposed status detection approach. Mainly, three algorithms are proposed: status monitoring, frequency-based damage detection, and the curvature-based damage detection algorithms.

Chapter 5 begins by describing the case study used in this research together with a historical background of prestressed concrete poles and catenary poles. The experimental program and the experiments conducted within this work are also described. In addition, the SHM system attached to selected poles on-site is presented. In addition, the results of different experiments are analyzed and discussed, and details of the numerical modeling techniques and the material constitutive models used in this study are outlined.

In Chapter 6, data recorded by SHM system sensors is analyzed to establish the existing status of the poles over the specified time. Furthermore, SI is conducted using the data recorded by the attached accelerometers. Two approaches are utilized for analyzing the data: signal processing and Stochastic Subspace Identification techniques. Then, the results are summarized and discussed.

Chapter 7 discusses the implementation of the proposed approaches of PI using the measurements and numerical models of the poles. Moreover, the validation process of the methods is presented. This chapter should be read in conjunction with Chapters 2, 4 and 5.

In Chapter 8, the proposed status detection approach is implemented. Then, the results of each of the proposed algorithms are discussed. This chapter should be read in conjunction with Chapters 3 to 6.

Chapter 9 summarizes the outcomes of this study and presents thoughts regarding further research possibilities in the field of catenary poles and similar structures, namely in the direction of PI, DD, and SHM.

Part I

State of the Art

Chapter 2

Uncertainty in Engineering Models

2.1 Introduction

Uncertainty is a fascinating topic that spans many areas of our lives. The concept of uncertainty is discussed intensely in most science disciplines, such as, engineering, physics, economics, and decision theory [19]. Uncertainty is an aspect of our life that cannot be avoided and occurs because of the limited knowledge and inability to control factors that influence the phenomena around us [20]. The concept of uncertainty is closely associated with probability and the measure theory. It arises due to the limitation of the understanding of reality, and is represented by the probabilistic beliefs concerning the sources of uncertainty [21]. UQ is the framework that predicts the uncertainty at the given phenomenon or system.

2.2 Uncertainty Quantification Framework

Uncertainty Quantification is a very active research area that studies the impact of uncertainties on the prediction capabilities. Probability and the measure theory provide essential tools for the quantitative mathematical treatment of uncertainty [22]. In predictive science, UQ is defined as the process of identifying and quantifying the uncertainties associated with models, numerical algorithms, experiments, and their predicted outcomes or Quantity of Interest (QoI) [23].

In engineering science, the UQ process includes, but is not limited to, model verification and validation, parameter identification, and inverse problems [24, 25]. Implementing the UQ framework requires three essential pillars as shown in Fig. 2.1:

1. A pre-existing model that represents the system under consideration.

2. Identifying and quantifying sources of uncertainty that affects this system.

3. Once the inputs and their uncertainties are identified, Uncertainty Propagation (UP) transfers the uncertainty of the inputs into the measure of uncertainty in the outputs of the considered model.
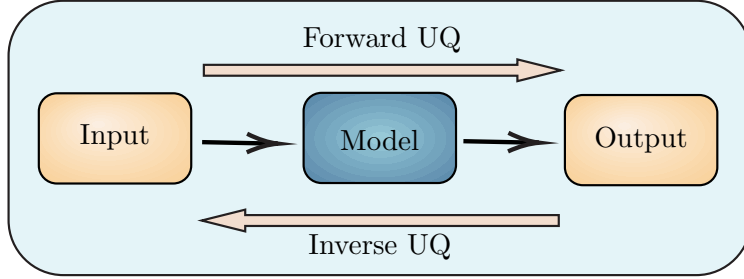
Fig. 2.1. Schematic UQ framework

However, applying UQ frameworks for large-scale applications requires a wide range of supporting topics and combines several advanced mathematical disciplines. This includes the theories of probability, statistics, and numerical analysis. This list can also extend to include the approaches of parameter identification, calibration, verification, and validation. Besides, UP requires additional techniques such as surrogate modeling, Sensitivity Analysis (SA), Monte Carlo (MC) simulation, Latin Hypercube Sampling (LHS), and more [24].

2.2.1 Probability Philosophy

The UQ can be understood as the association of probability theory and statistical practice with the real world. In other words, probability is the mathematical language for expressing the uncertainty. In this sense, a closer examination of the probability concept is needed for a deeper understanding of uncertainty [26].

Probability, in general, is related to the degree of belief that something is true. This is strongly related to the available information about the considered problem. Engineering society divides the information into two types: *objective* and *subjective*. The former is information based on experimental results or observations, whereas the latter is based on experience and data derived from similar problems [27]. This does not mean that *subjective* information is an *arbitrary* term. Different people may offer different information about a given problem, but when they update their beliefs, they will ultimately obtain a good agreement [28]. Consequently, we should distinguish here between two interpretations of statistical probability: Frequentism and Bayesianism [29].

Frequentists use the classical interpretation of *aleatory* (from Latin *alea*, meaning dice). Their interpretation of probability means the expected frequency over many repetitions of

Fig. 2.2. Confidence intervals (left) vs. credible region (right)

independent and identical experiments. Hence, they use objective information and consider unknown parameters to be deterministic and fixed. Parameters are *estimated* through statistical estimators, such as the Maximum Likelihood Estimator (MLE).

The frequentist approach evaluates the confidence in the estimator by using the Confidence Interval (CI). This means for a selected confidence interval, for example 95%, when repeating an event many times, and the 95% intervals are calculated each time, 95% of the cases of the computed confidence interval will contain the true value of the parameter x as illustrated in Fig. 2.2 (left). In this sense, additional steps are needed to propagate and quantify the parameter uncertainties [30].

In contrast, the Bayesian approach extends the probability interpretation to the degree of belief or certainty about a statement. Then, probability is subjective as it is related to their own knowledge about an event and can be updated as new data is available. This is sometimes called *epistemic* (from the Greek *epistẽmẽ*, meaning knowledge) or inverse probability.

In Bayesian inference, parameters are *inferred* in the form of probability densities, which reflect their uncertainties directly without any additional efforts. The basis of this approach is the law of conditional probability, or so-called *Bayes' rule*, which is explained in detail in Section 2.8.1. This combines subjective information (i.e., *a priori*), with the gained objective information from observations.

The Bayesian approach uses the Credible Region (CR) that is shown in Fig. 2.2 (right). This means that for the observed data of events, there is a 95% probability that the real value of the parameter lies within the credible region. This makes Bayesian probability closer to engineering thinking than that of the Frequentist approach [31].

2.2.2 Modeling Concept

Historically, the main goals of engineers and scientists have been to interpret, predict, and control natural and human-made systems. This usually involves the development of a reduced system, or so-called predictive *model*, that maps the given system using the data acquired through experience, experiments, and theories to explain the observations of the real system. The intention is for the model to link the output variables of the related system

causally, or the QoIs, to a set of input variables [19, 20].

Fig. 2.3 depicts the schematic flow chart of the modeling process. The first step is to build a conceptual model through *system abstraction*. In this step, the available information is collected to define and analyze the system, and to predict its behavior and performance [27]. In the next step, two types of models are built: first, the *physical* model, or so-called *experimental* model; and second the *computational*, or so-called *mathematical* model.
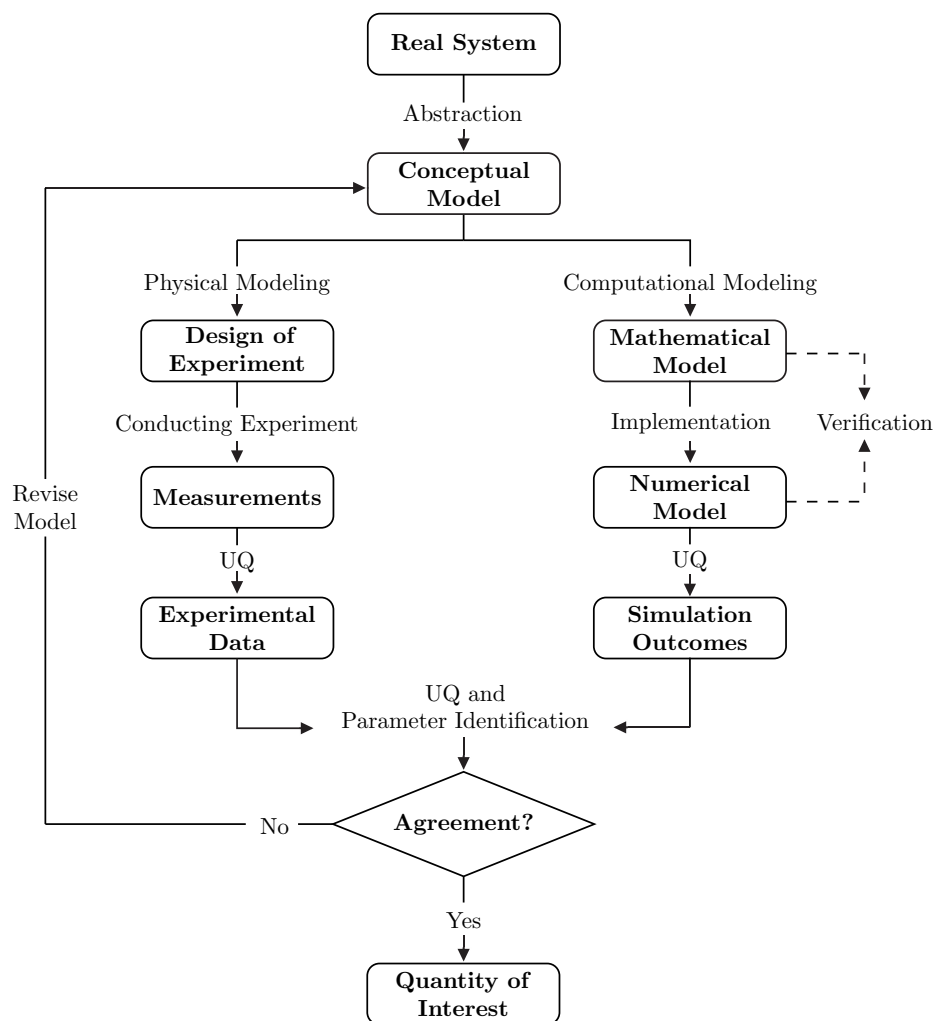
Fig. 2.3. Schematic flow chart of modeling [1].

The experimental model can be a reduced-scale model of the original system, or in some cases a full-scale model. Recently, it has become common to use the SHM systems that are attached to the real system on-site to trace its actual behavior. The *measurements* or *observations* are the outputs of the experimental model used to improve understanding of the system under investigation. Because the instruments are not perfect in most cases, more

uncertainties are added to the model.

In contrast, the computational model is usually built using mathematical functions, especially differential equations, and physical laws. This model represents the response of the physical system and includes materials, initial conditions, and the boundary condition of the system. It is quite common for these numerical approximations and solutions (such as the Finite Element Method (FEM)) to be used in these models. The *verification* process of the *numerical* models is essential to ensure that they represent the computational models with some uncertainties. Both the computational and numerical models need to be validated to the experimental models. The *validation* process indicates the degree to which the conceptual model represents the real system [1, 32].

Engineers, in most cases, build surrogate models to overcome the heavy computations of the numerical models. In this sense, regression models are good alternatives, and are widely used. However, regression models are verified against the results of numerical models to ensure their accuracy. This is done, for example, by calculating the Root Mean Squared Error (RMSE), the Coefficient of Determination (CoD), and the Predicted Coefficient of Determination (PoD). The type of regression model is selected based on the complexity and nature of the numerical model. In simple cases, the polynomial regression is used to create a linear or non-linear parametric regression model [33]. In more advanced cases, the non-parametric regression model is implemented, for example, [34], Extended Kalman filter [35], Polynomial Chaos [36], and Artificial Neural Networks (ANN) [37].

2.2.3 Uncertainty Sources

Identifying uncertainty sources is a challenging task, because of the lack of knowledge about the relevant system. Despite this, it is a fundamental task for understanding the impact of the uncertainties that affect the given system [28]. The uncertainties of the model arise from two sources: model discrepancies and uncertainties in the inputs.

At the level of the conceptual model, uncertainty propagates from limitations of the human perception of reality, and increases due to simplifications and abstractions of the real system. Experimental uncertainties can include (but are not limited to) human errors, limitation of the instruments and sensors, uncontrolled environmental conditions and errors of experimental setups. Numerical uncertainties originate from limitations of computational and numerical models, limitations in the accuracy of algorithms, numerical discretization, systematic and stochastic uncertainties of the input parameters, and approximation errors [23].

2.2.4 Uncertainty Types

There is no concept for classifying types of uncertainty. Based on causality, the uncertainty is classified into *forward* and *inverse* uncertainty quantification. The forward type is applied when the uncertainty of the inputs can be quantified and used to estimate the uncertainty of the outputs. The inverse uncertainty is essential when the uncertainties of the outputs are used to infer the uncertainties in the inputs [26].

When the uncertainty of a model is recognizable and quantifiable, the framework of probability mentioned above can be used efficiently to represent it. In this sense, it is common in engineering to divide the uncertainty into two main types: *aleatoric uncertainty* and *epistemic uncertainty* [38]. Aleatoric uncertainty describes the natural randomness of the given system and is usually defined in a probabilistic framework. It is inherited from the considered model and is, in principle, irreducible. In contrast, epistemic uncertainty is propagated due to the simplifications of the model and the lack of completed knowledge. In this regard, epistemic uncertainty can be reduced by enhancing new knowledge and expanding system resources [27].

Moreover, the UQ framework is usually solved using *deterministic* or *probabilistic* approaches. In the deterministic approach, linearization techniques (such as Markov estimator), are utilized to identify the uncertainty of the QoI. Furthermore, two *probabilistic* approaches are used to solve the UQ framework: the classical or Frequentist approach, and the Bayesian approach. The forward probabilistic approach describes uncertainty measures by transferring uncertainty in the inputs to the outputs using the probabilistic model. The Bayesian approach has a great advantage as it allows for consideration of the prior knowledge of the inputs [19]. For its efficiency, the Bayesian approach is used in this study to identify unknown parameters, and simultaneously to quantify the uncertainty.

2.3 Probability Theory

Let me begin with a brief review of measure theory and calculus-based probability. Such a fundamental review is essential for a better understanding of some terms, such as *random variables*, *moments*, and *density functions* [39, 40, 41].

The probability space is a triple $(\Omega, \mathcal{F}, \mathbf{P})$. Here, Ω is a sample measure space, or the set of possible outcomes $\omega \in \Omega$ of some random experiment. The σ-*algebra* $\mathcal{F} \subseteq 2^{\Omega}$ is defined as a set of subsets of Ω, called events, such that the subsets of Ω that includes Ω itself, is closed under complement, and is closed under countable unions. The event space $\mathcal{F}$ represents the set of observable sets of outcomes. Finally, $\mathbf{P}$ is a probability measure, also called a probability space, satisfies that probability of union of disjoint events being

equal to the sum of the correspondent events. The probability measure $\mathbf{P}$ assigns a number to each event contained in $\mathcal{F}$, for example, $\mathbf{P} : \mathcal{F} \to [0, 1]$ is a function on $\mathcal{F}$ with $\mathbf{P}(\emptyset) = 0$ and $\mathbf{P}(\Omega) = 1$, where $\emptyset$ is the empty set.

If we think of a sample space Ω as a set of all possible random outcomes of some experiment, then a random variable assigns a numerical value to each of these outcomes. Then, a random variable is a function $\mathbf{X} : \Omega \to \mathbb{R}$, such that

$$\{\omega \in \Omega; X(\omega) \leq x\} \in \mathcal{F}, \ x \in \mathbb{R}.$$

This is equivalent to saying that $\mathbf{X}^{-1}(B) \in \mathcal{F}$ for every Borel set $\mathcal{B}$, where Borel sets are the sets that can be constructed from open or closed sets by repeatedly taking countable unions and intersections. Then, for any Borel set $\mathcal{B}$, it is reasnoble to talk about $\mathbf{P}(X \in B)$, the probability that X lies in B. The *distribution* or *law* of X is the function μ defined on $\mathcal{B}$, the Borel subsets of $\mathbb{R}$, by

$$\mu(B) = \mathbf{P}(X \in \mathbf{B}) = \mathbf{P}(X^{-1}(B)), \ B \in \mathcal{B}.$$

Then, μ is the law of a random variable and $(\mathbb{R}, \mathcal{B}, \mu)$ is a valid probability triple, in other words, $X \sim \mu$, to indicate that μ is the distribution of X. Defining the Cumulative Distribution Function (CDF) of a random variable X by

$$F_X(x) = \ \mathbf{P}(X \leq x), \text{for } x \in \mathbb{R},$$

the function $\mathcal{F}$ is right-continuous and a non-decreasing function of x, with $\lim_{x \to \infty} F_X(x) = 1$ and $\lim_{x \to -\infty} F_X(x) = 0$.

Given a probability triple $(\Omega, \mathcal{F}, \mathbf{P})$ and X is a random variable having distribution μ, then, for any Borel-measurable function $f : \mathbb{R} \to \mathbb{R}$, the *expectation value* $\mathbb{E}(.)$ of the random variable X is defined as the Lebesgue integral, such that

$$\mathbb{E}_{\mathbf{P}}[f(X)] = \mathbb{E}_{\mu}(f) = \int_{\Omega} f(X(\omega))\mathbf{P}(d\omega) = \int_{-\infty}^{\infty} f(x)\mu(dx).$$

In other words, the expected value of the random variable $f(X)$ with respect to the probability measure $\mathbf{P}$ on Ω is equal to the expected value of the function f with respect to the measure μ on $\mathbb{R}$. For the continuous case, a Probability Distribution Function (PDF) π is similarly defined as a Borel-measurable function, such that $\pi > 0$ and $\int_{-\infty}^{\infty} \pi(x)dx = 1$, then

$$\mathbb{E}[f(X)] = \int_{-\infty}^{\infty} f(x)\pi(x)dx.$$

Similarly, the probabilities $P_X(B)$ can be also rewritten in a way involving the density function as $P_X(B) = \int_B \pi(x)dx$.

2.4 Predictive Model

2.4.1 Model Definition

For given input parameters $\boldsymbol{x} \in \mathcal{X}$ with a model parameter space $\mathcal{X} \subseteq \mathbb{R}^m$, the outputs of the predictive model are $\boldsymbol{y} \in \mathcal{Y}$ with an output space $\mathcal{Y} \subseteq \mathbb{R}^n$. Using a *forward operator* $\mathcal{G}$, the mapping from the input parameters $\boldsymbol{x}$ to the outputs $\boldsymbol{y}$ defines the *forward model* $\mathcal{M}$, such that

$$\begin{aligned} \mathcal{M} : \mathcal{X} &\to \mathcal{Y} \\ \boldsymbol{x} &\mapsto \boldsymbol{y} = \mathcal{G}(\boldsymbol{x}) \,. \end{aligned} \tag{2.1}$$

$\mathcal{G}$ is called a *function* when the inputs $\boldsymbol{x}$ and the outputs $\boldsymbol{y}$ are vectors [42]. This operator $\mathcal{G}$ can have different types, namely UQ, Partial Differential Equation (PDE) and their numerical approximation, or system of algebraic equations in a linear or nonlinear form. Here, Eq. (2.1) is appropriate for UQ through the deterministic framework [43].

Considering the probabilistic framework of the UQ, the input parameters $\boldsymbol{x}$ are modeled as random variables $\boldsymbol{X}$ that have the probability distribution $\mathbf{P_X}$ with PDFs $\pi(\boldsymbol{x})$. This means that the outputs $\boldsymbol{y}$ are also random variables $\boldsymbol{Y}$ that have the probability distribution $\mathbf{P_Y}$. Then, the model in Eq. (2.1) can be written as follows:

$$\begin{aligned} \mathcal{M} : (\mathcal{X}, \mathcal{B}(\mathcal{X}), \mathbf{P_X}) &\to (\mathcal{Y}, \mathcal{B}(\mathcal{Y}), \mathbf{P_Y}) \\ \boldsymbol{X} &\mapsto \boldsymbol{Y} = \mathcal{G}(\boldsymbol{X}) \,, \end{aligned} \tag{2.2}$$

this forward probabilistic model is illustrated in Fig. 2.4.

2.4.2 Model Imperfection

No mathematical model can perfectly represent the response of the real system. It is more convenient to rewrite Eq. (2.1) in this form: $\boldsymbol{y} = \mathcal{G}(\boldsymbol{x}) + \boldsymbol{\eta}_\mathcal{G}$, where $\boldsymbol{\eta}_\mathcal{G}$ represents the discrepancy between the model prediction and the real system.

Furthermore, in engineering applications, $\boldsymbol{y}$ represents the *'real'* observations of the given system, which practically cannot be measured due to the uncertainty of the experimental models and SHM systems. Then, the measured observation $\tilde{\boldsymbol{y}} = \boldsymbol{y} + \boldsymbol{\eta}_y$, where $\boldsymbol{\eta}_y$ is the discrepancy between the response of the real system and the measurands. Now Eq. (2.1)
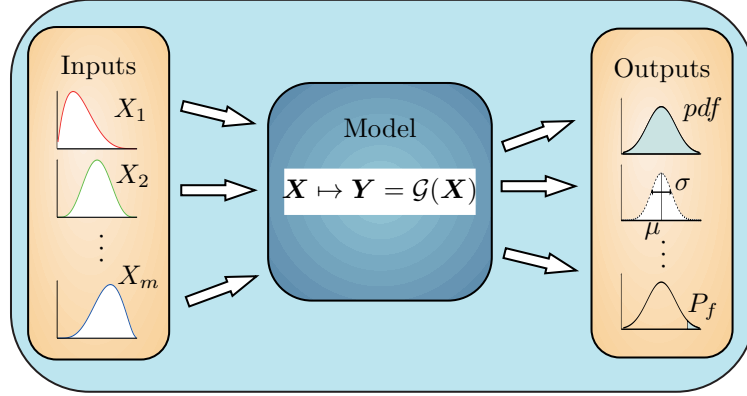
Fig. 2.4. A forward probabilistic model

can be written, such as

$$\tilde{\boldsymbol{y}} = \mathcal{G}(\boldsymbol{x}) + \boldsymbol{\eta}, \tag{2.3}$$

where $\boldsymbol{\eta} = \boldsymbol{\eta_y} + \boldsymbol{\eta_{\mathcal{G}}}$ is the total prediction error [44]. However, the researches widely cover the quantification of $\boldsymbol{\eta_y}$ and $\boldsymbol{\eta_{\mathcal{G}}}$, for example, [45, 46], which are not a part of this study.

2.5 Inverse Problems

2.5.1 Definition and Problems

In many engineering applications, the observations of the system $\tilde{\boldsymbol{y}} \subseteq \mathbb{R}^n$ can be measured without knowing their inputs $\boldsymbol{x} \subseteq \mathbb{R}^m$. In this case, given the forward operator $\mathcal{G}$ and the observations $\tilde{\boldsymbol{y}}$, the inputs to be inferred are such that Eq. (2.3) holds. This type of *inverse problem* is referred to by engineers as a PI process [47, 48].

Based on the number of observations n and the unknown inputs m, these inverse problems can be over-determined when $n > m$ or under-determined in case of $n < m$. In the former case, the solution of the inverse problem that satisfies all the outputs mostly does not exist [49]. In contrast, the uniqueness of the solution is the typical challenge of the latter case. Moreover, the sensitivity of the parameters plays a vital role in finding the solution of the inverse problem. The sensitivity makes the solution unstable, as a small change in the inputs $\boldsymbol{x}$ can lead to a significant change in the estimated model [22, 50].

The problem is considered as a *well-posed* problem if it fulfills the triple: existence, uniqueness, and stability. Practically, inverse problems are *ill-posed* as they mostly suffer from one or more of the three-mentioned causes. Solving inverse problems becomes harder due to imperfection of the model, uncertainties, and noisy measurements [43]. In the following sections, it is shown that one useful possibility to overcome these difficulties is to

utilize some informative priors. These regularization techniques are vital not only when using the deterministic framework, but also in the probabilistic framework, as in the Bayesian approach.

2.5.2 Deterministic Solution

Inverse problems can be solved using the least-squares approach, by minimizing the residuals between the observations and the model prediction. Then, the inferred parameters $\hat{\boldsymbol{x}}$ can be written as follows:

$$\hat{\boldsymbol{x}} = \underset{\boldsymbol{x} \in \mathcal{X}}{\operatorname{argmin}} \|\tilde{\boldsymbol{y}} - \mathcal{G}(\boldsymbol{x})\|_{\mathcal{Y}}^2 . \tag{2.4}$$

The *regularization* technique, (for example, Tikhonov regularization), can efficiently treat the ill-posedness of inverse problems by adding the prior knowledge of the input parameters $\boldsymbol{x}_0 \in \mathcal{V}$ with $\mathcal{V} \subseteq \mathcal{X}$ [42]. Then, the solution is derived by minimizing the function

$$\mathcal{J}(\boldsymbol{x}) := \|\tilde{\boldsymbol{y}} - \mathcal{G}(\boldsymbol{x})\|_{\mathcal{Y}}^2 + \alpha \|\boldsymbol{x} - \boldsymbol{x}_0\|_{\mathcal{V}}^2 , \tag{2.5}$$

where $\alpha > 0$ is the regularization coefficient, which can be determined using different methods, such as the L-curve method [50, 51].

Moreover, it is common in practice to re-weight the residuals using an operator $Q : \mathcal{Y} \to \mathcal{Y}$ such that Q is self-adjoint and positive-definite. By selecting the prediction error η in Eq. (2.3) to have zero mean, Q represents the covariance matrix of η. Similarly, a self-adjoint and positive definite operator $R : \mathcal{X} \to \mathcal{X}$ can be used to re-weight the regularization part of Eq. (2.5) [26]. This changes it into

$$\mathcal{J}(\boldsymbol{x}) := \left\|Q^{-1/2}(\tilde{\boldsymbol{y}} - \mathcal{G}(\boldsymbol{x}))\right\|_{\mathcal{Y}}^2 + \alpha \left\|R^{-1/2}(\boldsymbol{x} - \boldsymbol{x}_0)\right\|_{\mathcal{X}}^2 . \tag{2.6}$$

The inferred parameters $\hat{\boldsymbol{x}}$ are the minimizer of the function $\mathcal{J}$ in Eq. (2.6), such that

$$\hat{\boldsymbol{x}} = \underset{\boldsymbol{x} \in \mathcal{X}}{\operatorname{argmin}} \mathcal{J}(\boldsymbol{x}) . \tag{2.7}$$

2.6 Deterministic Approach of UQ

In the deterministic approach of UQ, parameters uncertainty is represented by the covariance matrix of the identified parameters $\hat{\boldsymbol{x}}$ by minimizing the residual part $\left\|Q^{-1/2}(\tilde{\boldsymbol{y}} - \mathcal{G}(\boldsymbol{x}))\right\|_{\mathcal{Y}}^2$ in Eq. (2.6). To evaluate the covariance matrix of the parameters, local sensitivities $s_i = \frac{\partial \widehat{\mathcal{G}}}{\partial x_i}$ are estimated by linearizing the nonlinear relation between the parameters and the observations at the optimal point, or the so-called *Markov estimator* [52, 53].

Confidence in the parameters is proportional to the entries on the main diagonal of the so-called *Fisher information matrix* or *sensitivity matrix* M. Then, the higher the value of M, the higher the confidence [33].

$$M := \sum_{i=1}^{m} \widehat{\mathcal{G}}'(\boldsymbol{x}_i)^T \ Q^{-1} \ \widehat{\mathcal{G}}'(\boldsymbol{x}_i) \,, \tag{2.8}$$

where Q is the covariance matrix of the observations. It can also be estimated by the inverse of the information matrix M^{-1}, and applying Cramér-Rao-Inequality, the so-called *variance-covariance matrix*

$$C \succeq \left(\sum_{i=1}^{m} \widehat{\mathcal{G}}'(\boldsymbol{x}_i)^T \ Q^{-1} \ \widehat{\mathcal{G}}'(\boldsymbol{x}_i) \right)^{-1} \,, \tag{2.9}$$

the symbol $\succeq$ is understood in the sense of $A \succeq B$ if $x^T A x \geq x^T B x, \ \forall x$.

Then, the CIs of the parameters are proportional to the diagonal entities C_{ii} of the covariance matrix C [54]. Then, the probability exists that

$$| \, x_i^{exact} - x_i^{computed} \, | \leq \sqrt{C_{ii}\chi_m^2(1-\alpha)}, \ i = 1, \cdots, m \tag{2.10}$$

is larger than $(1-\alpha)$, where $\chi_m^2(1-\alpha)$ denotes the $(1-\alpha)$ of the χ_m^2 probability distribution. The smaller the right-hand side of Eq. (2.10) the more reliable the identified parameter can be assumed [55].

2.7 Classical Probabilistic Approach of UQ

The Frequentist approach mostly uses the MLE to estimate the unknown parameters. To define the *likelihood function*, the observations are considered as a random variable $\boldsymbol{Y} = \{Y_1, \cdots, Y_n\}$ associated with the PDFs $\pi_Y(\boldsymbol{y}; \boldsymbol{x})$, where $\boldsymbol{y} = \{y_1, \cdots, y_n\}$ are the realizations of $\boldsymbol{Y}$. The unknown parameters $\boldsymbol{x}$ are considered as real numbers. Hence, the uncertainty of the estimated parameters $\hat{\boldsymbol{x}}$, which are likely close to $\boldsymbol{x}$, are evaluated using the CIs, as mentioned before in Section 2.2.1. The likelihood function $\mathcal{L}$ is defined such that

$$\mathcal{L}_y(\boldsymbol{x}) = \mathcal{L}(\boldsymbol{x}|\boldsymbol{y}) = \pi_Y(\boldsymbol{y}; \boldsymbol{x}) \,. \tag{2.11}$$

Assuming random variables $\boldsymbol{Y}$ to be independent and identically distributed (iid), the likelihood function in Eq. (2.11) is estimated as follows:

$$\mathcal{L}(\boldsymbol{x}|\boldsymbol{y}) = \prod_{i=1}^{n} \pi_{Y_i}(y_i; \boldsymbol{x}). \tag{2.12}$$

The unknown parameters are considered, from the Frequentist point of view, as the parameters that make the observed data more likely [51]. They are the maximizer of the likelihood function

$$\hat{\boldsymbol{x}}^{MLE} = \underset{\boldsymbol{x} \in \mathbb{R}^m}{\mathrm{argmax}} \, \mathcal{L}(\boldsymbol{x}|\boldsymbol{y}). \tag{2.13}$$

Practically, it is more convenient to deal with log-likelihood $\ln\mathcal{L}(\mathrm{x}|\mathrm{y})$. Equivalently, the estimated parameters $\hat{\boldsymbol{x}}^{MLE}$ are the maximizer of the $\ln\mathcal{L}(\mathrm{x}|\mathrm{y})$ such that

$$\hat{\boldsymbol{x}}^{MLE} = \underset{\boldsymbol{x} \in \mathbb{R}^m}{\mathrm{argmax}} \, \ln\mathcal{L}(\mathrm{x}|\mathrm{y}). \tag{2.14}$$

Now, the MLE is incorporated to solve the inverse problem of Eq. (2.3) by assuming the random variables of the errors $\mathbf{E}$ to be iid. $\mathbf{E}$ is associated with a selected PDF $\pi_{\mathrm{E}}(\boldsymbol{\eta}; \boldsymbol{\theta}_{\mathrm{E}})$ that depends on the error parameters $\boldsymbol{\theta}_{\mathrm{E}}$ and has a zero-mean $\mathbb{E}(\boldsymbol{\eta}) = 0$; for example, $\mathrm{E} \sim \mathcal{N}(0, \boldsymbol{\sigma}_\eta^2)$. Then, the likelihood function $\mathcal{L}$ in the Eq. (2.12) can be written as follows:

$$\mathcal{L}(\boldsymbol{x}|\tilde{\boldsymbol{y}}, \boldsymbol{\theta}_{\mathrm{E}}) = \prod_{i=1}^{n} \pi_{\mathrm{E}}(\tilde{y}_i - \mathcal{G}_i(\boldsymbol{x}); \boldsymbol{\theta}_{\mathrm{E}}), \tag{2.15}$$

and this equation plays a vital role in solving the probabilistic inverse problems for both the Frequentist and the Bayesian frameworks [56].

2.8 Bayesian Approach for Uncertainty Quantification

2.8.1 Bayes Theorem

Let $(\Omega, \mathcal{F}, \mathbf{P})$ be a probability space. *Bayes' rule* defines the conditional probability that a proposition $A \in \mathcal{F}$ occurs, given that a proposition $B \in \mathcal{F}$ occurred such that

$$\mathbf{P}(A|B) = \frac{\mathbf{P}(B|A) \cdot \mathbf{P}(A)}{\mathbf{P}(B)}, \text{ for } \mathbf{P}(B) > 0. \tag{2.16}$$

In this sense, the Bayesian framework includes a degree of belief through the term $\mathbf{P}(A)$, which is named the *prior*. The term $\mathbf{P}(B|A)$ is a function that quantifies the *likelihood* of event B's occurrence, given that A is true. The *posterior* density $\mathbf{P}(A|B)$ quantifies the

degree of belief having accounted for B. Eq. (2.16) forms the main core of Bayesian inference [57].

2.8.2   Bayesian Inverse Problems

The Bayesian approach, as a probabilistic framework of the UQ, overcomes the difficulties of solving inverse problems by considering the stochastic model of Eq. (2.3) such that [22]

$$\tilde{\boldsymbol{Y}} = \mathcal{G}(\boldsymbol{X}) + \mathbf{E}\,. \tag{2.17}$$

This is achieved by considering the observations as random variable $\tilde{\boldsymbol{Y}} \in \mathbb{R}^n$, which has the probability distribution $\mathbf{P}_{\tilde{Y}}$ with a PDF $\pi(\tilde{\boldsymbol{y}}) > 0$. The unknown parameter $\boldsymbol{X} \in \mathbb{R}^m$ is a random variable with a prior density $\pi_X(\boldsymbol{x}) = \pi_0(\boldsymbol{x})$. The error $\mathbf{E} \in \mathbb{R}^n$ is a random variable that is mutually independent of $\boldsymbol{X}$ and has a probability distribution $\mathbf{P}_{\mathrm{E}}$ with an appropriate density $\pi_{\mathrm{E}}(\boldsymbol{\eta})$ [58]. The joint probability density $\pi(\boldsymbol{x}, \tilde{\boldsymbol{y}})$ is defined as follows:

$$\pi(\boldsymbol{x}, \tilde{\boldsymbol{y}}) = \pi(\tilde{\boldsymbol{y}}|\boldsymbol{x}) \cdot \pi_0(\boldsymbol{x})\,.$$

Now, as in Eq. (2.16), the posterior probability distribution of $\boldsymbol{X}$ given the observed data $\tilde{\boldsymbol{Y}}$ is written such that

$$\pi(\boldsymbol{x}|\tilde{\boldsymbol{y}}) = \frac{\pi(\boldsymbol{x}, \tilde{\boldsymbol{y}})}{\pi(\tilde{\boldsymbol{y}})} = \frac{\pi(\tilde{\boldsymbol{y}}|\boldsymbol{x}) \cdot \pi_0(\boldsymbol{x})}{\pi(\tilde{\boldsymbol{y}})}\,. \tag{2.18}$$

Thus, Eq. (2.18) shows the four-pillars for solving inverse problems in the Bayesian approach: the *posterior* $\pi(\boldsymbol{x}|\tilde{\boldsymbol{y}})$, the *likelihood* $\pi(\tilde{\boldsymbol{y}}|\boldsymbol{x})$, the *evidence* $\pi(\tilde{\boldsymbol{y}})$, and the *prior* $\pi_0(\boldsymbol{x})$.

The prior density $\pi_0(\boldsymbol{x})$ represents any available knowledge of the system before the data are collected. This can be retrieved from similar systems or prior experience. However, it is recommended to use a *non-informative prior* (sometimes called a *vague prior*), such as uniform density and *Jeffreys'* prior, unless good prior information is available, as the posterior density can be strongly deviated by using the incorrect prior.

Nevertheless, the prior can be built into a hierarchical model based on the observed data. In this case, the unknown parameters $\boldsymbol{x}$ are modeled conditionally on unknown *hyper-parameters* $\boldsymbol{\theta}_X$ of a given probabilistic distribution $\pi(\boldsymbol{\theta}_X)$, which makes the prior to be $\pi_0(\boldsymbol{x}; \boldsymbol{\theta}_X)$ and increases the number of inferred parameters [59]. Substituting this prior in Eq. (2.18) gives

$$\pi(\boldsymbol{x}, \boldsymbol{\theta}_X|\tilde{\boldsymbol{y}}) = \frac{\pi(\tilde{\boldsymbol{y}}|\boldsymbol{x}, \boldsymbol{\theta}_X) \cdot \pi_0(\boldsymbol{x}, \boldsymbol{\theta}_X)}{\pi(\tilde{\boldsymbol{y}})}\,. \tag{2.19}$$

Additionally, choosing a *conjugate prior*, that is, assigning a prior density $\pi_0(\boldsymbol{x})$ such that the posterior $\pi(\boldsymbol{x}, \boldsymbol{\theta}_X|\tilde{\boldsymbol{y}})$ belongs to the same distribution family that contains the prior,

has the practical advantage of making the results more understandable and computationally more convenient [60].

The likelihood $\pi(\tilde{\boldsymbol{y}}|\boldsymbol{x})$ is a function of $\boldsymbol{y}$ with $\boldsymbol{x}$ fixed. To evaluate this, the Bayesian approach utilizes the concept of maximum likelihood from the Frequentist approach. This means that the specifications of the likelihood are based on the error model, see Eq. (2.3), which leads to $\pi(\tilde{\boldsymbol{y}}|\boldsymbol{x}) := \pi(\tilde{\boldsymbol{y}} - \mathcal{G}(\boldsymbol{x}))$, in other words $\pi(\tilde{\boldsymbol{y}}|\boldsymbol{x}) \equiv \mathcal{L}(\boldsymbol{x}|\tilde{\boldsymbol{y}})$. Thus, the approach in Section 2.7 can be utilized here [61].

The denominator of Eq. (2.18), the so-called evidence, is independent of $\boldsymbol{x}$ and represents the probability density of $\tilde{\boldsymbol{y}}$ for all values of $\boldsymbol{x}$. Hence, it is considered as a normalization constant and evaluated by the integral over all the possible joint densities of $\tilde{\boldsymbol{y}}$ such as

$$\pi(\tilde{\boldsymbol{y}}) = z = \int_{\mathbb{R}^m} \pi(\tilde{\boldsymbol{y}}|\boldsymbol{x}) \cdot \pi_0(\boldsymbol{x}) \mathrm{d}\boldsymbol{x} \,. \tag{2.20}$$

As a result, the posterior in Eq. (2.18) is written as a statement of proportionality as follows:

$$\pi(\boldsymbol{x}|\tilde{\boldsymbol{y}}) \propto \pi(\tilde{\boldsymbol{y}}|\boldsymbol{x}) \cdot \pi_0(\boldsymbol{x}) \,. \tag{2.21}$$

Finally, the posterior density $\pi(\boldsymbol{x}|\tilde{\boldsymbol{y}})$ is a probability distribution that provides the full information of the unknown parameters $\boldsymbol{x}$, based on the observations $\boldsymbol{y}$. In some case studies, when only the statistical moments are required, for example, the mean and the variance, as QoIs. Here, keep in mind that the normalization constant z should be included to have the right values of QoIs. In other cases, the *maximum a posteriori* (MAP) estimator $\hat{\boldsymbol{x}}^{MAP}$ or *mode* as statistically named is quantified. MAP represents the values of inferred parameters with the highest probabilities of occurrence,

$$\hat{\boldsymbol{x}}^{MAP} = \operatorname*{argmax}_{\boldsymbol{x} \in \mathbb{R}^m} \pi(\boldsymbol{x}|\tilde{\boldsymbol{y}}) \,, \tag{2.22}$$

and in this case, there is no need to calculate the normalization factor z [57].

One of the challenges of the Bayesian approach is extracting information from the posterior. Any parameter can be inferred directly through the marginalization of the posterior over the rest of the parameters as follows:

$$\pi(x_i|\tilde{\boldsymbol{y}}) = \int \pi(\boldsymbol{x}|\tilde{\boldsymbol{y}}) \mathrm{d}\boldsymbol{x}_{\sim i} \,, \tag{2.23}$$

where $\boldsymbol{x}_{\sim i} = (x_1, \cdots, x_{i-1}, x_{i+1}, \cdots, x_m)$ denotes the parameters except x_i. In most cases, this cannot be solved analytically without using other simplification methods, such as asymptotic approximation [62]. Stochastic sampling routines can be utilized here to approx-

imate this integral by sampling from the probability distribution in question, for example, the MC integration, and importance sampling [37].

This becomes more difficult with higher dimensional probability distributions. Then, the alternatives are the Markov Chain Monte Carlo (MCMC) algorithms. These are very efficient in drawing the parameter distributions from the posterior, even those that are complex and high-dimensional. To achieve this, the forward problem needs to be solved many times, which makes this approach computationally expensive [36].

2.8.3 Markov Chain Monte Carlo

The MCMC method combines the Markov chain and MC integration for constructing chains whose stationary distribution is the posterior. The densities of parameters based on the observations are the realizations of the Markov chain. The MCMC uses the concept of MC sampling and an acceptance criterion to build the Markov chain. The samples are drawn from a proposed simpler distribution $\pi^*(\boldsymbol{x})$. Then, they randomly move through the parameter space to explore the regions of high probability. Moving between states $\boldsymbol{x}_j$ and $\boldsymbol{x}_{j+1}$ is defined based on the jumping distribution $q(\boldsymbol{x}_{j+1}|\boldsymbol{x}_j)$ that depends only on the current state $\boldsymbol{x}_j$ [57, 63].

Many different MCMC algorithms have been developed over in recent years. Most are mainly based on the probability of proposing the future state, for example, Metropolis-Hastings (MH), Gibbs sampling, and Slice sampling. Unlike these algorithms, Hamiltonian/Hybrid Monte Carlo (HMC) adopts physically dynamic system based on Hamiltonian dynamics in propagating the Markov chain. This allows the Markov chain to sample the target distribution much more efficiently than other probability-based algorithms, which results in faster convergence. However, the HMC requires the careful tuning of internal parameters to decrease its computational cost, which makes it less popular [64].

2.8.4 Metropolis-Hastings

Because of its efficiency and simplicity, MH is a widely-used algorithm for sampling from the posterior distribution of unknown parameters. MH is based on random-walk that starts from some random initial state x_0 drawn from initial condition distribution π_0. The algorithm uses a transitional distribution q, or so-called *random walk kernel*, to randomly move to a proposed state x^*, given a current state [65].

Samples from the proposal distribution are not accepted automatically as posterior samples. MH utilizes the concept of rejection sampling to reject or accept the proposed state x^* with probability $\alpha = \min(1, r)$. This denotes $\alpha = 1$ if $r \geq 1$ and with probability $\alpha = r$ if $r < 1$, where r is the probability ratio, as shown in Algorithm 1. This means that the

algorithm does not always move uphill towards the higher probability, but also goes downhill to avoid being stuck in the local maximums. Simultaneously, the entire posterior density is explored [66].

Algorithm 1 Metropolis-Hastings (MH) algorithm [56]

1: specify the number of the chain elements N_s
2: generate an initial state $\boldsymbol{x}_0 \sim \pi_0$
3: **for** $j = 1, \cdots, N_s$ **do**
4:     generate a proposal state $\boldsymbol{x}^* \sim q(\boldsymbol{x}|\boldsymbol{x}_{j-1})$
5:     calculate the acceptance ratio

$$r = \frac{\pi(\boldsymbol{x}^*|\tilde{\boldsymbol{y}})q(\boldsymbol{x}_{j-1}|\boldsymbol{x}^*)}{\pi(\boldsymbol{x}_{j-1}|\tilde{\boldsymbol{y}})q(\boldsymbol{x}^*|\boldsymbol{x}_{j-1})}$$

6:     calculate the acceptance probability $\alpha = \min(1, r)$
7:     sample $u \sim \mathcal{U}(0, 1)$
8:     **if** $(u \leq \alpha)$ **then**
9:         accept $\boldsymbol{x}^*$, set $\boldsymbol{x}_j = \boldsymbol{x}^*$
10:     **else**
11:         reject $\boldsymbol{x}^*$, set $\boldsymbol{x}_j = \boldsymbol{x}_{j-1}$
12:     **end if**
13: **end for**

Most often, the multivariate Gaussian distribution is selected as a proposal jumping distribution, namely, $q(\boldsymbol{x}^*|\boldsymbol{x}_{j-1}) \sim \mathcal{N}(\boldsymbol{x}_{j-1}, \Sigma_q)$, where the covariance matrix Σ_q defines the jumping length [35].

2.8.5   Analysis of resulting MCMC Chain

For any MCMC method, the resulting chain to be inspected by answering some questions, such as how to choose the appropriate jumping step; does the resulting chain have a stationary distribution that coincides with the posterior density; when can the chain be considered as converged and when to stop the algorithm; and what is the degree of correlation between the accepted samples.

It is crucial for the MH algorithm to assign an appropriate value to the size of the random walk; that is, the variance σ^2. The optimal step size depends strongly on the geometry of the target posterior. Increasing the value of the step size ends with rejecting many candidates x^*, where assigning a small value produces stagnation and makes the algorithm too slow. Most of the literature advises optimization of the step size to get an acceptance ratio of between 0.2 and 0.5. This also quantifies whether the algorithm is adequately sampling from the posterior [23, 57].

Assessing the convergence, or *burn-in*, of the MH algorithm is very important to assure that the resulting chain has a stationary distribution. Theoretically, this can mainly be reached within a sufficient large number of iterations, which is computationally demanding. One of the methods of checking the stationarity and adequacy of the chain length is to rerun the algorithm several times using different starting points. Consequently, the results can be visually or statistically compared. In this method, the initial samples within the burn-in period should be excluded when computing the parameter densities. Another method of analyzing convergence is with statistical tests; for example, the Geweke, or Gelman and Rubin tests, which are implemented in CODA library in R program [67].

The MCMC supposes that the resulting chain is a Markov chain. To assure this, and knowing that the samples of the MH algorithm are not entirely random, the autocorrelation of the samples should be checked. This can be reduced by eliminating some samples,namely by retaining the kth sample of the produced chain, or so-called *thinning*. However, the autocorrelation is inversely proportional to the convergence and the step size [43, 68].

Despite the efficiency of the MH algorithm to draw the posterior density, it is valid only for evaluation of the first level of Bayesian inference. To evaluate the hierarchical Bayesian models and overcome the drawback of the MH algorithm mentioned previously, more advanced algorithms can be utilized. These include, but are not limited to, Gibbs sampling, Nested sampling, reversible jump Markov Chain Monte Carlo (RJMCMC), and Transitional Markov Chain Monte Carlo (TMCMC) [64].

2.8.6 Transitional Markov Chain Monte Carlo

Among MCMC algorithms, the TMCMC is a widely used algorithm for solving both levels of the Bayesian inference, for example, parameter identification, model selection, and model averaging problems. Because of its high efficiency, it is popular in engineering practice and inspiring in the research field [64]. The TMCMC algorithm overcomes many of the MH drawbacks that were mentioned in Section 2.8.5. Compared to the standard MH algorithm, drawn posterior density using TMCMC has better quality with a smaller number of samples. Besides, TMCMC is suitable for sampling from multiple models, estimating the evidence of the Bayesian model class. It also overcomes the difficulty of sampling from complex models [69]. These reasons offer motivation to utilize the TMCMC algorithm in this study.

The TMCMC adopts the idea of using a series of intermediate PDFs, proposed by Ching and Chen [70], to sample the posterior in sequence by reweighting and resampling the samples from each intermediate PDF. Instead of directly sampling from the target density, TMCMC starts sampling from the prior $\pi_0(\boldsymbol{x})$. Then, in each of the following steps, it uses intermediate PDFs until the posterior density $\pi(\boldsymbol{x}|\tilde{\boldsymbol{y}}) = \pi^J(\boldsymbol{x})$ is gradually reached

---

Algorithm 2 Transitional Markov Chain Monte Carlo (TMCMC) algorithm [70, 72]

1: specify the number of the chain elements N_s

2: at $j = 0$ generate N_s samples at the initial state $\{\boldsymbol{x}_{(0,1)}, \cdots, \boldsymbol{x}_{(0,N_s)}\} \sim \pi_0$, set $j = 1$

3: **while** $p_j < 1$ **do**

4:      optimize p_j such as $p_j = \mathrm{argmin}_p \left(|c.o.v.\{\mathcal{L}(\boldsymbol{x}_{(j,n_s)}|\tilde{\boldsymbol{y}})^{(p-p_{j-1})}\}_{n_s=1}^{N_s} - \nu| \right),$

5:          $p \in (p_{j-1}, 1]$, $\nu = 100\%$, If $p_j > 1$, then set $p_j = 1$

6:      **for** $n_s = 1, \cdots, N_s$ **do**

7:          compute the weighting coefficients $\omega_{(j,n_s)} = \mathcal{L}(\boldsymbol{x}_{(j-1,n_s)}|\tilde{\boldsymbol{y}})^{(p_j-p_{j-1})}$, and the

8:              normalized weights $\tilde{\omega}_{(j,n_s)} = \frac{\omega_{(j,n_s)}}{\sum_{n_s=1}^{N_s} \omega_{(j,n_s)}}$

9:          compute the mean of the weighting coefficients $S_j = \frac{1}{N_s} \sum_{n_s=1}^{N_s} \omega_{(j,n_s)}$

10:          compute the covariance matrix of the Gaussian proposed distribution

$$\Sigma_j = \beta^2 \sum_{n_s=1}^{N_s} \left(\tilde{\omega}_{(j,n_s)}(\boldsymbol{x}_{(j-1,n_s)} - \bar{\boldsymbol{x}}_j) \cdot (\boldsymbol{x}_{(j-1,n_s)} - \bar{\boldsymbol{x}}_j)^T \right)$$

11:          where the user scale factor $\beta = 0.2$, and $\bar{\boldsymbol{x}}_j = \sum_{n_s=1}^{N_s} \tilde{\omega}_{(j,n_s)} \cdot \boldsymbol{x}_{(j-1,n_s)}$

12:          **for** $l = 1, \cdots, N_s$ **do**

13:              set the candidate $\boldsymbol{x}_{(j,l)}^* = \boldsymbol{x}_{(j-1,l)}$

14:              randomly samples from the set $\boldsymbol{x}_{(j-1,n_s)}$ with probability $\tilde{\omega}_{(j,n_s)}$, i.e.,

15:              $\boldsymbol{x}_{(j,l)}^* = \boldsymbol{x}_{(j-1,n_s)}$

16:              **for** $k = 1, \cdots, N_s$ **do**

17:                  sample $\boldsymbol{x}^* \sim \mathcal{N}(\boldsymbol{x}_{(j,l)}^*, \Sigma_j)$

18:                  sample $u \sim \mathcal{U}(0,1)$

19:                  if $u \leqslant \frac{\pi^j(\boldsymbol{x}^*)}{\pi^j(\boldsymbol{x}_{(j,l)}^*)}$ then set $\boldsymbol{x}_{(j,l)}^* = \boldsymbol{x}^*$, otherwise do nothing

20:                  set $\boldsymbol{x}_{(k,n_s)} = \boldsymbol{x}_{(j,l)}^*$, set $\omega_{(j,l)} = \mathcal{L}(\boldsymbol{x}_{(j,l)}^*|\tilde{\boldsymbol{y}})^{(p_j-p_{j-1})}$

21:              **end for**

22:          **end for**

23:      **end for**

24:      set $j = j + 1$

25: **end while**

26: estimate the evidence $\hat{z} = \prod_{j=1}^{m} S_j$

---

[71]. In each step, a new Markov chain of samples is initiated from each of the previous samples set using the MH algorithm. This is achieved using the random walk approach, assuming a Gaussian proposal PDF centered at the current sample. The covariance matrix is estimated by importance sampling using the samples of the previous step [70]. The proposed transitional PDFs are written such that

$$\pi^j(\boldsymbol{x}) \propto \pi_0(\boldsymbol{x}) \cdot \mathcal{L}(\boldsymbol{x}|\tilde{\boldsymbol{y}})^{p_j}, \tag{2.24}$$

where $p_j \in [0,1]$ and the step number $j = 0, \cdots, J$. The total number of the steps J is reached when $p_J = 1$. The value of p_j is optimized, such that the coefficient of variation of $\mathcal{L}(\boldsymbol{x}|\tilde{\boldsymbol{y}})^{(p_{j+1}-p_j)} \simeq \nu$, where ν is a user-defined threshold. However, some important modifications and improvements were added to the original TMCMC algorithm, such as adjusting the sample weights, improving the burn-in period, and adjusting the acceptance rate [73, 72]. The TMCMC algorithm is summarized in Algorithm 2.

Chapter 3

Damage Inspection and Diagnosis

3.1 Introduction

The integrity of civil structures is usually maintained by periodic inspection procedures that aim to detect any deterioration that might occur. Thus, this guarantees adequate safety of the structure. By detecting deterioration at an early stage, repair procedures can be performed on structures instead of demolition or replacement [74, 75]. Furthermore, some existing structures are subject to higher load levels than they were designed for, as in the case of increasing traffic loads on old bridges. Inspection practices lead to an increase in the operational life span of structures, which has a significant economic impact, especially in the case of infrastructure systems [76].

Inspection practices are generally divided into *destructive* and *non-destructive*. However, destructive practices are avoided when possible for civil structures. Non-destructive practices include (but are not limited to) visual inspection, acoustic emissions, ultrasound, magnetic particle, and radiography testing [77]. These methods are mostly efficient for the inspection of deterioration within a localized area referred to as *local* damage [78]. Techniques such as classical visual inspection practices can be subjective, costly, time-consuming, and require trained experts, making them inefficient as a means of identifying invisible damage [79]. In contrast, *vibration-based* practices work well for identifying *global* deterioration, which makes it one of the promising methods in civil engineering, principally in the field of DD [80, 81]. However, a combination of both practices is recommended, where vibration-based practice is used for detecting and localizing the damage, and other non-destructive practices can be used to verify the location and evaluate the severity of the damage [82].

Global vibration-based inspection practices verify the integrity of a structure, from changes in its dynamic response to either service actions or an artificially introduced excitation. Using SHM in conjunction with vibration-based damage detection approaches provides

an efficient approach in the field of damage detection [83]. In addition, vibration-based inspection is an attractive inspection practice for detecting both global and local deterioration of systems, as local damage mostly leads to a change in dynamic characteristics of the structure, which in turn can be an indicator of damage [84].

3.2 Damage Detection of Structures

Techniques for DD have been widely developed and implemented to assure the integrity of structural and mechanical systems such as aircraft, rotating machinery, offshore platforms, and bridges. In structural systems, damage is generally defined as changes to properties of a given system that adversely affect its performance (such as changes to the properties of materials, geometry, and boundary conditions) [74]. Damage inspection is hierarchically classified into four levels: damage detection (Level 1), damage localization (Level 2), quantifying damage severity (Level 3), and predicting the remaining life of the structure (Level 4) [84, 85].

It is common for the DD process to work in conjunction with closely related disciplines such as SHM, statistical process control, and non-destructive practices to detect the onset of damage or deterioration as early as possible so that the integrity of the system under consideration can be maintained. Unlike temporally applied, traditional non-destructive evaluation methods, SHM systems have become more popular and efficient for providing real time inspection of civil structures. This is because of the rapid development of diagnosis and classification techniques such as data-driven, machine learning and computer vision techniques [86].

3.2.1 Structural Health Monitoring

The SHM system is based on a data acquisition system that periodically samples response measurements from an array of sensors attached to the structure being monitored. Then, the data interpretation process is achieved using diagnostic techniques. The structural condition is assessed to evaluate the integrity of the structure, localize and quantify possible damages, and take subsequent prevention actions, as well as to predict the remaining service life of the structure.

Operational Modal Analysis (OMA), as a particular example of experimental modal analysis, has been used extensively for identifying modal parameters of systems in engineering. Compared to experimental modal analysis, OMA has some advantages that make it more pertinent for use in civil engineering [87, 88, 89]. When using OMA, the complete structure of interest is tested under real operational conditions using ambient excitation

without the need for artificial excitation, which makes OMA suitable for output-only iden-
tification of the system. Moreover, due to the natural presence of ambient excitation, OMA
is ideally suited to continuous monitoring of the system such as that used in vibration-based
SHM and DD of civil structures. However, OMA also has drawbacks; for example, it is not
efficient in low ambient excitation cases, and mode shapes derived using this method are
unscaled [90, 91].

Based on data provided by the SHM system, two approaches of DD processes are defined:
supervised and *unsupervised*. In the supervised approach, both the healthy and damaged
states of the structure of interest are known, and are consequently used to classify the state
of the structure based on newly recorded data. In civil engineering, it is most probable
that the unsupervised approach is used, as the available data describes only one class; that
is, the healthy state. In this case, any deviation from the healthy state of the structure
under monitoring is considered a change in its response and is consequently classified as a
damaged state [92].

Based on the nature of diagnostic techniques, DD processes are classified into *data-based*,
and *model-based* techniques. However, using a combination of both in a *hybrid* technique
offers the advantages of each whilst providing efficient cover for the four levels of the DD
process [93]. The data-based approach identifies the state of the structure of interest us-
ing tools such as signal processing and modern statistical tools. In the field of DD using
signal-processing techniques, methods have been introduced based on vibration's signals
from sensors, empirical mode decomposition, and Hilbert-Huang transformation. These
methods are mostly able to detect damage at Level 1 and in some cases at Level 2, which is
insufficient for many practical applications [94]. Conversely, modern statistical tools (such
as auto-regression models, machine learning, artificial neural networks, and Gaussian pro-
cesses) train the data to build statistical models or *patterns* that represent possible states
of the concern structure [95, 96]. Then, the state of the structure is identified using pat-
tern recognition algorithms in supervised cases [97, 98]. In addition, algorithms like novelty
detection [99], outlier analysis [100], control chart methods [101, 102], and principal com-
ponent analysis (PCA) [103] are used for unsupervised cases. Besides the excessive time
needed in the data training process, modern statistical approaches are capable of practically
handling the DD at Levels 1–4, but only for supervised cases where both healthy and dam-
aged patterns of the structure are known; for example, in the field of aircraft and rotary
machines. However, in civil engineering damage patterns are usually unavailable, which
limits the efficiency of data-based approaches in this field to cover only the most basic level
of DD. Efforts are being made to extend efficiency so that the second level is also covered,
whereas the four levels of DD are well-covered using model-based techniques [104].

3.2.2 System Identification

System Identification as a model-based DD technique is an inverse process of estimating the dynamic characteristics of a structure using an appropriate model (commonly a FEM) and measurements recorded by an SHM system, such as strain gauges and accelerometers [105, 106]. To begin, in a step called *damage feature extraction*, a set of damage features is defined by choosing dynamic characteristics of the structure of interest that are highly sensitive to its damaged condition [92]. Next, the set of selected damage features are identified; for example, modal parameters such as natural frequencies, damping ratios and mode shapes. These results are subsequently used to evaluate model parameters such as stiffness matrix, mass matrix, and material properties of the structure [80]. Up to this point, one loop of a *model updating* process is made. Successive loops are achieved using periodically recorded measurements derived, for example, using an SHM system [107, 108].

The SI processes work in either a *frequency* or a *time* domain. The choice of the domain is highly dependent on the nature of the problem, the dynamic characteristics to be identified, and the availability of input and output measurements. For instance, input-output methods are less attractive in the case of large civil structures where the input is unknown [84]. Among the different methods that have been developed in both domains, the most practical and relevant methods for this study are discussed. Frequency domain methods are principally based on the relation between the input and output PSD of a random process [109]. However, the Frequency Domain Decomposition (FDD) method can only be used in output-only cases. In this method, the Singular Value Decomposition (SVD) of the output PSD in different frequencies is used as the mode indicator function. Besides the simplicity and speed of application, this method works well with noisy data and close modes [110]. In the time domain, subspace-based methods for identifying the state-space of systems has gathered significant attention in civil engineering. From these methods, SSI methods use the output-only measurements of a system subjected to stochastic excitation in an operational situation [111]. Practically, two SSI approaches are used: *data-driven* SSI, and *covariance-based* SSI. However, both approaches perform equally well concerning modal parameter estimation performance [112].

In any system, inputs and outputs are required to identify its dynamic characteristics during the SI process. However, determining the inputs for civil structures is often a difficult task because these kinds of structures are usually subjected to environmental actions (such as wind and ambient temperature), or varying loads (such as traffic loads on bridges). In addition, it is difficult to excite such structures due to their large scale. Therefore, much effort has been given to the development of output-only SI methods, which provides reliable estimates of the dynamic characteristics of civil structures using only outputs of their system

under ambient vibration and random environmental actions [113].

3.2.3 Uncertainty Quantification in Damage Detection

Each step involved in solving the DD problem has a level of uncertainty, such as the uncertainty and noise of SHM measurements, and the discrepancy of models used in the SI process. Therefore, UQ plays a significant role in the DD process and the subsequent decision-making phase. As discussed in Section 2.8, Bayesian inference is an efficient approach for solving the ill-posed inverse problems using noisy data and various sources of uncertainties, which makes it a powerful approach to DD, SHM, and SI. For instance, Bayesian parameter estimation is used in the domain of structural vibration-based parameter estimation [79, 114], and in the fields of OMA and SHM as a probabilistic uncertainty approach [115, 116] for model selection of linear and nonlinear dynamical systems [117], in the domain of DD and model updating [118, 44, 119]. In addition to the already mentioned approaches, Bayesian inference is a vital tool in the probabilistic *data fusion* field of study [120, 121]. Data fusion combines information from multiple sources (such as multiple sensors or methods) to enhance the efficiency of the damage detection process [74, 122]. For instance, the Bayesian data fusion is used for integrating different kinds of sensors and multiple damage features in DD problems [123, 124, 125].

3.3 Damage Modal Features

Modal parameters have been used intensively in global vibration-based approaches for solving DD problems. The basic idea is to track changes in the dynamic characteristics of the structure of interest and use these changes to detect possible damage. A significant amount of existing literature presents different DD methods based on modal damage features; for example, methods are built based on changes in natural frequencies, modal damping, mode shapes and their derivatives, modal strains, modal flexibility, and modal strain energy [80, 81, 92, 126, 127]. Each of the presented methods has some limitation based on certain factors; for example, the sensitivity of the given system to the damage feature, the location and severity of damage to be detected, the noise level, and the number and type of sensors used in the attached monitoring system. The following discussion focuses on the damage modal features based on the output-only, vibration-based approach of DD. The methods most relevant to this research are duly presented.

The vibration of a viscously damp, linear structural system with N degrees of freedom

is represented using the equation of motion such that:

$$[M]\{\ddot{x}(t)\} + [C]\{\dot{x}(t)\} + [K]\{x(t)\} = \{f(t)\}, \tag{3.1}$$

where $[M]$ is the mass matrix, $[C]$ is the viscous damping matrix, and $[K]$ is the stiffness matrix. The vectors of nodal displacement, velocity, and acceleration are represented by $x(t), \dot{x}(t)$, and $\ddot{x}(t)$, respectively. Term t is the time, and $f(t)$ is the excitation force vector. The matrices and vectors have an order of N in size, corresponding to the number of degrees of freedom used in describing the displacements of the structure.

The eigenvalue equation of an un-damped system of the ith mode is given as follows:

$$(-\lambda_i[M] + [K])\{\phi_i\} = \{0\}, \tag{3.2}$$

where $\lambda_i = \omega_i^2$ is the eigenvalue, and ω_i represents the un-damped natural frequencies of the system. Term $\{\phi_i\}$ is the eigenvector, or the ith mode shape of the system. Damage in the system of interest leads to a change in the stiffness matrix $[K]$ and/or the mass matrix $[M]$. Accordingly, dynamic characteristics (such as natural frequencies and mode shapes) are changed. Such a change is the essence of the vibration-based DD process.

3.3.1 Natural Frequencies

The DD based on changes in the natural frequencies of systems, is one of the first methods used in the vibration-based DD domain. Compared to other modal features, natural frequencies are easy to measure using fewer sensors and greater precision. In addition, they are less sensitive to location and smaller measuring errors. However, this method mostly identifies Level 1 damage only. Moreover, they are sensitive to the noise level and the effects of environmental actions on the given system [126, 81]. Recently, this method has regained the interest of some researchers. For example, environmental and operational influences on natural frequencies can be eliminated using kernel principal component analysis [128]. Furthermore, using Bayesian data fusion of multiple natural frequencies leads damage detection to Level 1, with slightly less efficiency to Level 2 of DD [129]. Besides, shifts in multiple natural frequencies provide spatial information about structural damage, because changes in structure at different locations cause different combinations of changes in modal frequencies [108].

3.3.2 Mode shapes

Compared to natural frequencies, mode shapes contain spacial information and are less influenced by environmental effects, which makes them an excellent candidate for detecting

damage at Level 2 [130]. This is usually achieved using Modal Assurance Criterion (MAC) values, which measure the correlation between the modal shapes of the system in two states to detect the damage at Level 1 when MAC values differ significantly from unity [92]. The MAC values are calculated as follows [131]:

$$MAC\left(\{\phi_i^u\}, \{\phi_j^d\}\right) = \frac{\left|\{\phi_i^u\}^T\{\phi_j^d\}\right|^2}{\left(\{\phi_i^u\}^T\{\phi_i^u\}\right)\left(\{\phi_j^d\}^T\{\phi_j^d\}\right)}, \tag{3.3}$$

where, $\{\phi_i^u\}$ and $\{\phi_j^d\}$ are the vector of measured mode shapes i^{th} and j^{th} of two different states of the structure of interest, namely, the un-damaged state u, and the damaged state d.

The concept of MAC has been extended to Coordinate Modal Assurance Criterion (CO-MAC), which verifies the correlation between modal displacements at measured degrees of freedom. This extends the validity of this method to detect damage at Level 2. The CO-MAC value of the qth degree of freedom and k number of measured mode shapes is written such that [131]

$$COMAC\left([\phi^u], [\phi^d], q\right) = \frac{\left(\sum\limits_{i=1}^{k}\left|(\phi_i^u)_q(\phi_i^d)_q\right|\right)^2}{\left(\sum\limits_{i=1}^{k}\left(\phi_i^u\right)_q^2\right)\left(\sum\limits_{i=1}^{k}\left(\phi_i^d\right)_q^2\right)}. \tag{3.4}$$

The COMAC values differ considerably from unity when comparing the damaged and un-damaged state of a system. However, this method depends strongly on the quality of measured modal displacements, the noise level, and the number of sensors used to measure the response of the system of interest.

3.3.3 Modal Curvature

It is proven that the DD process is more sensitive to derivatives of the modal displacements, such as the modal curvature, than the modal displacements themselves. The modal curvature ν is the second derivative of the modal displacement ϕ. Having an array of sensors attached to the structure of interest at equally-distributed spaces $\Delta\vartheta$, the modal curvature $(\nu_i)_p$ at coordinate p is numerically estimated using the second-order central difference approximation [132]:

$$(\nu_i)_p = \frac{(\phi_i)_{p-1} - 2(\phi_i)_p + (\phi_i)_{p+1}}{\Delta\vartheta}, \tag{3.5}$$

where $(\phi_i)_{p-1}, (\phi_i)_p$, and $(\phi_i)_{p+1}$ are the measured modal displacements at three subsequent coordinates. However, to use modal curvatures for DD, the modal displacements need to be calculated with as much coordinates on the structure of interest as possible. In addition, this method is sensitive to noisy measurements compared with other methods. Therefore, the modal curvatures are optimal for damage localization at a low level of noise [82]. It is recommended that another feature is used (such as natural frequencies) to detect the damaged state, then the modal curvatures feature is the right candidate for localizing the damage [127, 133]. Moreover, it is noted that using data fusion techniques to merge the results of multiple measured modes can improve the quality of the modal curvature approach considerably [125].

3.4   Stochastic Subspace Identification Method

Excitation is usually considered as white noise in the output-only linear system in civil engineering. Given a discrete-time system with sampling interval Δt, the subspace model can be written as follows [111]:

$$
\begin{aligned}
x_{k+1} &= \mathrm{A}x_k + w_k \\
y_k &= \mathrm{C}x_k + v_k \,,
\end{aligned}
$$
(3.6)

where x_k is a state vector that describes the system displacement and velocity at the instant $k\Delta t$, and y_k denotes the measured output vector. Terms w_k and v_k represent the system and measurement noise, respectively. Thus, SSI solves the system by identifying the system matrix A and the output matrix C form the output-only data, as it is shown later. Then, the modal parameters of the system are derived from the eigenvalue decomposition of matrix A as follows:

$$
\mathrm{A} = \Psi\Lambda\Psi^{-1} = \sum_{k=1}^{n} \psi_k \lambda_k \psi_k \,,
$$
(3.7)

where Ψ is the eigenvector matrix, and $\Lambda = diag(\lambda_i)$ is the eigenvalues matrix. Term λ_k denotes the eigenvalues of the discrete-time system. Accordingly, the eigenvalues of the continuous system are calculated such that

$$
\lambda_{ck} = \frac{\ln(\lambda_k)}{\Delta t} \,.
$$
(3.8)

Consequently, the modal parameters of the system, that is, the natural frequency f_k, damping ratio ζ_k, and the mode shape ϕ_k are calculated [134] as follows:

$$f_k = \frac{|\lambda_{ck}|}{2\pi}, \qquad \zeta_k = -100\frac{\text{Re}(\lambda_{ck})}{|\lambda_{ck}|}, \qquad \phi_k = C\psi_k. \tag{3.9}$$

Estimating the system matrix A starts with calculating the output covariance R_i with time lag $i\Delta t$, which is factorized such that $R_i = \text{CA}^{i-1}G = \mathbb{E}[y_{k+1}\ y_k^T]$, where G is the next-state output correlation matrix, $G = \mathbb{E}[x_{k+1}\ y_k^T]$ [135]. Then, the block Toeplitz matrix $T_{1|i}^{ref}$ is formed by multiplication of future and past measurements, and can be assembled concerning subset reference sensors (ref) [136] as follows:

$$T_{1|i}^{ref} = \begin{bmatrix} R_i^{ref} & R_{i-1}^{ref} & \cdots & R_1^{ref} \\ R_{i+1}^{ref} & R_i^{ref} & \cdots & R_2^{ref} \\ \cdots & \cdots & \cdots & \cdots \\ R_{2i-1}^{ref} & R_{2i-2}^{ref} & \cdots & R_i^{ref} \end{bmatrix}. \tag{3.10}$$

The block Toeplitz matrix $T_{1|i}^{ref}$ can be factorized into the extended observability matrix O_i and the reserved extended stochastic controllability matrix Γ_i^{ref} such that

$$T_{1|i}^{ref} = O_i\Gamma_i^{ref} = \begin{bmatrix} C \\ CA \\ \cdots \\ CA^{i-1} \end{bmatrix} \begin{bmatrix} A^{i-1}G^{ref} & \cdots & AG^{ref}\ G^{ref} \end{bmatrix}. \tag{3.11}$$

The singular value decomposition is used to reduce the block Toeplitz matrix $T_{1|i}^{ref}$ as follows:

$$T_{1|i}^{ref} = USV^T = \begin{bmatrix} U_1\ U_2 \end{bmatrix} \begin{bmatrix} S_1 & 0 \\ 0 & S_2 \simeq 0 \end{bmatrix} \begin{bmatrix} V_1^T \\ V_2^T \end{bmatrix} = U_1 S_1 V_1^T, \tag{3.12}$$

where S_1 is a diagonal matrix containing the singular values in descending order. Using Eqs. (3.11) and (3.12), the matrix O_i and the matrix Γ_i^{ref} are written such that $O_i = U_1 S_1^{\frac{1}{2}}$, and $\Gamma_i^{ref} = S_1^{\frac{1}{2}} V_1^T$. Then, the output matrix C can be determined as the first l rows of the matrix O_i. The system matrix A is calculated using the matrix O_i [137] as follows:

$$A = \underline{O_i}^\dagger \overline{O_i}, \tag{3.13}$$

where $\underline{O_i}$ denotes the matrix O_i without the last l rows, $\overline{O_i}$ is the matrix O_i without the first l rows, and $\dagger$ denotes the pseudo-inverse.

The key point in the SSI method is to determine the model order n. Theoretically, the model order equals to the number of nonzero singular values of Teoplitz matrix, which is practically not the case, due to the noise, non-stationarity, and non-linearity of the data. To overcome that, stabilization diagram and stability criteria to natural frequencies, damping ratios, and mode shapes are used to identify the stable solution [138].

3.5 Signal Processing for SHM

3.5.1 Frequency Domain

Defining the signal as a function $f(x)$, where x is an independent variable defines the domain of the signal, for example, in the *time-domain.* Thus, a signal in the time domain $x(t)$ defined on the interval $\left[\frac{-\tau}{2}, \frac{\tau}{2}\right]$ is represented using exponential Fourier series as follows:

$$x(t) = \sum_{n=-\infty}^{\infty} c_n \, e^{in\omega t}, \tag{3.14}$$

where $\omega = 2\pi/\tau$ is the fundamental frequency of the period τ, and i is the imaginary units of the complex number, such that $i^2 = -1$. The spectral coefficients c_n are defined as follows:

$$c_n = \frac{1}{\tau} \int_{-\frac{\tau}{2}}^{\frac{\tau}{2}} x(t) \, e^{-in\omega t} \, dt. \tag{3.15}$$

Using this and by rearranging terms, the *Fourier transform F* is obtained as follows [139]:

$$F[x(t)] = X(\omega) = \int_{-\infty}^{\infty} x(t) e^{-i\omega t} dt, \tag{3.16}$$

where $X(\omega)$ is a *frequency-domain* of signal $x(t)$, which is often referred to as a *spectrum.* The *inverse Fourier transform $F^{-1}[X(\omega)]$* allows the time-domain to switch back as follows:

$$F^{-1}[X(\omega)] = x(t) = \frac{1}{2\pi} \int_{-\infty}^{\infty} x(\omega) e^{i\omega t} d\omega. \tag{3.17}$$

3.5.2 Fast Fourier Transform

Storing a continuous signal on a computer requires infinite memory. Usually, the signals collected by sensors are digitized, or in other words, they are stored in the form of discrete-time. By sampling the continuous signal at regular intervals, such as Δt seconds apart, the signal $x(t)$ can be written as a finite vector of N samples, such as $x(t) = \{x_0, \cdots, x_r, \cdots, x_{N-1}\}$, where $x_r = x(t_r) = x(t_0 + r\Delta t)$, $r \in \mathbb{N}$. Considering the reference time t_0 to be $t_0 = 0$, the

time t_r becomes $t_r = r\Delta t$.

The Discrete Fourier Transform (DFT) is an essential tool used in the field of digital signal processing to derive a frequency-domain (spectral) representation of the signal. A discrete signal defined on $[\frac{-\tau}{2}, \frac{\tau}{2}]$ is decomposed into a series of periodic signals using an exponential Fourier transform [140], as follows:

$$x(t) = \sum_{n=-\infty}^{\infty} c_n \, e^{2\pi i \left(\frac{n}{\tau}\right)t} \,. \tag{3.18}$$

The spectral coefficients c_n are calculated, such that:

$$c_n = \frac{1}{\tau} \int_{-\frac{\tau}{2}}^{\frac{\tau}{2}} x(t) \, e^{-2\pi i \left(\frac{n}{\tau}\right)t} \, dt. \tag{3.19}$$

Using the concept of DFT and considering $\tau = N \cdot \Delta t$, the spectral coefficients c_n are written as follows:

$$c_n = \frac{1}{N} \sum_{r=0}^{N-1} x_r \, e^{-2\pi i \left(\frac{nr}{N}\right)} \,. \tag{3.20}$$

The FFT is an efficient algorithm for the computation of the DFT coefficients, which exploits the computational redundancy in the equations defined by the DFT. The FFT algorithm reduces the required number of operations to $N \log_2 N$, compared with N^2 operations in the case of using the DFT [141].

The frequency-domain of the perfect time-domain input-output system $\mathbf{S}$ is defined such that

$$Y(\omega) = H(\omega)X(\omega) \,, \tag{3.21}$$

where $X(\omega)$ and $Y(\omega)$ are the FFT of the input signal $x(t)$ and output signal $y(t)$, respectively. The Frequency Response Function (FRF), denoted as $H(\omega)$, turns the relation between the input signal and the response of the system in the frequency domain into a simple multiplication compared to the system $\mathbf{S}$ in the time-domain.

It is more convenient, especially for random signals, to represent the spectrum $X(\omega)$ by *averaging* the squared spectrum, or the PSD, denoted as $S_{xx}(\omega)$, which is defined as follows:

$$S_{xx}(\omega) = \mathbb{E}[|X(\omega)|^2] = \mathbb{E}[X(\omega)X(\omega)^*] \,. \tag{3.22}$$

In the same manner, considering two signals $x(t)$ and $y(t)$, the Cross-Spectral Density (CSD) S_{yx} is defined, as follows:

$$S_{yx}(\omega) = Y(\omega)X(\omega)^* \,. \tag{3.23}$$

Thus, the FRF is re-estimated as

$$H(\omega) = \frac{S_{yx}(\omega)}{S_{xx}(\omega)}, \tag{3.24}$$

or in another form as follows:

$$S_{yy}(\omega) = |H(\omega)|^2 S_{xx}(\omega). \tag{3.25}$$

Generally, any system $\mathbf{S}$ has noise on both the input and output signal. By adding a noise $n(t)$ to the unknown clean part of the signal $u(t)$, such that $x(t) = u(t) + n(t)$. Similarly, the response signal $y(t)$ is also subjected to the measurement noise $m(t)$, such as, $y(t) = v(t) + m(t)$, where $v(t)$ is the unknown clean output signal. Then, the general expression of the coherence function $\gamma^2(\omega)$ is defined as follows:

$$\gamma^2(\omega) = \frac{|S_{yx}(\omega)|^2}{S_{yy}(\omega)S_{xx}(\omega)} = \frac{1}{\left(1 + \frac{S_{mm}(\omega)}{S_{vv}(\omega)}\right)\left(1 + \frac{S_{nn}(\omega)}{S_{vv}(\omega)}\right)}. \tag{3.26}$$

The coherence is always positive, with $\gamma^2(\omega) = 1$ when $S_{mm}(\omega) = 0$, or $S_{nn}(\omega) = 0$. Consequently, the coherence function detects the noise in both the input and output of the system. In addition, $\gamma^2(\omega) < 1$ in the case of the nonlinearity of the system [74].

3.5.3 Time-Frequency Domain

The FFT are powerful tools for identifying the frequency contents of signals. However, they are valid and effective in the case of stationary signals. In the case of signals where the frequency content changes over time (non-stationary signals), more advanced methods (such as Short-Time Fourier Transform (STFT) and the Wavelet Transform (WT)) can be used. The basic idea behind this solution is to consider the signal as stationary over a finite time duration T by using a localized time window w. The *time-frequency* map, or *spectrogram*, is built using the STFT as follows:

$$X(\tau, \omega) = \int_{-\infty}^{\infty} w(t - \tau)e^{-i\omega t}x(t)dt. \tag{3.27}$$

One example of the used windows is the Gaussian window $w(t - \tau) = exp[-1/2(\frac{t-\tau}{\sigma})^2]$. The finite time duration T needs to be chosen carefully, as using a small T leads to learning deeper about the signal with lower frequency resolution within the window. Conversely, using a big T improves the resolution of the frequency content although not all of the features of the signal will be identified. Another drawback of the STFT is that the original

signal cannot be easily reconstructed from the spectrogram. The WT, which is not a part of this study, can be efficiently used to overcome the problems of the STFT [141].

3. DAMAGE INSPECTION AND DIAGNOSIS

Part II

Methodology and Applications

Chapter 4

Methodology

4.1 Parameter Identification

4.1.1 Introduction

Verifying the actual behavior of existing structures requires knowledge of the actual parameters of the given system, for example, the material properties and the boundary conditions. The characteristic parameters of the structure provided by the manufacturer in the datasheet are usually used for the structural design. However, this information is not sufficient for evaluating existing structures. This data deviates from the actual values to assure the quality of the constructed system, for example, using the CI to describe the data. To solve this crucial issue, engineers usually conduct destructive and non-destructive experiments on the given structure, which do not explicitly give the required parameters in most cases. For these reasons, *parameter estimation* as a statistical term, or PI as an engineering term, is currently one of the essential tasks of engineering and science, especially as the increasing capacity of computers makes the tasks more practical and efficient.

In this section, inverse problem techniques are implemented to identify unknown parameters and quantify their uncertainties by utilizing measurements of the conducted experimental models. One of the main challenges of the PI process is solving the ill-posedness of the inverse problem using regularization techniques, such as Tikhonov regularization in the deterministic approach. As mentioned in Section 2.5, Bayesian inference is a probabilistic approach of the UQ framework that has an added value of quantifying the uncertainty of the identified parameters without additive efforts. This prioritizes Bayesian inference as the focal approach for inferring the unknown parameters and their uncertainties in this study.

4.1.2 Problem and Formation

An approach that quantitatively and qualitatively infers unknown parameters is newly proposed in this study. The approach focuses on increasing the number of inferred parameters as is possible by utilizing the most relevant experimental measurements. On the other hand, it proposes an enhanced combination of measurements, based on their characteristics, to improve the quality of inferred parameters. As shown in Fig. 4.1, the approach is applied using multiple measurements, the corresponding numerical models, and the PI process described in Section 4.1.4.
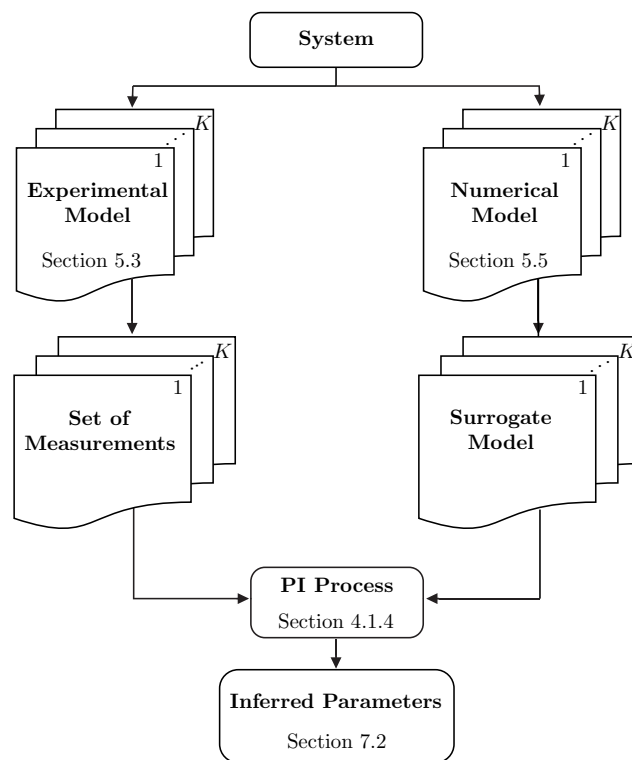
Fig. 4.1. The proposed approach of PI.

4.1.3 Updated Forward Model

Parameters of engineering models have mainly physical meanings, that is, they represent material properties, geometry, boundary conditions and so on. Other parameters have no physical interpretation, but they are needed to build the computational and numerical models. Based on the nature of their uncertainties, parameters can be associated with well-known uncertainty, unknown uncertainty, or even considered as deterministic parameters.

In this study, three types of parameters are considered, as follows: input parameters that

are subjected to uncertainty $\boldsymbol{x} \in \mathcal{X}$, non-physical input parameters $\boldsymbol{\xi} \in \mathcal{Z}$, and well-known deterministic input parameters, $\boldsymbol{d} \in \mathcal{D}$. In addition, hyperparameters $\boldsymbol{\theta} \in \Theta$ are sometimes needed to describe the unknown uncertainty of uncertain parameters. By this, the forward model $\mathcal{M}$ in Eq. (2.1) is reconstituted by classifying the input parameters based on their nature and uncertainties, as follows:

$$
\begin{aligned}
\mathcal{M} : \mathcal{X} \times \mathcal{Z} \times \mathcal{D} &\to \tilde{\mathcal{Y}} \\
(\boldsymbol{x}, \boldsymbol{\xi}, \boldsymbol{d}) &\mapsto \tilde{\boldsymbol{y}} = \mathcal{G}(\boldsymbol{x}, \boldsymbol{\xi}, \boldsymbol{d}) \,.
\end{aligned}
\tag{4.1}
$$

In the UQ probabilistic framework (see Section 2.8.2), uncertain input parameters $\boldsymbol{x}$ are considered as random variables $\boldsymbol{X} = (X_1, \cdots, X_m)^T \in \mathbb{R}^m$ with a prior PDF $\pi(\boldsymbol{x}; \boldsymbol{\theta}_X)$. Here, $\boldsymbol{\theta}_X$ represents the unknown hyperparameters that describe the variety of parameters $\boldsymbol{x}$. These hyperparameters are random variables $\boldsymbol{\Theta}_X$ with prior density distributions $\boldsymbol{\Theta}_X \sim \pi_{\boldsymbol{\Theta}_X}(\boldsymbol{\theta}_X)$. In most cases, input parameters are conditionally independent, then the prior of the unknown parameters is evaluated from $\pi(\boldsymbol{x}|\boldsymbol{\theta}_X) = \prod_{i=1}^{m} \pi(x_i|\boldsymbol{\theta}_X)$. Consequently, the joint prior distribution is written as

$$
\pi_0(\boldsymbol{x}, \boldsymbol{\theta}_X) = \left(\prod_{i=1}^{m} \pi(x_i|\boldsymbol{\theta}_X) \right) \cdot \pi_{\boldsymbol{\Theta}_X}(\boldsymbol{\theta}_X) \,.
\tag{4.2}
$$

Random variables of the observations $\tilde{\boldsymbol{Y}} = \{\tilde{Y}_1, \cdots, \tilde{Y}_n\}^T \in \mathbb{R}^n$ represent the multiple outputs of the given case study. Their realizations $\tilde{\boldsymbol{y}} = \{\tilde{y}_1, \cdots, \tilde{y}_n\}^T$ are observed directly from measurements of the conducted experiments, (or evaluated based on them). Now, the stochastic forward model in Eq. (2.17) is updated such that

$$
\tilde{\boldsymbol{Y}} = \mathcal{G}(\boldsymbol{X}, \boldsymbol{\Theta}_X, \boldsymbol{\xi}, \boldsymbol{d}) + \mathbf{E} \,.
\tag{4.3}
$$

In this case study, the realizations $\boldsymbol{\eta} = \{\eta_1, \cdots, \eta_n\}^T$ of the total errors $\mathbf{E}$ are not well-known, because they are not quantified through experiments. This increases the number of unknown parameters and includes additional hyperparameters $\boldsymbol{\theta}_{\mathrm{E}}$ with a prior distribution $\pi_{\boldsymbol{\Theta}_{\mathrm{E}}}(\boldsymbol{\theta}_{\mathrm{E}})$. $\boldsymbol{\theta}_{\mathrm{E}}$ is needed to define the density distribution of the error $\mathbf{E} \sim \pi_{\mathrm{E}}(\boldsymbol{\eta}; \boldsymbol{\theta}_{\mathrm{E}})$. Assuming that $\boldsymbol{\theta}_{\mathrm{E}}$ is mutually independent of $\boldsymbol{x}$ and $\boldsymbol{\theta}_X$, the joint prior distribution in Eq. (2.17) can be updated as follows:

$$
\pi_0(\boldsymbol{x}, \boldsymbol{\theta}_X, \boldsymbol{\theta}_{\mathrm{E}}) = \left(\prod_{i=1}^{m} \pi(x_i|\boldsymbol{\theta}_X) \right) \cdot \pi_{\boldsymbol{\Theta}_X}(\boldsymbol{\theta}_X) \cdot \pi_{\boldsymbol{\Theta}_{\mathrm{E}}}(\boldsymbol{\theta}_{\mathrm{E}}) \,.
\tag{4.4}
$$

As mentioned previously in Section 2.7, errors $\mathbf{E}$ have a likely multivariate Gaussian distribution $\mathbf{E} \sim \mathcal{N}(0, \boldsymbol{\Sigma})$ with zero-means $\mathbb{E}(\boldsymbol{\eta}) = 0$. $\boldsymbol{\Sigma}$ represents the symmetric and

positive-semidefinite covariance matrix that is unknown (at least in this case), and is estimated through the applied framework. For uncorrelated errors, the covariance matrix is rephrased to be $\boldsymbol{\Sigma} = \sigma_{\mathrm{E}}^2 \, diag\{\tilde{y}_1, \cdots, \tilde{y}_n\}^2 \in \mathbb{R}^{n \times n}$, where σ_{E}^2 is the variance of the errors $\boldsymbol{\eta} = \tilde{\boldsymbol{y}} - \boldsymbol{\mathcal{G}}(\boldsymbol{x}, \boldsymbol{\xi}, \boldsymbol{d})$. In this case, it is more convenient to use matrix notation in presenting the Gaussian multivariate likelihood, as follows:

$$\mathcal{L}(\boldsymbol{x}, \boldsymbol{\xi}, \boldsymbol{d} | \tilde{\boldsymbol{y}}, \boldsymbol{\theta}_{\mathrm{E}}) = \frac{1}{(2\pi)^{\frac{n}{2}} \sqrt{|\boldsymbol{\Sigma}|}} \cdot e^{-\frac{1}{2} \boldsymbol{\eta}^T \boldsymbol{\Sigma}^{-1} \boldsymbol{\eta}} \,. \tag{4.5}$$

It is common to consider the observations $\tilde{\boldsymbol{Y}}$ and hyperparameters of the inputs $\boldsymbol{\Theta}_{\boldsymbol{X}}$ as mutually independent, that is, $\pi(\tilde{\boldsymbol{y}} | \boldsymbol{x}, \boldsymbol{\theta}_X) = \pi(\tilde{\boldsymbol{y}} | \boldsymbol{x})$. Accordingly, the posterior in Eq. (2.19) is described as follows:

$$\pi(\boldsymbol{x}, \boldsymbol{\theta}_X, \boldsymbol{\theta}_{\mathrm{E}} | \tilde{\boldsymbol{y}}) = \frac{\pi(\tilde{\boldsymbol{y}} | \boldsymbol{x}) \cdot \pi_0(\boldsymbol{x}, \boldsymbol{\theta}_X, \boldsymbol{\theta}_{\mathrm{E}})}{\pi(\tilde{\boldsymbol{y}})} \,. \tag{4.6}$$

Considering the definition of the likelihood in Section 2.8.2, the likelihood $\pi(\tilde{\boldsymbol{y}} | \boldsymbol{x})$ in Eq. (4.6) can be written as $(\tilde{\boldsymbol{Y}} | \boldsymbol{x}, \boldsymbol{\xi}, \boldsymbol{d}) \sim \pi_{\mathrm{E}}(\tilde{\boldsymbol{y}} - \boldsymbol{\mathcal{G}}(\boldsymbol{x}, \boldsymbol{\xi}, \boldsymbol{d}); \boldsymbol{\Sigma})$. For mutually independent observations $\tilde{\boldsymbol{Y}}$, the likelihood is calculated as

$$\pi(\tilde{\boldsymbol{y}} | \boldsymbol{x}) \equiv \mathcal{L}(\boldsymbol{x}, \boldsymbol{\xi}, \boldsymbol{d} | \tilde{\boldsymbol{y}}, \boldsymbol{\theta}_{\mathrm{E}}) = \prod_{i=1}^{n} \pi_{\mathrm{E}}(\tilde{y}_i - \mathcal{G}_i(\boldsymbol{x}, \boldsymbol{\xi}, \boldsymbol{d}); \Sigma_i) \,, \tag{4.7}$$

with Σ_i being the ith component of the main diagonal of the matrix $\boldsymbol{\Sigma}$; by this, the normalization constant z can be updated as follows:

$$z = \pi(\tilde{\boldsymbol{y}}) = \int_{\mathcal{X}} \int_{\mathcal{Z}} \int_{\Theta_X} \int_{\Theta_{\mathrm{E}}} \mathcal{L}(\boldsymbol{x}, \boldsymbol{\xi}, \boldsymbol{d} | \tilde{\boldsymbol{y}}, \boldsymbol{\theta}_{\mathrm{E}}) \, \pi_0(\boldsymbol{x}, \boldsymbol{\theta}_X, \boldsymbol{\theta}_{\mathrm{E}}) \, \mathrm{d}\boldsymbol{x} \, \mathrm{d}\boldsymbol{\xi} \, \mathrm{d}\boldsymbol{\theta}_X \, \mathrm{d}\boldsymbol{\theta}_{\mathrm{E}} \,. \tag{4.8}$$

At this point, unknown parameters can be inferred by sampling from the posterior $\pi(\boldsymbol{x}, \boldsymbol{\theta}_X, \boldsymbol{\theta}_{\mathrm{E}} | \tilde{\boldsymbol{y}})$ using the TMCMC algorithm.

4.1.4 Parameter Identification Methodology

The primary goal of the proposed approach is to infer unknown parameters quantitatively and qualitatively. In this sense, the available observations of the conducted experiments are utilized and managed in two strategies, as shown in Fig. 4.2. After implementing the proposed strategies, the quality of the results is compared. Then, the results with the best quality from one of the applied strategies is selected [142].
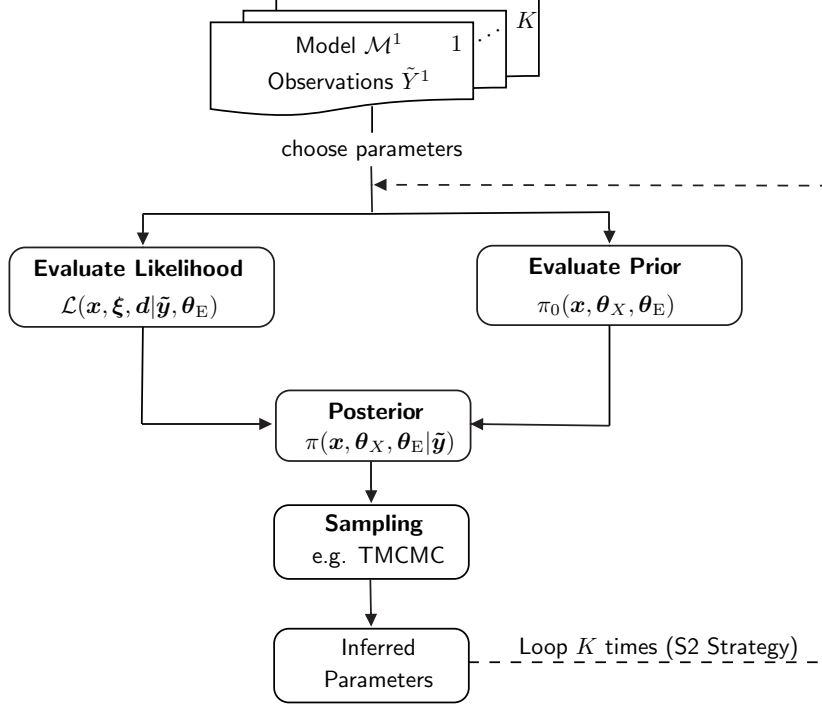
Fig. 4.2. The proposed process of PI.

4.1.4.1   Strategy 1 (S1)

In this *All-in-one* strategy (S1) [142], the observations of different experiments, or even the observations of different sensors in the same experiment, are formed in one observations vector $\tilde{\boldsymbol{Y}} = \{\tilde{\boldsymbol{Y}}^1, \cdots, \tilde{\boldsymbol{Y}}^K\}^T$ that has the corresponding models $\mathcal{M} = \{\mathcal{M}^1, \cdots, \mathcal{M}^K\}^T$. Term K represents the number of conducted experiments, where the observations of the kth experiment are $\tilde{\boldsymbol{Y}}^k = \{\tilde{Y}_1^k, \cdots, \tilde{Y}_{n^k}^k\}^T$. The realizations of these random variables are $\tilde{\boldsymbol{y}}^k = \{\tilde{y}_1^k, \cdots, \tilde{y}_{n^k}^k\}^T \in \mathbb{R}^{n^k}$.

The global likelihood becomes $(\tilde{\boldsymbol{Y}}^1, \cdots, \tilde{\boldsymbol{Y}}^K | \boldsymbol{x}, \boldsymbol{\xi}, \boldsymbol{d}) \sim \pi_{\mathrm{E}}(\tilde{\boldsymbol{y}} - \boldsymbol{\mathcal{G}}(\boldsymbol{x}, \boldsymbol{\xi}, \boldsymbol{d}); \boldsymbol{\Sigma})$, where $\boldsymbol{\Sigma} = diag\{\boldsymbol{\Sigma}^1, \cdots, \boldsymbol{\Sigma}^K\} \in \mathbb{R}^{N \times N}$ is the global covariance matrix and $N = \sum_{k=1}^{K} n^k$. Assuming that data in each experiment are conditionally independent given the unknowns, we can update the likelihood in Eq. (4.9) as follows:

$$\mathcal{L}(\boldsymbol{x}, \boldsymbol{\xi}, \boldsymbol{d} | \tilde{\boldsymbol{y}}^1, \cdots, \tilde{\boldsymbol{y}}^K, \boldsymbol{\theta}_{\mathrm{E}}) = \prod_{k=1}^{K} \mathcal{L}^k(\boldsymbol{x}, \boldsymbol{\xi}, \boldsymbol{d} | \tilde{\boldsymbol{y}}^k, \boldsymbol{\theta}_{\mathrm{E}}^k), \tag{4.9}$$

where $\mathcal{L}^k(\boldsymbol{x}, \boldsymbol{\xi}, \boldsymbol{d} | \tilde{\boldsymbol{y}}^k, \boldsymbol{\theta}_{\mathrm{E}}^k) = \prod_{i=1}^{n^k} \pi_{\mathrm{E}}(\tilde{y}_i^k - \mathcal{G}_i^k(\boldsymbol{x}, \boldsymbol{\xi}, \boldsymbol{d}); \Sigma_i^k)$ is the likelihood of the observations of the kth experiment.

The posterior is written as $\pi(\boldsymbol{x}, \boldsymbol{\theta}_X, \boldsymbol{\theta}_{\mathrm{E}} | \tilde{\boldsymbol{y}}^1, \cdots, \tilde{\boldsymbol{y}}^K) \propto \pi(\tilde{\boldsymbol{y}}^1, \cdots, \tilde{\boldsymbol{y}}^K | \boldsymbol{x}) \cdot \pi_0(\boldsymbol{x}, \boldsymbol{\theta}_X, \boldsymbol{\theta}_{\mathrm{E}})$.

It can be evaluated as normal using (for example) the TMCMC algorithm or any other appropriate method.

4.1.4.2 Strategy 2 (S2)

In the stochastic UQ framework that is utilized in the PI process, the concept of sensitivity plays a key role in finding the unknowns. The more the given model is sensitive to the unknown parameter, the lower is the uncertainty of this inferred parameter. In this sense, an adapted sequential Bayesian approach is newly built in this study, named the *sensitivity-based* strategy (S2), to achieve the goal of increasing the quality of the identified parameters [142].

The observations $\tilde{Y}$ are classified into K subsets, based on the sensitivity of the unknown parameters, that is, $\tilde{Y} = \{\tilde{Y}^1, \cdots, \tilde{Y}^K\}^T$ of the forward model $\mathcal{M}$ of the considered system. The realizations of the observations are $\tilde{y} = \{\tilde{y}^1, \cdots, \tilde{y}^K\}^T$. Then, the Bayesian updating framework is sequentially applied in a step-wise manner associated with the obtained subsets, by assuming the mutual independence of the observation subsets, in other words, $\pi(\tilde{y}^1, \cdots, \tilde{y}^K) = \prod_{k=1}^{K} \pi(\tilde{y}^k)$.

In the first step at $k = 1$, the joint prior $\pi_0(x, \theta_X, \theta_E)$ and the first set of observations $\tilde{y}^1$ are utilized to build the posterior, as follows:

$$\pi^1(x, \theta_X, \theta_E | \tilde{y}^1) = \frac{\mathcal{L}^1(x, \xi, d | \tilde{y}^1) \cdot \pi_0(x, \theta_X, \theta_E)}{\pi(\tilde{y}^1)} . \tag{4.10}$$

In the following steps, the posterior of the previous step $\pi(x, \theta_X, \theta_E | \tilde{y}^1)$ and the corresponding set of observations $\tilde{y}^k$ are used, until the end of the observations subsets is reached, that is, $k = 2, \cdots, K$. The posterior of the step k^{th} could then be generalized to

$$\pi^k(x, \theta_X, \theta_E | \tilde{y}^1, \cdots, \tilde{y}^k) = \frac{\mathcal{L}^k(x, \xi, d | \tilde{y}^k) \cdot \pi^{k-1}(x, \theta_X, \theta_E | \tilde{y}^{k-1})}{\pi(\tilde{y}^k)} . \tag{4.11}$$

In each step, the parameters are inferred by implementing the MCMC method, namely the, TMCMC algorithm. However, this increases the computational time of the whole process, because the parameters are inferred at each sub-step. At the same time, it is still reasonable and has significant advantages in improving the convergence of the MCMC algorithm and enhancing the quality of the identified parameters.

4.2 Status Monitoring of Structures

4.2.1 Introduction

A monitoring approach is built in the current Chapter 4 to detect changes in a given structure using the data from an SHM system. The newly proposed approach covers the status monitoring of cantilever structures, and will be implemented on the catenary poles (see Chapter 8). The approach solves the Level 1 of DD through utilizing logistic functions for detecting the outliers of the structure data, which avoids the expensive learning step in the existing approaches of DD. Then, the Levels 2 and 3 of DD are handled using the concept of data fusion of multiple dynamic properties and multiple modes of the structure.

The flowchart in Fig. 4.3 presents a vibration-based status monitoring approach that uses outputs of the SHM systems in tracing the status of the structure of interest. The approach compares the newly obtained natural frequencies and mode shapes of the given structure with healthy data using the Status Monitoring (SM) algorithm described in Section 4.2.2. When no damage is detected, the healthy data is updated, and to be used later for subsequent checks. The damage identification algorithms described in Section 4.2.3 are activated when the SM algorithm classifies changes in the given system as damage. As a result, the damage is localized and quantified. This is then followed by a further decision-making process (which is not a part of this study).

4.2.2 Status Monitoring Algorithm

The proposed SM algorithm uses the concept of control charts to classify the status of the structure of interest, based on its healthy data. The healthy data of the structure defines the reference status. New features of the given structure λ_d are calculated using newly data recorded by an SHM system, namely, the natural frequencies $\mathbf{f}$, the changes of natural frequencies $\Delta\mathbf{f}$, and MAC values. Then, the new features are compared with healthy data. The control chart in Fig. 4.4 (left) describes the proposed approach for a considered feature λ_d. The new value of feature $\hat{\lambda}_d$ is classified as damage when it is located outside pre-defined alarm limitation for healthy data, or a so-called *red* region. The area within the Alarm Control Limit (ACL) is divided into two regions. First, the *orange* region represents the warning area when the feature of the structure approaches the alarm area. Second, the *green* region represents when $\hat{\lambda}_d$ is still close to the mean values μ_λ of the health data of a feature λ, and below the Warning Control Limit (WCL).

The ACL is defined as a factor β of the standard deviation σ_λ of the considered feature λ, such that $ACL = \beta \cdot \sigma_\lambda$. The no-damage case is defined to satisfy $\Delta_{norm} \leq 1$. The
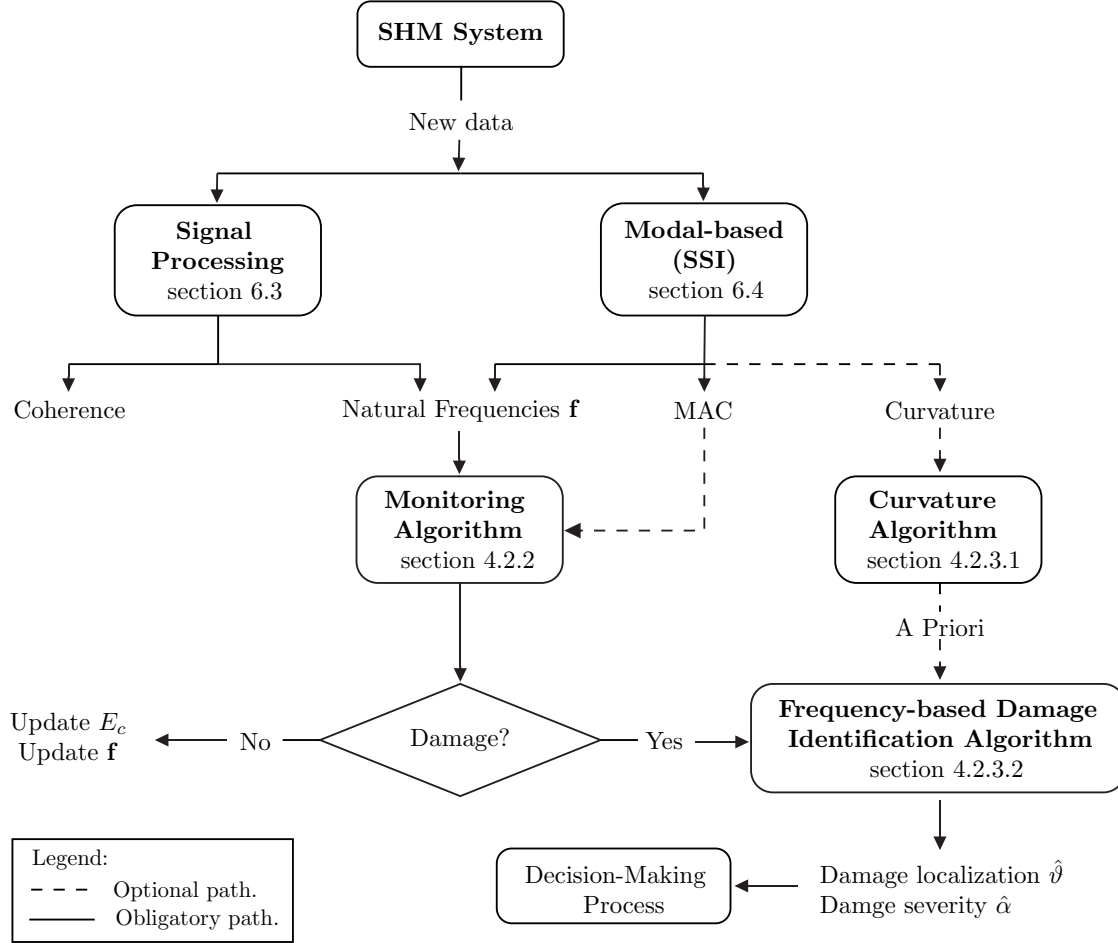
Fig. 4.3. Status Monitoring Approach.

normalized residual Δ_{norm} is defined, as follows:

$$\Delta_{norm} = \frac{|\mu_\lambda - \hat{\lambda}_d|}{\beta \cdot \sigma_\lambda} \, . \tag{4.12}$$

Apart from the classical use of control charts [102], the proposed Status Monitoring algorithm uses a logistic function (a Sigmoid function) to classify the status of the structure of interest within pre-specified regions (namely, safe, warning, and alarm). Besides the classification of features, the Sigmoid function associates studied features with probability values, which later makes the decision-making process more practicable [143]. The Sigmoid function $S(z)$ is defined, such that

$$S(z) = \frac{1}{1 + e^{-z}} \, , \tag{4.13}$$
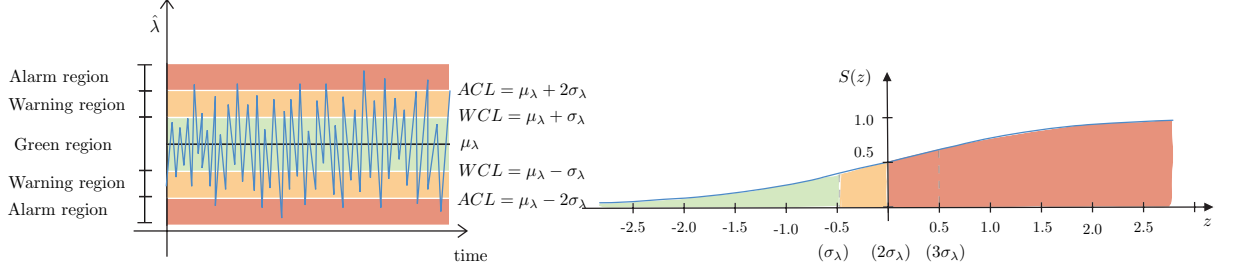
Fig. 4.4. Pre-specified classification regions for $\beta = 2$: using control chart concept (left), using Sigmoid function (right).

where the Sigmoid variable z is defined, such that $z = \Delta_{norm} - 1$.

An illustration of the Sigmoid function is shown in Fig. 4.4 (right) for $\beta = 2$, where the values of $z = \{-0.5, 0, 0.5\}$ correspond to control limit values of $\{\sigma_\lambda, 2\sigma_\lambda, 3\sigma_\lambda\}$.

Test data is compared to a reference status using a sliding window with a length w_{len}, and a window shift w_{sh}. The window length w_{len} decreases with the increase in speed by which data is changed. The window shift w_{sh} controls the smoothness of the results.

Based on the values calculated using Eq. (4.13), the Damage Index (DI) is defined as the change of Sigmoid indices $\tilde{S}$, as follows:

$$\text{DI}_i = \frac{\tilde{S}_i^d - \tilde{S}_i^u}{\tilde{S}_i^u} , \qquad (4.14)$$

where DI_i is the damage index of the ith mode. $\tilde{S}_i^d$ and $\tilde{S}_i^u$ represent Sigmoid indices of the damaged and un-damaged structure, respectively. Sigmoid index $\tilde{S} = \sum_{p=1}^{P}(S_{nr}^p \cdot S_v^p)$ evaluates the number S_{nr} and values S_v of the outliers P that overpass a threshold calculated using the reference status.

4.2.3 Damage Identification Algorithms

Once the SM algorithm classifies the structure status as damaged, a damage identification algorithm is required to identify and quantify the structural damage. It is important to build an algorithm that identifies the damage along the structure efficiently using the available data from SHM. Accordingly, two vibration-based algorithms are proposed. The first is the Frequency-based Damage Identification (FDI) algorithm [144] that detects the location and severity of the damage. The second is a Curvature-based Damage Identification (CDI) algorithm that is integrated into the first algorithm to provide the damage location a priori, which improves the quality of outcomes of FDI algorithm [144].

4.2.3.1 Curvature-based Damage Identification Algorithm

The CDI algorithm [144] uses relative changes of modal curvatures $\Delta\nu$ to localize damage along the given structure by applying Bayesian inference techniques as discussed in Section 2.8.2. Realizations $\tilde{\boldsymbol{y}}$ of observations $\tilde{\boldsymbol{Y}}$ are considered such that $\tilde{\boldsymbol{y}} \equiv \{\nu_1, \cdots, \nu_i, \cdots, \nu_n\}^T$, where ν_i is the modal curvature of the mode ϕ_i, and n is the number of considered mode shapes. Unknown parameters vector $\boldsymbol{x}$ is formed from the coordinates $\boldsymbol{\vartheta}$ of the attached sensors m along the structure, such as, $\boldsymbol{x} \equiv \{\vartheta_1, \cdots, \vartheta_j, \cdots, \vartheta_m\}^T$.

For mutually independent observations $\tilde{\boldsymbol{Y}}$, the likelihood $\mathcal{L}^j$ at location ϑ_j is suggested by [125], such that

$$\mathcal{L}^j(\vartheta_j|\boldsymbol{\nu}) = \prod_{i=1}^{n} \pi(\nu_i|\vartheta_j), \tag{4.15}$$

where the probability function $\pi(\nu_i|\vartheta_j)$ is defined, as follows:

$$\pi(\nu_i|\vartheta_j) = \frac{\Delta\nu_{ij}}{\sum_{i=1}^{n} \Delta\nu_{ij}}. \tag{4.16}$$

The absolute relative changes in the modal curvature $\Delta\nu_{ij}$ are defied, such that $\Delta\nu_{ij} = |\nu_{ij}^d - \nu_{ij}^u|/\nu_{ij}^u$, where ν_{ij}^u and ν_{ij}^d denote un-damaged (ν^u) and damaged (ν^d) modal curvature of the mode ϕ_i at coordinate ϑ_j along the structure.

The prior $\pi_0(\boldsymbol{x}) \equiv \pi_0(\boldsymbol{\vartheta}) = \prod_{j=1}^{m} \pi_0(\vartheta_j)$ is selected to decrease the probability gradually with an increase in the coordinate of the sensor ϑ_j. The selected prior fulfills the high probability of expected damage at the lower part of the cantilever structure; that is, at the points of high stress under applied actions.

Consequently, the probability of damage at ϑ_j given the modal curvatures $\boldsymbol{\nu}$ is written as [125, 145]

$$\pi(\vartheta_j|\boldsymbol{\nu}) = \frac{\mathcal{L}^j(\vartheta_j|\boldsymbol{\nu}) \cdot \pi_0(\boldsymbol{\vartheta})}{\sum_{j=1}^{m}\left(\mathcal{L}^j(\vartheta_j|\boldsymbol{\nu}) \cdot \pi_0(\boldsymbol{\vartheta})\right)}. \tag{4.17}$$

The validation and implementation of the CDI algorithm are discussed in Section 8.4.1.

4.2.3.2 Frequency-based Damage Identification Algorithm

As mentioned in Section 3.3.1, using the natural frequencies for DD has recently regained the interest of some researchers, especially when using Bayesian data fusion of multiple natural frequencies that detects damage to Level 1 of DD. A newly proposed FDI algorithm extends solving the DD problem in Levels 2 and 3 using a UQ framework [144]. The FDI algorithm is a vibration-based Bayesian algorithm that fuses informative data of multiple natural frequencies to quantify and localize the damage along the given structure (For example, see Fig. 8.2).

The Bayesian approach illustrated in Section 4.1.3 is re-used to infer the unknown parameters of DD. Using the changes of the natural frequencies $\Delta\mathbf{f}$ as a damage feature, the realizations $\tilde{\boldsymbol{y}}$ of observations $\tilde{\boldsymbol{Y}}$ are build , as follows, $\tilde{\boldsymbol{y}} \equiv \{\Delta f_1, \cdots, \Delta f_i, \cdots, \Delta f_n\}^T$, where Δf_i is the relative changes in the natural frequency of the ith mode, and n is the number of considered modes. The characteristics of the damage, that is, damage location ϑ and damage severity α, are considered as unknown parameters $\boldsymbol{x}$, such as, $\boldsymbol{x} \equiv \{\vartheta, \alpha\}^T$. Consequently, the posterior in Eq. (4.6) is written as follows:

$$\pi(\vartheta, \alpha|\Delta\mathbf{f}) = \frac{\mathcal{L}(\vartheta, \alpha|\Delta\mathbf{f}) \cdot \pi_0(\vartheta, \alpha)}{\pi(\Delta\mathbf{f})} \ . \tag{4.18}$$

The prior of the damage location $\pi_0(\vartheta)$ can be derived using the curvature algorithm CDI, as mentioned in Section 4.2.3.1. Accordingly, unknown parameters can be inferred by sampling from the posterior $\pi(\vartheta, \alpha|\Delta\mathbf{f})$ using, for example, the TMCMC algorithm. An implementation of the current algorithm can be found in Section 8.4.3.

4.3   Summary

The Bayesian probabilistic approach is proposed to identify the unknown parameters of the given structure. First, the empirical Bayesian approach is adopted through the All-in-one strategy (S1) by utilizing FEM models and observations of the multiple experiments.

An adapted sequential Bayesian approach is proposed to improve the quality of inferred parameters. This approach is implemented through the sensitivity-based strategy (S2) by dividing the observations into subsets based on the sensitivity of the parameters. Then, the Bayesian approach is applied in a sequential manner, considering the posterior of the current step as the prior to the subsequent step. In both strategies, the TMCMC algorithm can be used to sample from the posterior.

In addition, a vibration-based status monitoring approach that traces the status of the structure of interest over time is presented. This approach consists of three algorithms: the SM algorithm, the CDI algorithm, and the FDI algorithm. The proposed monitoring algorithm uses a logistic function for classifying the status of the structure of interest as either damaged, or un-damaged status.

Chapter 5

Case of Study

5.1 Prestressed Concrete Poles

5.1.1 Introduction

Poles are used worldwide to support power transmission, telephone and telegraph lines, street lighting, antenna masts, and overhead power lines for electric trains. For many years, poles were made of wood, steel, and concrete. In the early years of the 20th century, concrete poles were made of normal reinforced concrete. The main hazard with this type of pole is the corrosion of reinforcement bars due to environmental and exposure conditions [12].

Two improvements in the production of concrete poles increase their use. The first improvement was achieved by Eugene Freyssinet, who developed the concept of prestressed concrete. He produced the first prestressed concrete pole in the mid 1930s. The second improvement was the development of the centrifugal or spun-cast method in 1968, which facilitated the production of the hollow cross section, prestressed concrete pole [146]. Nowadays, the production process has developed further, by using high and ultrahigh strength concrete and a better curing process. These improve the durability of the poles, making them lighter and stronger, able to withstand more cyclic loads, and increasing their resistance to environmental conditions [147, 148]. Compared to steel poles, the prestressed, spun-cast concrete poles become more feasible, cheaper; have a longer operational life, and lower lifetime costs [13].

Due to their height and slenderness, prestressed concrete poles are considered to be cantilevered structures. Their capacity is generally governed by their flexural capacity, whereas shear and torsion capacity play a minor role [149, 150, 14]. It is recommended by different design standards that poles are designed to withstand equal bending moments in opposite directions by applying a uniform prestressing, and adapting the prestressing forces
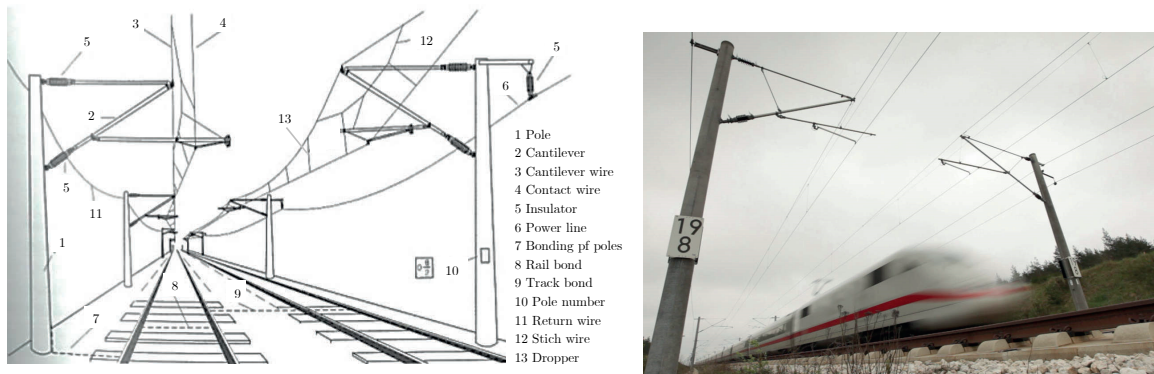
Fig. 5.1. Illustration of the catenary pole system: Schematic illustration (left) [2], and the actual system in Germany (right) [3].

to ensure they remain uncracked under service working conditions [151, 152].

However, spun-cast, prestressed hollow concrete poles are robust structures. Through their history, few cases of failure for the power transmission and lighting poles have been reported in the literature. This includes flexural failure in windstorms [153], and the shear failure under collision [154]. One further registered failure type of spun-cast poles is that of longitudinal cracks, caused by differential shrinkage between the fine layer along the inside of the pole and the coarser layer on the outside [155]. These phenomena are discussed by some literature, for example, [16, 156]. Moreover, the dynamic behavior of this type of pole is also verified in many research studies [157, 158, 159].

5.1.2 Catenary Poles

Structural members, called *catenary poles*, suspend the catenary systems of electric trains. These structural members are installed at equal-spaced distances along the train-track to support the overhead power lines for electric trains. They play a vital role in the entire train system, as any damage to one of these members leads to difficulties in the functionality of the whole system; therefore questions about their performance and material properties are essential. Fig. 5.1 illustrates the different parts of the catenary pole system used in Germany.

This type of pole is mainly subjected to a combination of several actions that include (but is not limited to) static actions, seasonal ambient temperature, and wind effects. Furthermore, trains passing near the poles causes a transient excitation, which forces the poles to vibrate frequently in a complex form. There are three main sources of such transient vibrations. First, vibrations are transmitted from the waving of the catenary cables due

to the interaction between them and the pantograph of the train. second, vibrations are caused by the air pressure wave generated by the train. Third, vibrations travel through the foundation caused by the interaction between the train wheels and the sub-base of the track.

Each of these transient excitation sources have been separately well-studied by many researchers. In the case of train-induced ground vibrations, some research focuses on the nature of the wave that is transmitted through the soil, and how this can be used to detect the train speed [160, 161]. However, the railways and their interaction with the surrounding soil and nearby structures, still offer a very promising research domain, for example, [162]. Other researches study the effect of train-induced vibrations on adjacent buildings, but not the poles that carry the catenary system. In addition, due to the collapse of some of the noise protection walls, Ampunant et al. investigates the effect of aerodynamic pressure loads on such structures when high-speed trains are passing by [163].

The interaction of the train's pantograph and the catenary cables are investigated for various types of pantographs, and different train types and speeds. Some of these studies replace the pole by fixed boundary condition in the numerical model, where others assume some stiffness by using elastic springs to simulate the connection [2, 164]. This is valid to study the behavior of the catenary as an isolated system without taking the actual interaction between it and the poles. Pombo et al. provide a detailed model of the catenary system that includes the poles themselves. However, they study changes in the behavior of the catenary cables without addressing the effects on the poles [165].

As already mentioned, most research (and literature) focuses on power transmission and lighting. Some intensively study the catenary system and the train-induced vibration in the soil. However, scant attention has been paid to the behavior of the *catenary poles* in the literature. Currently, catenary poles have not received adequate attention, given their importance to the entire train system.

This means that further research is needed to detect the actual behavior of these poles and their interaction with the catenary system and surrounding soil. This gives the motivation to focus our study on the dynamic behavior of this type of pole, particularly the prestressed, spun-cast catenary poles made from high-strength concrete. Recently, thousands of these catenary poles have been installed along the new high-speed train track in Germany.

The properties of the prestressed, concrete poles change visibly over time due to different effects, such as, the degradation of concrete because of shrinkage, creep, and low-cycle fatigue; and the increase in prestressing losses. This increases the necessity to trace the performance of the poles under various actions (namely, static, environmental, and dynamic

actions), considering the long-term changes in the material of the pole.

5.2 Case Study

5.2.1 Introduction

In collaboration with Deutsche Bahn (DB), Europoles GmbH & Co. KG developed a system of standard catenary poles for german high-speed rail routes, reaching a speed of $330\,\mathrm{km\,h^{-1}}$. This system fulfills the particular requirements of this type of pole. It considers the minimum maintenance cost, high corrosion resistance, and easy installation. Besides, the poles were designed to have relatively high rigidity; thus the poles exhibit minimal structural and dynamic deformations. This minimizes the oscillation of the catenary pole during and after the passing of the train [3].

The catenary poles were selected as one of the reference projects within the Deutsche Forschungsgemeinschaft (DFG) Research Training Group 1462 (GRK1462) at Bauhaus Universität Weimar. To fulfill the aim of this project, the members of GRK1462 selected the newly-built, high-speed train track between Erfurt and Halle/Leipzig, which provides a unique opportunity to analyze a newly-built structure at different stages: production, installation, and service life. To achieve this, a short-term experimental program and long-term monitoring system were developed to collect the statistical data of the real system.

The experimental program was implemented in the laboratory through a series of short-term tests to verify the properties of the spun-cast poles. This included (but was not limited to) the verification of geometry, compression tests of cut-pieces, vibration tests, and 3-point bending test. More details about this program are available in [166, 167]. In Addition, vibration tests of 16 poles were conducted on-site after the completion of the installation process. At the time of the tests, only the electric return cables were connected to the poles, where the full catenary system was not yet attached [168].

The installed SHM system diagnosed the current state of the structure between the summers of 2015 and 2018. Based on the recorded data, GRK1462 verified different phenomena: detect the train passing, the effects induced by the train passing, the effects caused by environmental changes, and the development of concrete strains and prestressing strands [169, 170].

The experimental program utilized in this study was implemented within the activities of the GRK1462 group and with the contribution of its members, which is highly appreciated. The author was involved mainly in different phases of the 3-point bending test and partially in conducting the vibration test. This included the design of the experiment, implementation, and analysis of the results. For additional verification of the pole, the experimental

Table 5.1: The nominal geometry of the poles.

Dimension	Nominal value
Length, L [m]	10
Outer diameter at the bottom, d_{bot} [mm]	400
Outer diameter at the top, d_{top} [mm]	250
Wall thickness at the bottom, t_{bot} [mm]	62
Wall thickness at the top, t_{top} [mm]	52

program was extended after the close of the project in 2017. The extension covered the vibration test of the damaged poles and the verification of the actual dimensions.

5.2.2 Geometry and Materials

The studied structure is 10 m in height with tapered hollow circular sections. The outer diameter at the bottom end is 400 mm and reduces linearly to 250 mm at the top of the pole. The pole is produced by a spinning method, resulting in a variation of the wall thickness. The geometric of the spun-cast pole is summarized in Table 5.1. However, verification of the geometry in the laboratory showed that, relative to the nominal ones, a considerable increase of 15% in the wall thickness exists due to the spin casting process during production. Nevertheless, the actual measured dimensions are used in this study to ensure optimal estimation of the parameters and more realistic identification of the given structure.

Nominal material properties of the structure, which are summarized in Table 5.2, were extracted from the data sheet provided by the manufacturers. The pole is made of a high-strength concrete with grade C80/95 . Furthermore, the cross-section incorporates ten strands, prestressed initially with a total force of approximately 680 kN. The strands are distributed equally throughout the perimeter. The strand layout is displayed in Fig. 5.2 (right). There is no additional longitudinal reinforcement, except two bars (Ø10 mm) used for grounding. Spiral reinforcement, with a diameter of 5 mm and pitch of 50 mm, is added along the pole.

Table 5.2: Nominal material properties.

Material	Value
Concrete	
Concrete grade	C80/95
Prestressing	
Prestressing strands	7/16" St 1680/1880
Number of strands, n_{st}	10
Area of the strand, A_{st} [mm^2]	70
Initial prestressing stress, σ_{PT} [MPa]	975
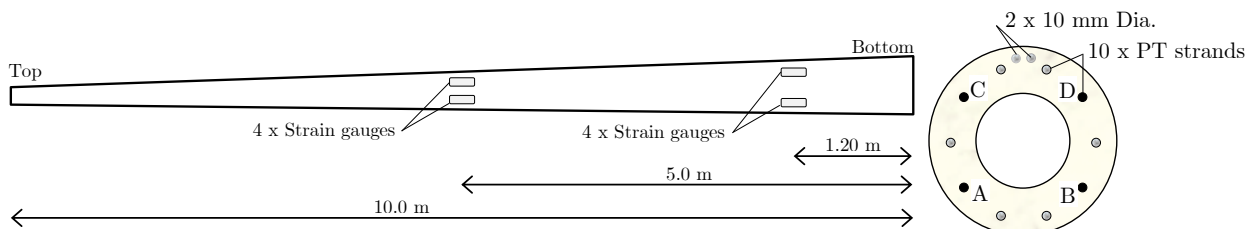
Fig. 5.2. Arrangement of the strain gauges of the laboratory poles: the location of the strain gauges along the pole (left), and the arrangement of the prestressing strands in the cross-section of the pole (right); the strain gauges are attached to the strands A, B, C, and D. The cross-section seen from bottom of the pole and matches the setup of the 3-point bending test.

5.3 Experimental Program

For the sake of the experimental program, the manufacturer provided the GRK1462 with four poles. These poles have the same characteristics and production conditions as the pole installed on site. To follow the development of the strains of the prestressing strands during and after the production, eight strain gauges were attached to four prestressing strands before casting the concrete in two positions: at the mid-height of the pole and at 1.2 m from the bottom of the pole, as shown in Fig. 5.2.

The experiments were conducted in cooperation with Versuchstechnische Einrichtung (VTE), which is the laboratory of the Institute for Structural Engineering of the Faculty of Civil Engineering at the Bauhaus-Universität Weimar. In the following, an overview of the conducted experiments, which are employed in this study, are described. Three types of the experiments were mainly selected: vibration test of the undamaged pole, 3-point bending test, the vibration test of the damaged pole.

5.3.1 Vibration Test

A pole was tested in a vibration test in free-free setup by hanging it in a horizontal position using two ropes as shown in Fig. 5.3. A set of twelve 1D accelerometers (type PCB Piezotronics 393A03) were attached to the pole to measure the accelerations in the horizontal and vertical directions, according to the test setup. Two of the sensors were fixed to the top end of the pole, and considered as reference sensors while the rest were configured in two measurement setups to increase the quantity and quality of the identified mode shapes and natural frequencies.

Moreover, a hammer with an appropriate hardness of impact tip was used to excite the structure in three positions in both horizontal and vertical directions. The procedure was repeated for each sensor-setup. In the first sensor-setup, the sensors were attached with an
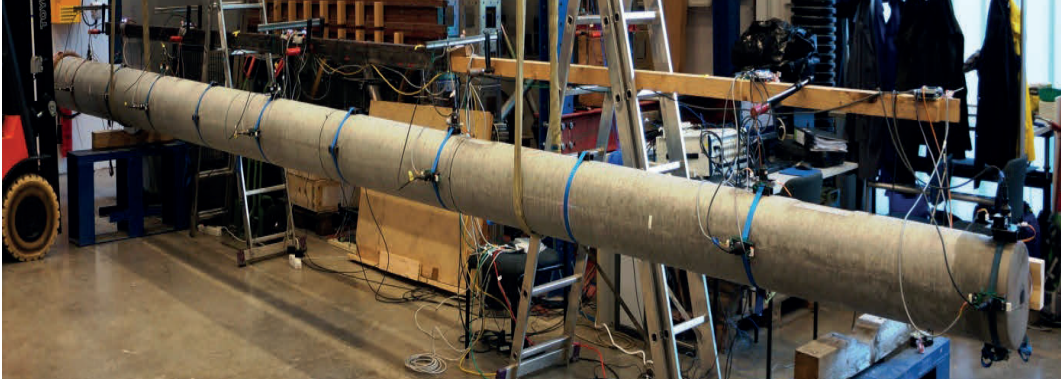
Fig. 5.3. Vibration test layout (Source: VTE).
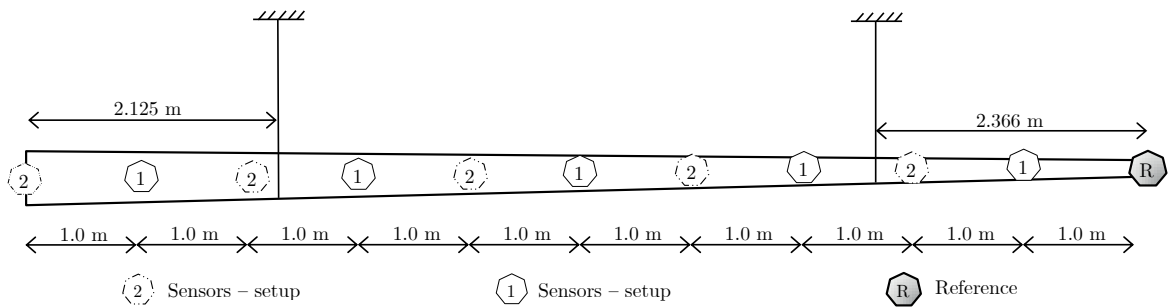
Fig. 5.4. The vibration test of the un-damaged pole – schematic experimental setup.

in-between distance of 2.0 m; then these sensors were moved 1.0 m towards the bottom of the pole to form the second measuring setup, as shown in Fig. 5.4.

Data was acquired at a sampling rate of 4096 Hz. The modal parameters were identified using the recorded accelerations from the two setups. The data were analyzed using the OMA, based on the output-only data. The covariance-driven version of the SSI method was implemented to compute the covariances of the identified system and modal parameters using the MACEC toolbox [171]. The modal parameters of the first five modes in both horizontal and vertical directions were identified. The results of the SSI analysis are shown in Figs. 5.5 and 5.6 for vertical and horizontal directions, respectively. The identified natural frequencies $\mathbf{f}$ and the damping ratios ζ are listed in Table 5.3.

5.3.2 3-Point Bending Test

Later, the same pole was tested in a 3-point bending setup. The setup was selected to verify the actual performance and to evaluate the actual material properties of the pole. This test has been used widely in the literature and verified by mathematical models [172], which
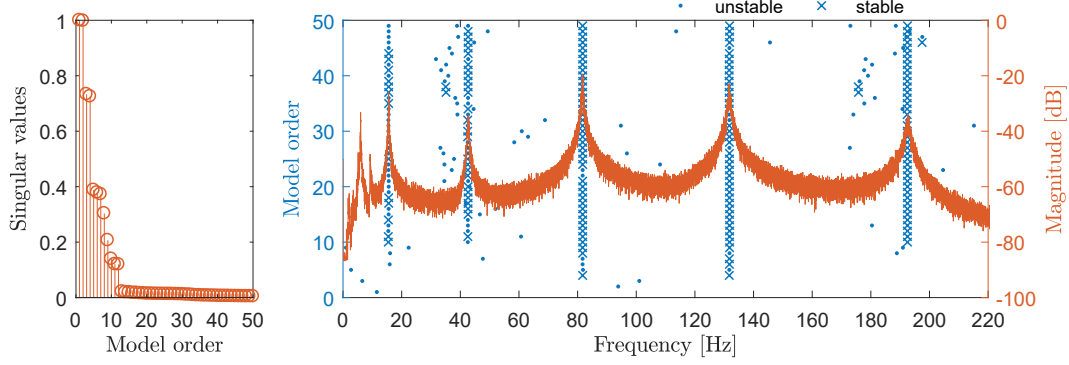
Fig. 5.5. The results of the SSI analysis of the un-damaged pole in the vertical direction: the singular values of the output covariance matrix (left), and the stabilization diagram (right).
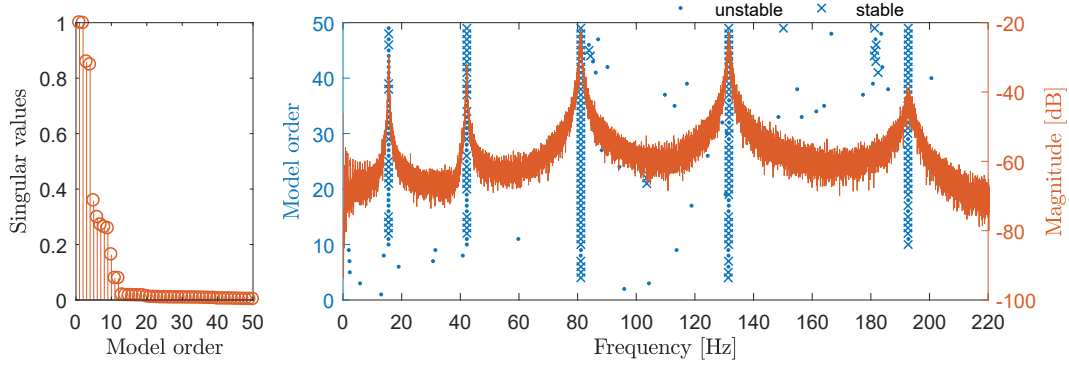
Fig. 5.6. The results of the SSI analysis of the un-damaged pole in the horizontal direction: the singular values of the output covariance matrix (left), and the stabilization diagram (right).

makes the results more understandable and offers more accurate interpretation. Furthermore, this setup also covers both linear and non-linear behavior of the concrete in tension and compression.

For the sake of DoE, a preliminary analysis of the pole using Response2000 was performed before conducting the test. This step was essential for building the most appropriate experimental setups. Response2000 is an advanced fiber model of prestressed sectional analysis with the effects of shear, and is based on the Modified Compression Field Theory (MCFT) considering biaxial stress-strain behavior throughout the depth of the beam [173]. Nominal material properties were used for the preliminary analysis, which gave the maximum concentrated load at mid-span of 67 kN, corresponding to a deflection of 102 mm at the failure of the beam, as shown in Figs. 5.7 and 5.8.

Based on the results of preliminary analysis, the experimental setup and applied displacements were developed. The pole was tested horizontally in a simply-supported setup.

5.3 Experimental Program

Table 5.3: The Natural frequencies **f** and the damping ratios ζ of the first five mode shapes of the un-damaged pole.

Mode shape [a]	1 - v	2 - v	3 - v	4 - v	5 - v	1 - h	2 - h	3 - h	4 - h	5 - h
f [Hz]	15.56	42.67	81.72	131.69	192.43	15.56	42.17	81.09	131.58	192.68
ζ [%]	0.87	0.72	0.28	0.38	0.47	0.33	0.33	0.36	0.26	0.81

[a] $(i - \text{v})$ is the ith mode shape in vertical directions, and $(i - \text{h})$ is the ith mode shape in horizontal directions, $i = 1, \cdots, 5$.
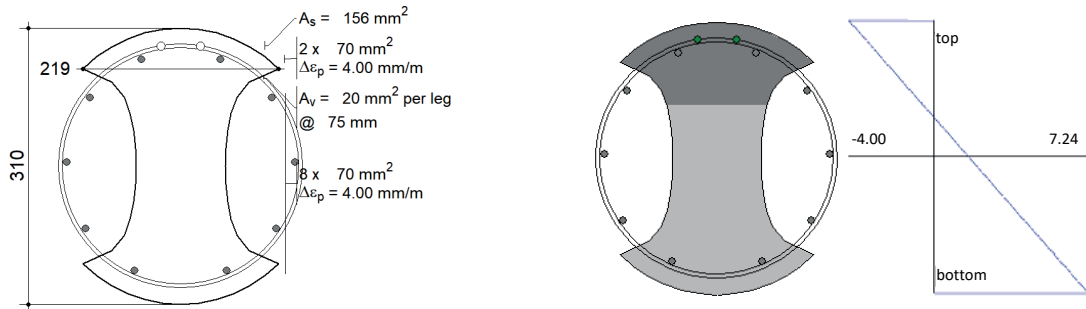
Fig. 5.7. The preliminary analysis of the beam in 3-point bending test setup using Response2000: the equivalent cross-section (left), and the cracked cross-section at failure point with the stress diagram in MPa (right).

The supports were made to fit the circular shape of the pole, as shown in Fig. 5.9. The pole was supported at 1.5 m from each of the ends, resulting in a mid-span of 7 m. The schematic experiment setup is shown in detail in Fig. 5.10.

The pre-specified displacements –shown in Fig. 5.11 (left)– were applied vertically at mid-span in steps by a servo-hydraulic piston, until the failure of the pole. Each step consisted of three identical loops. Each loop was ended by totally removing the applied displacement. The steps were carefully selected to cover the behavior of the structure in both the un-cracked and the cracked phases. Accordingly, concrete strains in the linear and
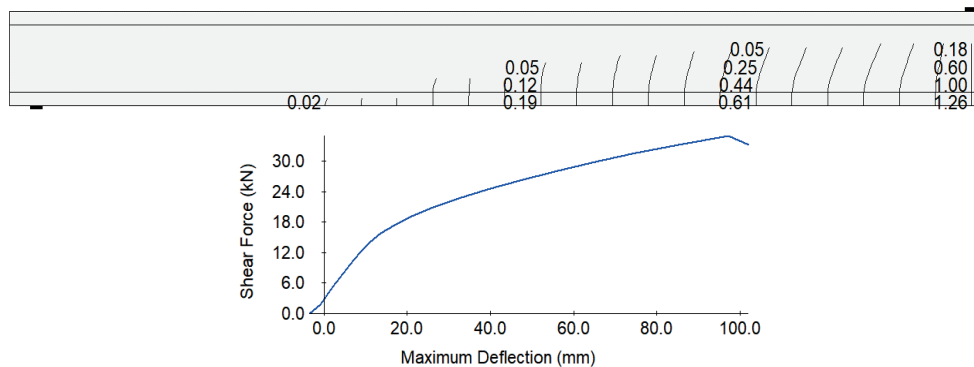
Fig. 5.8. The preliminary analysis of the beam in 3-point bending test setup using Response2000: the half of 7 m span with expected cracks at failure point (top), and the load-deflection curve (bottom).

63
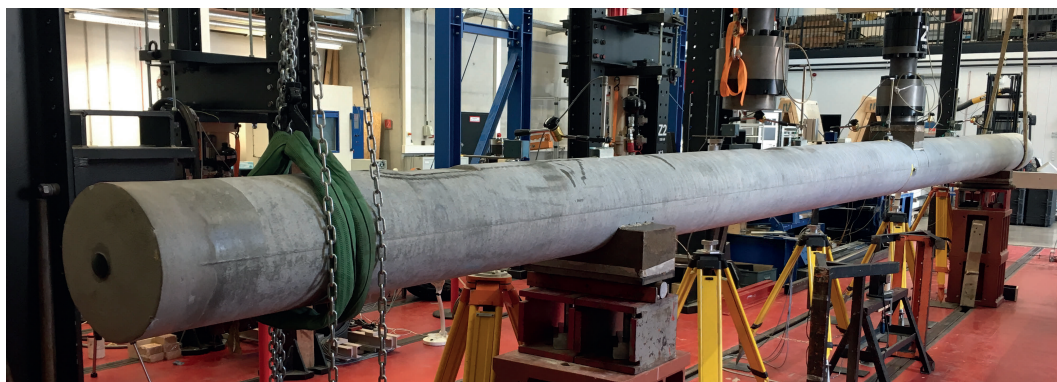
Fig. 5.9. 3-point bending test layout.
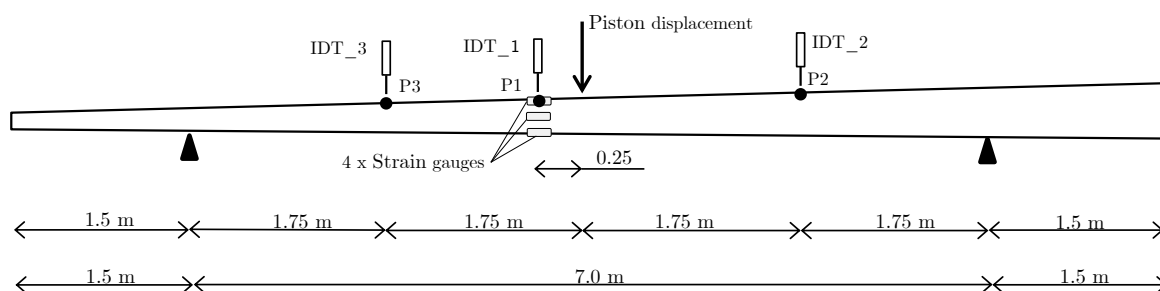
Fig. 5.10. 3-point bending test – schematic experimental setup.

non-linear phases were measured. The corresponding loads were measured from the load cell located at the piston and plotted in Fig. 5.11 (right).

Before conducting the test, the strains of the prestressing strands were recorded for strands A to D shown in Fig. 5.2 (right). The recorded strains were in the range $\varepsilon_{PT} = [2.5 - 3.6]$ ‰ with a mean value $\mu_{PT} = 3.08$ ‰ and a standard deviation $\sigma_{PT} = 0.41$ ‰.

During the test, deflection of the pole was recorded continuously, using Inductive Displacement Transducers (IDT) in three positions, P1, P2, and P3 as shown in Fig. 5.10. The point P1 matches the point of maximum deflection, due to the self-weight of the pole in the experimental setup. Points P2 and P3 correspond to the quarters of the mid-span. Deflections were only measured due to the applied displacements. Due to technical difficulties, the deflection under the self-weight of the structure was not measured at the beginning of the bending test.

In addition, strains on the outer surface of the concrete were measured using four strain gauges at position P1. Two strain gauges were attached one at each of the top and bottom of the pole in the experimental setup. The other two strain gauges were attached at the
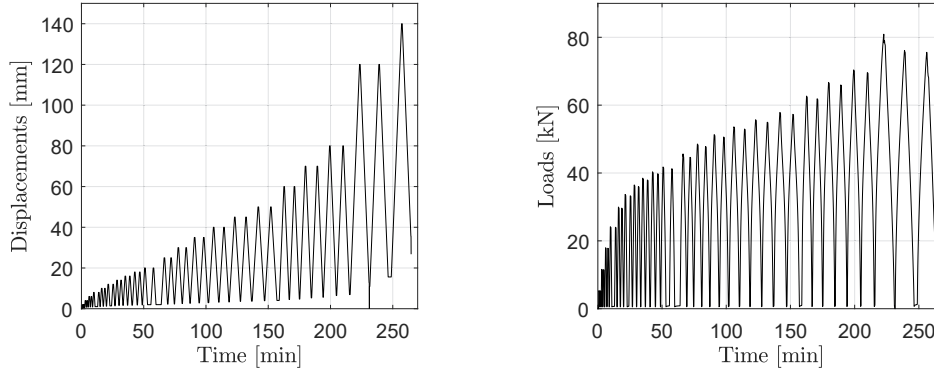
Fig. 5.11. The applied loading regime of the 3-point bending test: the applied displacements at the mid-span (left), and the corresponding piston loads (right).
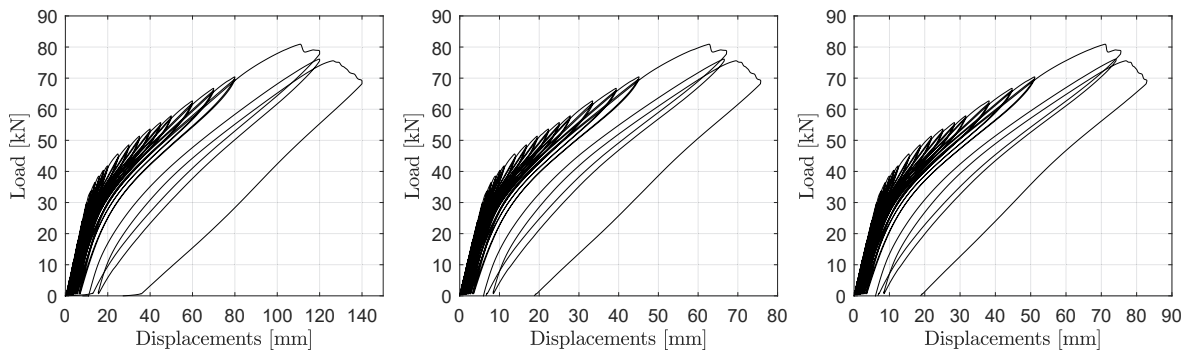
Fig. 5.12. The results of the 3-point bending test: load-displacement hysteresis curve presented at the points P1 (left), P2 (middle), and P3 (right).

mid-height of the cross-section from both sides.

As shown in Fig. 5.12, the maximum load was 81 kN corresponding to deflection of 110 mm, 63 mm, 71 mm at the points P1, P2, and P3, respectively. Development of strains of the prestressing strands is shown in Figs. 5.13 and 5.14 (right). The maximum strain reached 9.5 ‰ at the lower strands (A and B) and 4.6 ‰ at the upper strands (C and D). The sign convention for strain is as follows: tensile strain is positive whereas compressive strain is negative.

From Fig. 5.13 (right) and Fig. 5.14 (right), it is evident that the tensile strains of prestressing strands C and D decreased in the first part of the test, because they were located within the compression zone of the cross-section. This trend reversed, starting from the displacement corresponding to the load of 38 kN when the crack depth reached the level of these strands.

At failure, the strain in the most upper fiber of the cross-section at the point mid-span reached −3.0 ‰, which caused the concrete to fail under compression, as shown in Fig. 5.14
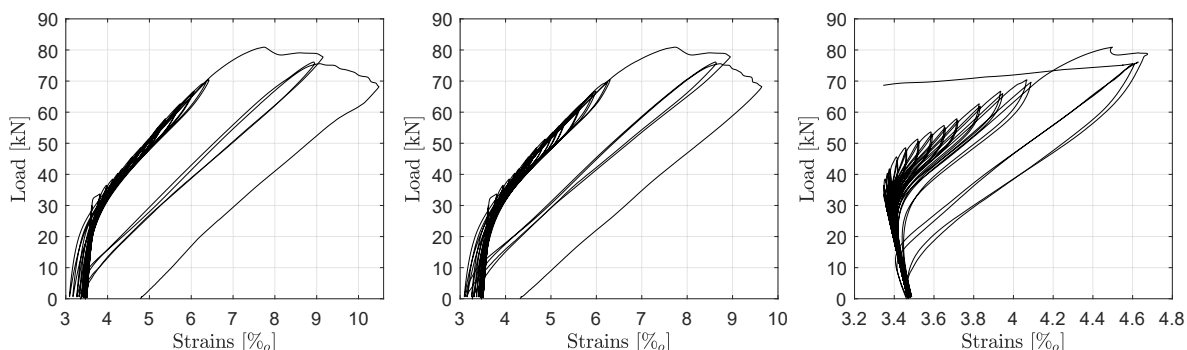
Fig. 5.13. The results of the 3-point bending test: the strains of the prestressing strands during the test measured at strand A (left), strand B (middle), and strand C (right).
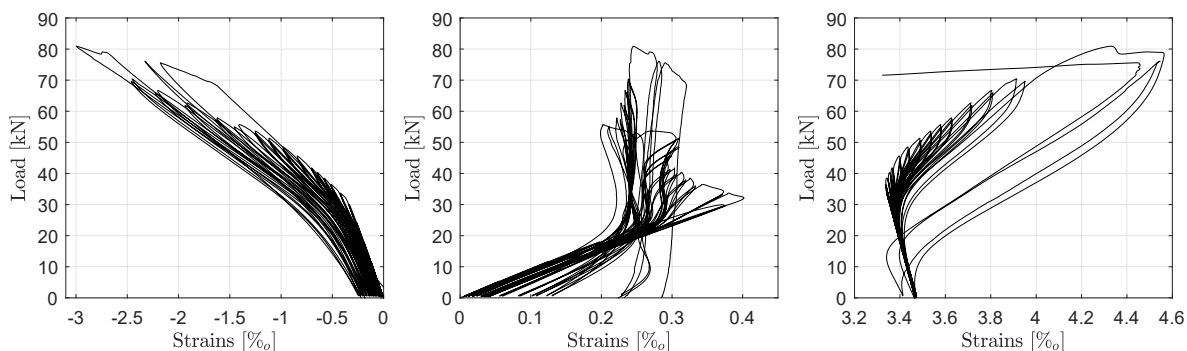
Fig. 5.14. The results of the 3-point bending test: the concrete strains at the top fiber at position P1 (left), the concrete strains at the bottom fiber at the position P1 (middle), and the strains of the prestressing strand D (right).

(left). The development of concrete tensile strains shown in Fig. 5.14 (middle) indicates that the section cracked seriously at strain 0.4 ‰ corresponding to a load of 35 kN. However, the results of this strain gauge after this point are not reliable, as it was partially damaged due to the cracks in the concrete.

It was evident that the measured loads and deflections were more than those calculated from the preliminary analysis by approximately 20%. These increments are ascribed to the differences between the 'real' properties of the structure and the nominal values mentioned in the datasheet. These differences indicate the importance of identifying the real geometry and material properties before evaluating the actual behavior of the structure.

For greater understanding and in-depth verification of the nature of the structure and the ongoing test, a deflection-wise sensitivity analysis is accomplished. This analysis is fundamental to this study as it shows the most dominant parameters at each step of the test. In this analysis, the envelope of the load-deflection hysteresis curve is discretized before implementing a sensitivity analysis. As a result, Sobol sensitivity indices, based on
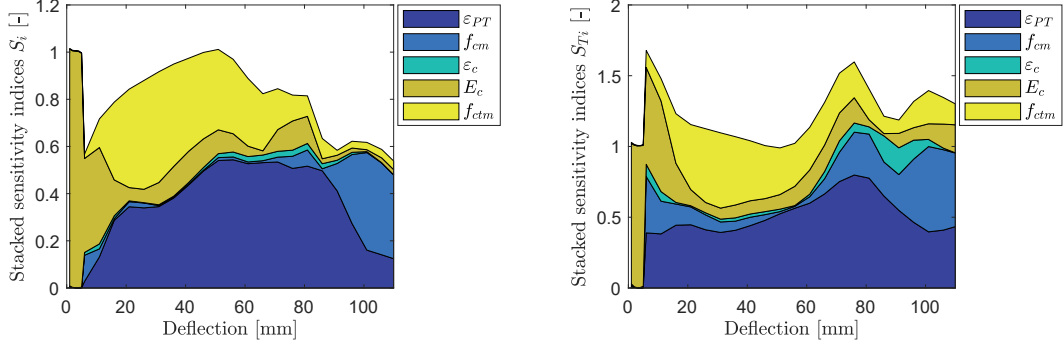
Fig. 5.15. Stacked sensitivity indices at the point P1: first-order sensitivity indices (left), and total effects sensitivity indices (right).
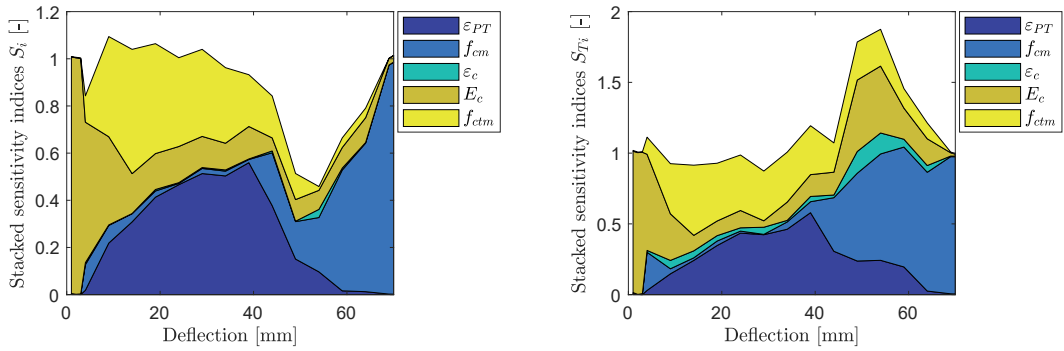
Fig. 5.16. Stacked sensitivity indices at the point P2: first-order sensitivity indices (left), and total effects sensitivity indices (right).

the variance method at each discretization point, are calculated.

The results of the sensitivity analysis at P1, P2, and P3 are shown in Figs. 5.15 to 5.17, respectively. As a conclusion, for the deflections measured at P1 (for example), the modulus of elasticity E_c is dominant in the first part of the test up to a deflection of 6 mm. For the deflection values between 6 and 80 mm, both the concrete tensile strength f_{ctm} and the prestressing initial strain ε_{PT} are the leading parameters. For the remainder, until failure point is reached, the compression strength of the concrete f_{cm} and the concrete strain at maximum compressive stress, ε_c become the most critical parameter.

The same interpretation covers the result of the point P3 in Fig. 5.17. The result at point P2 (shown in Fig. 5.16) differs a little at the last part, starting form deflection of 60 mm. This result is logical, as the cross-section at point P2 is larger and has fewer cracks in its vicinity compared to the smaller cross-sections at points P1 and P3.

Finally, the behavior of beams under the 3-point bending test has three main stages. In the first stage, the relation between the applied load and the deflection changes linearly.
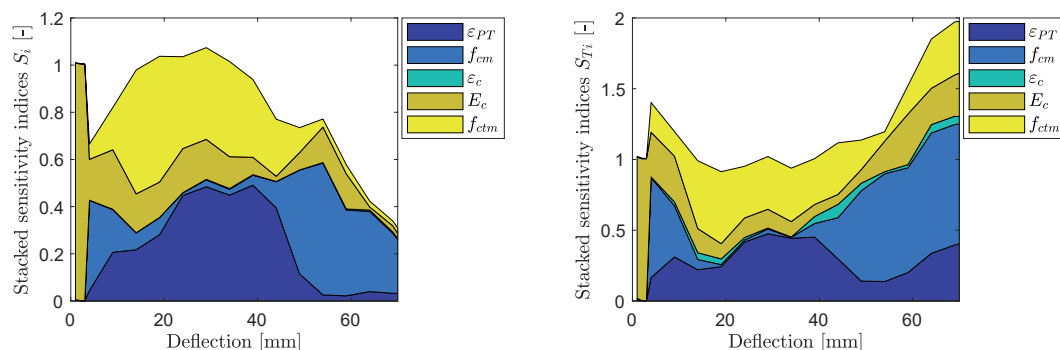
Fig. 5.17. Stacked sensitivity indices at the point P3: first-order sensitivity indices (left), and total effects sensitivity indices (right).

The slope of this curve is affected by the stiffness of beam, which makes this stage ideal for detecting the concrete modulus of elasticity. This linear behavior starts to change as the first crack occurs at the lower fiber of concrete, which makes this stage suitable for identifying the tensile strength of the concrete. In the second stage, the concrete cracks continue propagating, which leads to a nonlinear relation between the load and deflection. In the final stage, the load-deflection curve turns into a linear relation again, but with a much smaller slope, where a small increase in forces occurs against a dramatic increase in deflection.

5.3.3 Vibration Test of the Damaged Pole

During the 3-point bending test, it was recognized that most of the small cracks were recovered when the applied displacement returned to zero. Except for the main crack at the mid-span, which was clearly evident, it was found that most of the main cracks were closed again after the pole had been left for a period after completion of the test. The highly applied prestressing forces, and the elastic behavior of the prestressing strands worked efficiently to
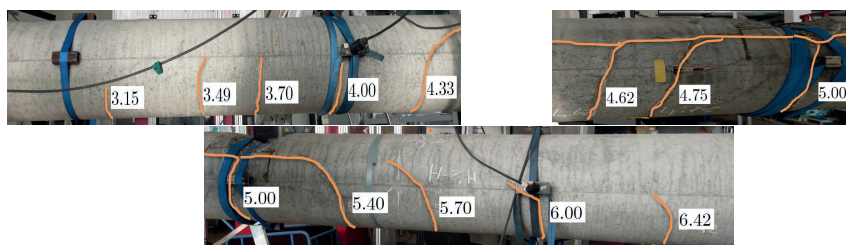
Fig. 5.18. The paths of the cracks (orange lines) at the failure of the pole under the 3-point bending test. The numbers on the photos represent the location of the cracks measured in meters from the top of the pole.
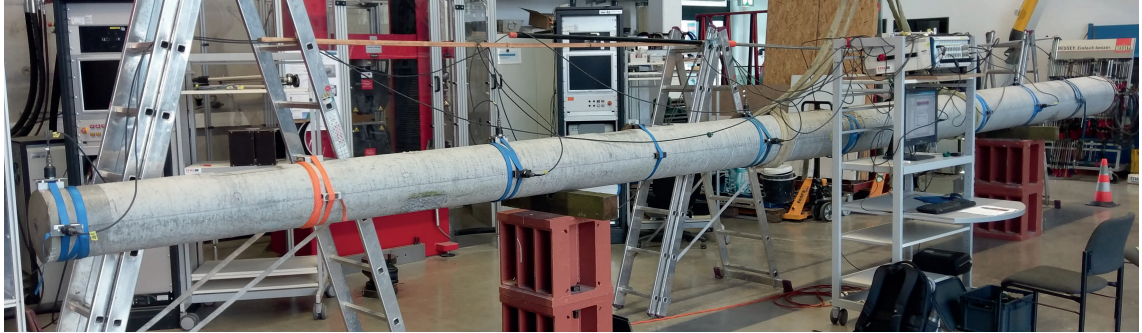
Fig. 5.19. The general arrangement of the vibration test of the damaged pole.

keep the cracks closed, which meets the requirement of the corrosion protection, mentioned previously in Section 5.1.1.

The paths of the cracks along the damaged pole are shown in close-up in Fig. 5.18. The main cracks are located at the second and third quarters of the tested span in the 3-point bending test, that is, between points P2 and P3, as shown in Fig. 5.10. The crack patterns are repeated in equal distances, mainly between 250 and 300 mm.

It is expected that the on-site poles follows the same behavior in case of cracking, which might affect the process of tracking the dynamic behavior of the poles considerably. This phenomenon gives the motivation to verify the impact of the '*recovered cracks*' on the modal parameters of the severely damaged pole. For this reason, the same vibration test on the damaged pole as had been previously conducted on the un-damaged pole was re-produced. The arrangements and detailed setup of the test are shown in Figs. 5.19 and 5.20.

The main goal is to compare the results of both damaged and un-damaged poles to present the changes in system identification and to propagate a damage detection indicator of the given structure. Accordingly, the observations of the test are analyzed using signal processing and SSI methods, which verifies the efficiency of each method in detecting changes in the dynamic behavior of the pole. The derived natural frequencies in vertical and
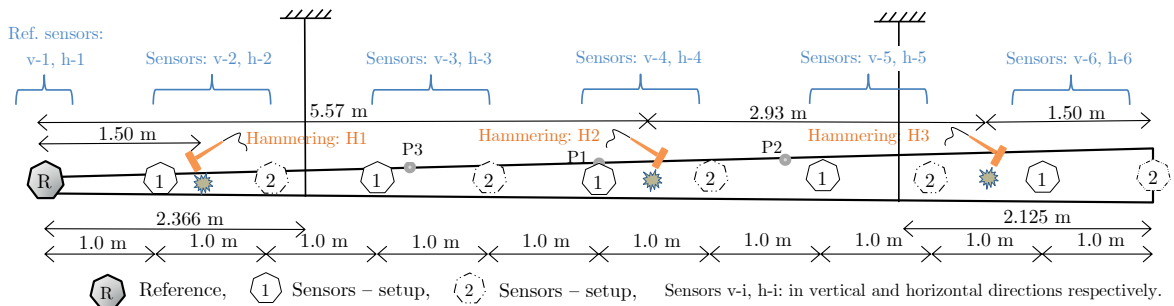
Fig. 5.20. The setup of the vibration test of the damaged pole.

Table 5.4: The natural frequencies **f** in [Hz] of the first five mode shapes of the damaged pole.

Method	Mode shape [a]									
	1 - v	2 - v	3 - v	4 - v	5 - v	1 - h	2 - h	3 - h	4 - h	5 - h
PSD [b]	14.40	43.20	78.60	130.50	186.20	15.40	42.00	80.60	131.60	191.10
SSI	14.42	43.01	78.36	130.75	186.43	15.44	42.13	80.64	131.26	191.31
Diff. [c] [%]	**7.33**	0.80	**4.10**	0.71	**3.12**	0.77	0.10	0.55	0.21	0.71

[a] $(i - \mathrm{v})$ is the ith mode shape in vertical directions, and $(i - \mathrm{h})$ is the ith mode shape in horizontal directions, $i = 1, \cdots, 5$.

[b] The average values of the different applied test setups and hammering positions.

[c] The difference is calculated in comparison to the measured values of the natural frequencies listed in Table 5.3.

Table 5.5: The damping ratios ζ of the first five mode shapes of the damaged pole.

Mode shape [a]	1 - v	2 - v	3 - v	4 - v	5 - v	1 - h	2 - h	3 - h	4 - h	5 - h
ζ [%]	0.47	0.40	0.31	0.29	0.38	0.47	0.35	0.32	0.34	0.48

[a] $(i - \mathrm{v})$ is the ith mode shape in vertical directions, and $(i - \mathrm{h})$ is the ith mode shape in horizontal directions, $i = 1, \cdots, 5$.

horizontal directions are listed in Table 5.4. The damping ratios ζ are listed in Table 5.5.

In Figs. 5.21 and 5.22, two examples of using the signal processing methods by utilizing the vertical accelerations, which were recorded by sensors v-2 and v-4. The signals of the hammering positions H1, H2, and H3 for each sensor were appended. Then, different signal processing techniques were implemented so that their benefits would help in detecting the natural frequencies of the structure in the applied test setup.

The results of the FFT and PSD techniques are almost the same. The peaks of the corresponding diagrams in Figs. 5.21 and 5.22 represent the natural frequencies of the damaged pole. However, the STFT technique has greater advantages as it additionally describes the change of frequencies over time. Moreover, it shows the dominant frequencies during the test and the suitable hammering positions for detecting the different natural frequencies.

As an example, the STFT results of sensor v-2 in Fig. 5.21 (right) show that the first and second natural frequencies are efficiently detected by exciting the structure at the second hammering position H2, whereas the third hammering position (H3) is optimal for detecting the fifth natural frequency of the structure. Fig. 5.22 (right) shows that for sensor v-4, the dominant natural frequencies detected by this sensor are the third and the fourth, especially from the excitation at the first hammering position H1. The fifth natural frequency is hardly detected using this sensor.

From Table 5.4, it is clear that the natural frequencies **f** (derived by the covariance-based SSI method and signal processing analysis) are almost the same. By comparing these results to the un-damaged case, it is evident that the main changes occurred in the odd-number natural frequencies, especially in the vertical direction. The maximum change corresponds to the first natural frequency and decreases for the third and the fifth.

Fig. 5.21. The analysis of the signals of the sensor v-2 in the vertical direction using signal processing methods: FFT analysis (left-top), PSD analysis (left-bottom), and STFT analysis (right).

The same trend is evident in Figs. 5.23 and 5.24 for the results of the SSI analysis for the vertical and horizontal directions, according to the test setup. In contrast, the changes in damping ratios ζ do not follow a clear trend as in the case of the natural frequencies **f**.

For a greater understanding of the dynamic behavior of the damaged pole, the mode shapes of the damaged and un-damaged pole are compared, as shown in Fig. 5.25. It is evident that the main changes of the mode shapes of the damaged pole occur at the coordination of 5 m at the mid-span. This reflects the significant influence of the main crack at this position.

In Fig. 5.26, the plot of the MAC analysis emphasizes that the even-number mode shapes are less sensitive to the main crack, as they have a modal node at the crack location, which indicates why significant changes of the natural frequencies are important for the odd-number modes. Besides, it can be seen that the horizontal direction has fewer changes in natural frequencies and mode shapes because the cracks are mainly in the vertical direction. They significantly reduce the stiffness of the pole in the vertical direction, compared to the horizontal direction.

Unequal changes to the different modes of the structure form a good indicator of the damage situation of the pole and can be developed to cover damage localization, and to some extent, damage severity. It is right that the tested pole is severely damaged, which is not the expected case for the real poles on site. However, these findings are promising
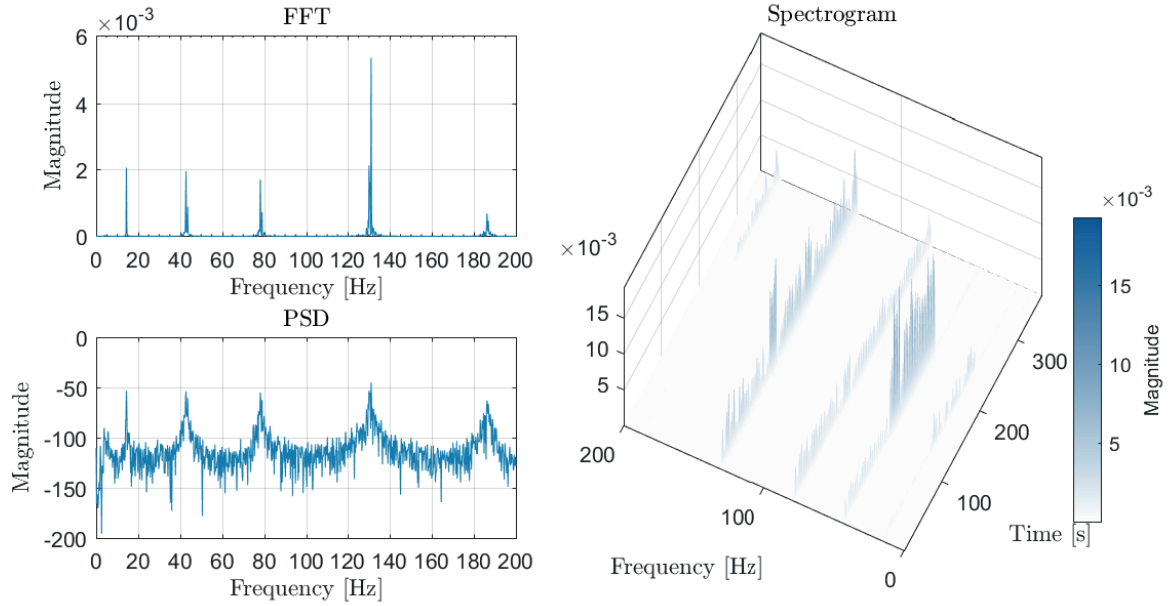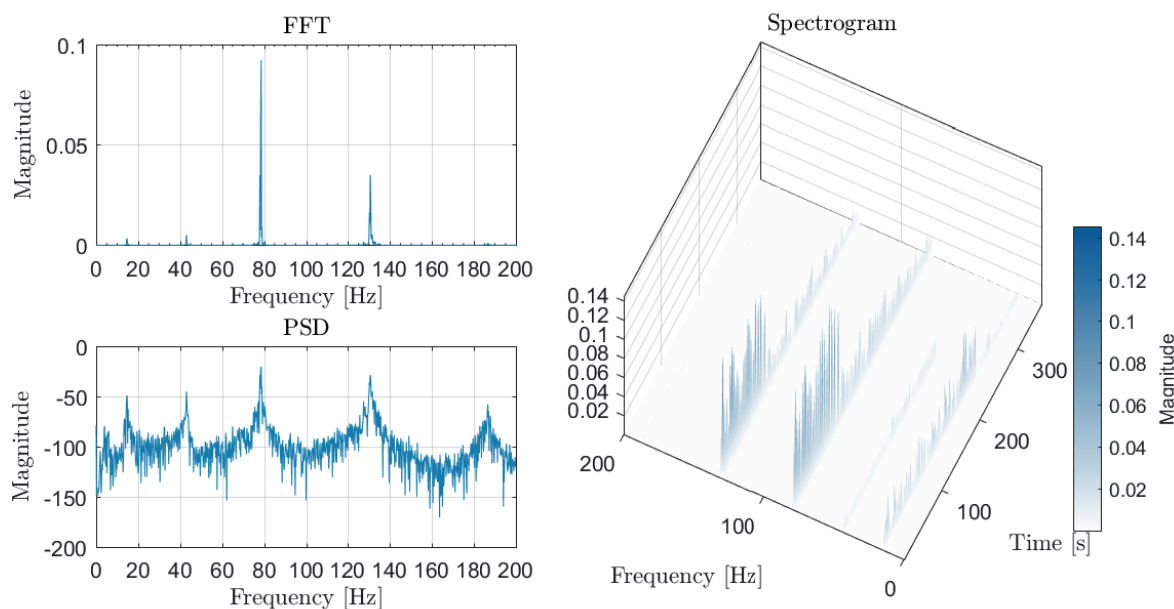
Fig. 5.22. The analysis of the signals of the sensor v-4 in the vertical direction using signal processing methods: FFT analysis (left-top), PSD analysis (left-bottom), and STFT analysis (right).

to invest more in the direction of building a *status detection* approach that supports the aim of this study in identifying the behavior and detection of the status of poles on-site, as described in Chapter 8.

5.4 Long-term Structural Health Monitoring System

The SHM system was installed on three successive poles along the new high-speed train track between Erfurt and Halle/Leipzig. This track is part of the project VDE 8.2, constructed by Deutsche Bahn (DB). The location and the arrangement of the selected poles M262-25, M262-27, and M262-29 are shown on the plan in Fig. 5.27. A general layout of the train track at the selected location is depicted in Fig. 5.28. The system collected the data from December 2015 to August 2018, mainly during the sunny weather(which is required to charge the system batteries).

The on-site part of the SHM system consists of a control cabinet that has the data acquisition unit, a local PC, batteries, solar panel, and temperature sensor. In this control unit, the data was collected from the sensors and stored temporarily. Then, the data wad collected frequently and stored permanently on a specific server in the university. The system was automatically triggered through photoelectric sensors attached to the poles M262-25 and M262-29. As a train-passed, the system began collecting data from the different sensors.

Fig. 5.23. The results of the SSI analysis of the damaged pole in the vertical direction: the singular values of the output covariance matrix (left), and the stabilization diagram (right).
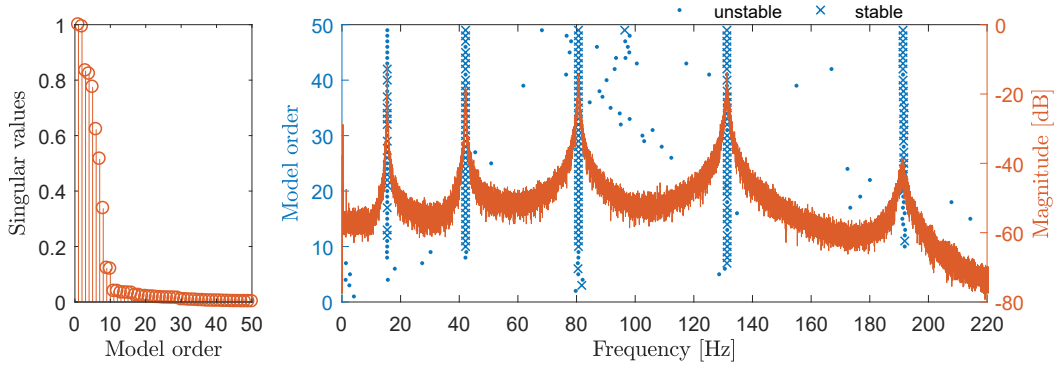
Fig. 5.24. The results of the SSI analysis of the damaged pole in the horizontal direction: the singular values of the output covariance matrix (left), and the stabilization diagram (right).

The attached SHM is illustrated in Fig. 5.29. In the following, a summary of the most important details of the SHM system is provided. However, full details can be found in [174, 175, 169].

The primary goal behind this SHM system was to track the behavior of the pole under train-induced effects and environmental conditions. Accordingly, different types of sensors were attached to the selected poles M262-25, M265-27, and M262-29. The vibration of the structure is detected mainly through two 2D accelerometers of type PCB Peizotronics 393A03. The accelerometers were attached at two levels to measure the change in horizontal accelerations of pole M262-27 in directions parallel and perpendicular to the train track.

Furthermore, strain gauges were attached to measure changes of the strain over time for each of the concrete outer surfaces, the prestressing strands, the foundation steel pipe, and additional reinforcement bars embedded into the concrete. Changes in temperature were measured by sensors attached to the concrete outer surface, and other sensors were embedded
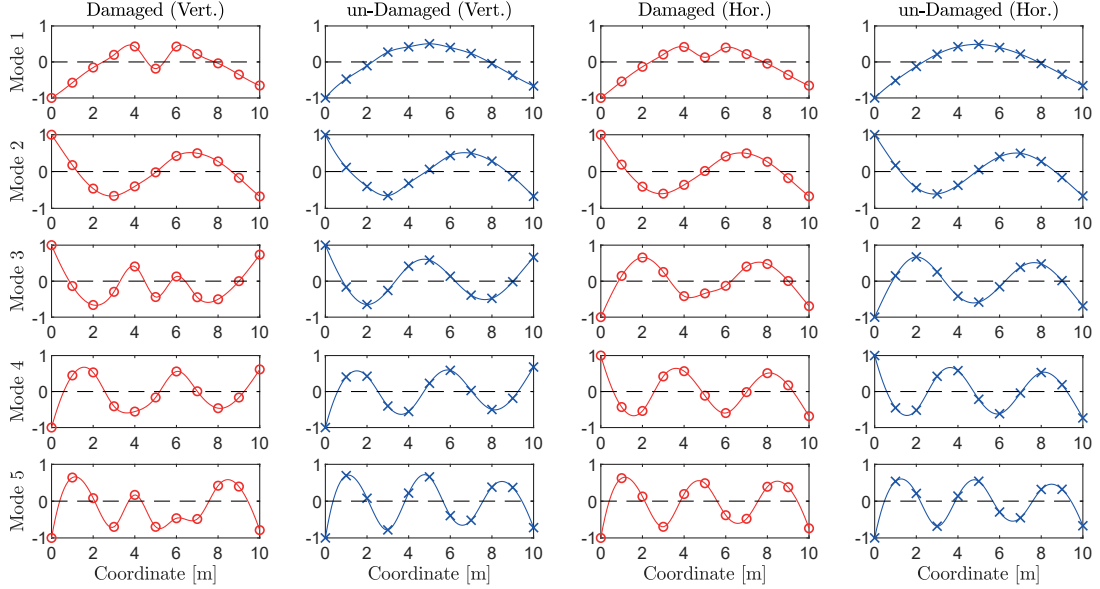
Fig. 5.25. The normalized mode shapes of the pole: the mode shapes of the damaged pole in vertical direction (left), the mode shapes of the un-damaged pole in vertical direction (middle-left), the mode shapes of the damaged pole in horizontal direction (middle-right), and the mode shapes of the un-damaged pole in horizontal direction (right).

into the concrete. Wind speed and direction were measured using a 3D anemometer attached to the top of pole M262-27. In addition, a 1D anemometer was also attached to the same pole at 4 m from the top, and one soil pressure sensor was attached at a depth of approximately 1.2 m below ground level.

Signals from the different sensors were synchronously recorded in two digital files for a period of eight minutes. The `.TST` file contained general information about the data sampling rate, recording time and length, and the date. Data collected from the sensors were stored in the form of a `.BIN` binary file. Signals from the temperature sensors were acquired in 1 Hz sampling rate, whereas the signals of the other sensors were mainly sampled in 1200 Hz. For a short period, the sampling rate is reduced to 600 Hz and then 300 Hz to study the effect of different rates on the results of the signal processing. The binary files were converted to `.mat` format using a pre-defined script. Then, the data was read, visualized, and analyzed in MATLAB packages [176].

5.5 Numerical Modeling

A 3D fully-detailed FEM model is built to simulate each of the experimental tests and poles on the site. The concrete material is simulated using volume elements with eight nodes, each with three degrees of freedom. The sizes of volume elements are approximately
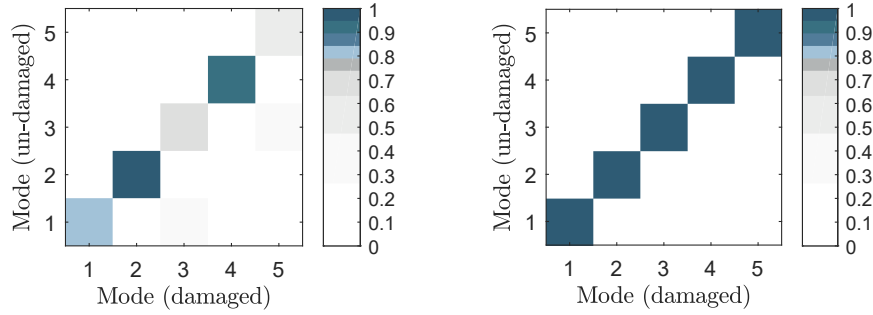
Fig. 5.26. The MAC matrix between the modes of the damaged pole (horizontal axis) and the un-damaged pole (vertical axis): the MAC values for the modes in the vertical direction (left), and the MAC values for the modes in the horizontal direction (right).
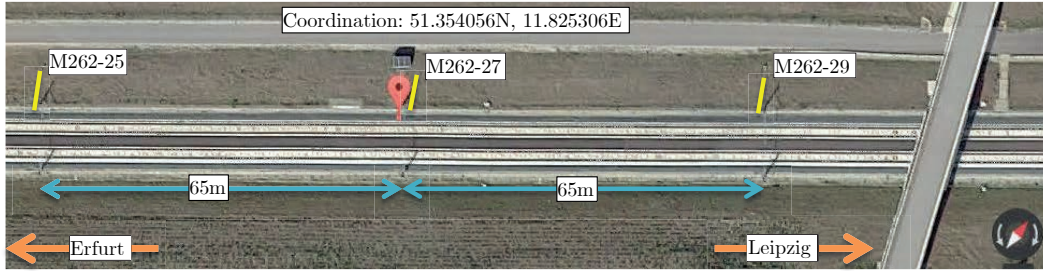
Fig. 5.27. The location of the SHM system.

$50 \times 50 \times 25\,\text{mm}$ in the longitudinal, circumferential, and radial directions, respectively. The volume elements sizes are selected based on the mesh convergence analysis shown in Fig. 5.30 to assure that the mesh size has no significant effect on the FEM results. Further, the prestressing strands are simulated using 3D truss elements with two nodes and three degrees of freedom at each node. The boundary conditions are selected in proportional to the simulated case, for example, the boundary conditions of the conducted experiments and the poles on-site.

The concrete constitutive model is carefully built to match the linear and nonlinear behavior of the concrete. Concrete damage plasticity (CDP) constitutive model is used in this study. The selected model covers both softening and hardening behavior of the concrete in tension and compression, respectively. The selected model covers two main failure mechanisms: tensile cracking, and compressive crushing [177]. Moreover, the selected concrete constitutive model has the advantage of simulating the material in the post-cracking phase, which is mainly required for the simulation pole in the 3-point bending test [178].

In the CDP constitutive model the evolution of the yield or failure surface is controlled by two hardening variables, $\tilde{\varepsilon}_t^{pl}$ and $\tilde{\varepsilon}_c^{pl}$, tensile and compressive equivalent plastic strains, respectively. The CDP assumes the elastic stiffness of the material to be degraded after the
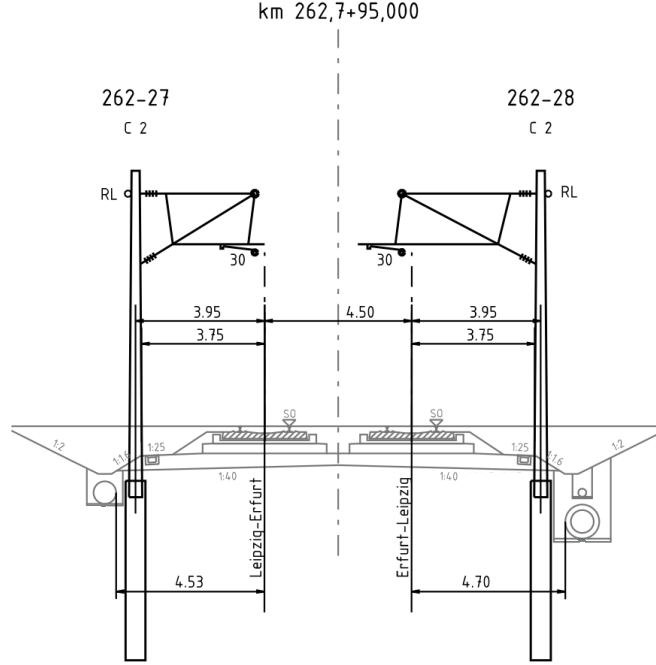
Fig. 5.28. The general layout of the train track at the location of the SHM system.

ultimate strength is achieved. The degradation of the elastic stiffness ($E = (1 - d)/E_o$) is described by two damage variables d_t and d_c, where E_o is the initial modulus elasticity of the concrete. The degradation parameters take values from zero, representing the undamaged material, to one, which corresponds to total loss of strength. The CDP requires the values of elastic modulus, Poisson's ratio, the plastic damage parameters and description of compressive and tensile behavior. The plastic damage parameters are the dilation angle, the flow potential eccentricity, the ratio of initial equibiaxial compressive yield stress to initial uniaxial compressive yield stress, the ratio of the second stress invariant on the tensile meridian to that on the compressive meridian and the viscosity parameter that defines visco-plastic regularization. In the absence of advanced materials tests, the values of these parameters were taken as recommended by ABAQUS documentation [179] and are set to $36°, 0.1, 1.16, 0.66$ and 0.0, respectively. Furthermore, it is essential to describe the stress–strain curve for material precisely.

The stress-strain curves of concrete in compression and tension are derived from the Fib Model Code 2010 [4]. As shown in Fig. 5.31 (right), it is assumed that the compression response of concrete is linear until the stress reaches a value of 30% of maximum concrete compressive strength f_{cm}. Then, the concrete in compression follows a parabolic curve until the material attains f_{cm} corresponding to a strain of ε_{c1}. Then, it is followed by strain-softening until the concrete reaches a crushing strain ε_{cu1} of 3.1 ‰. The behavior
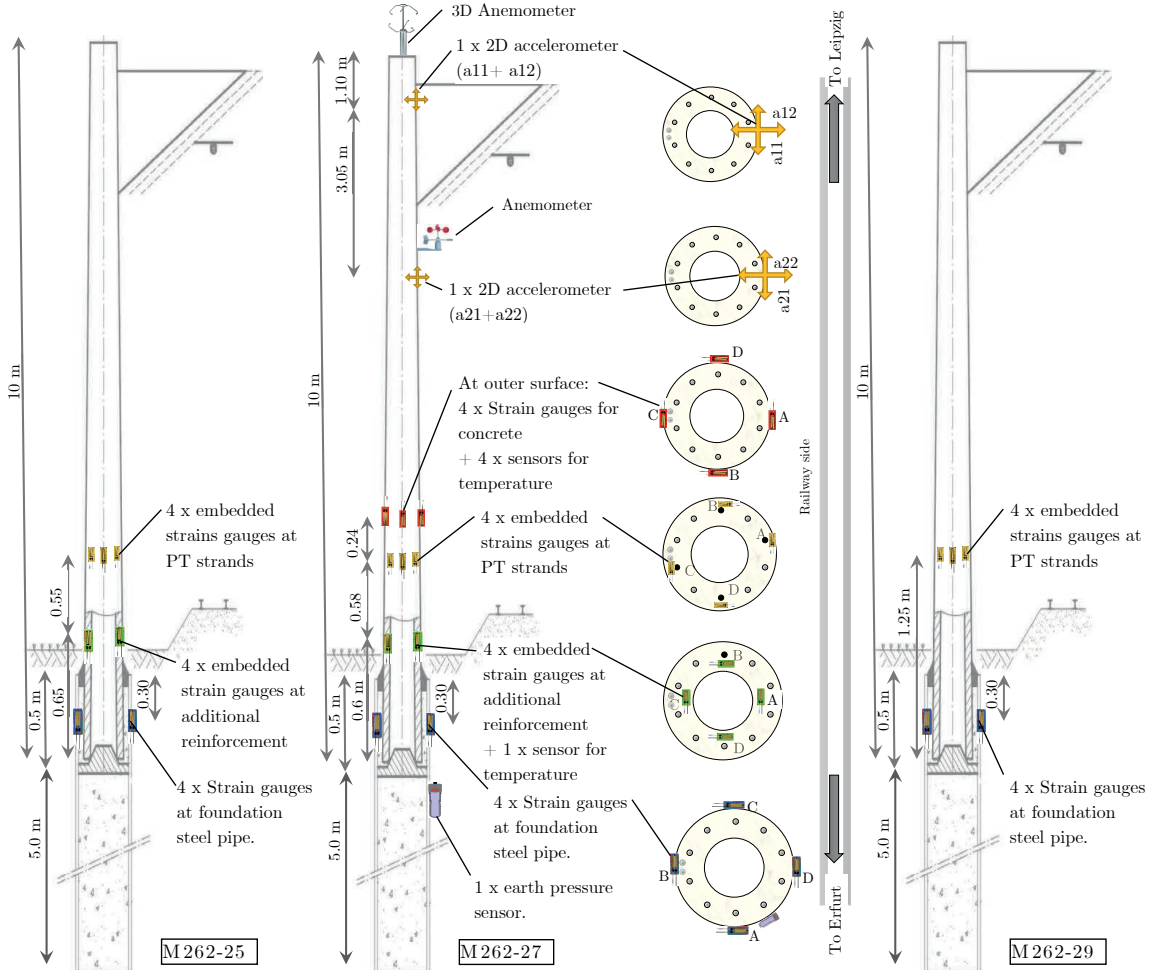
Fig. 5.29. The setup of the SHM system attached to the poles M262-25 (left), M262-27 (middle), and M262-29 (right). The cross sections (middle) show the location of the different sensors and their donations as used in the monitoring system.

of concrete in tension is considered linear until the mean tensile strength of concrete f_{ctm} (corresponding to tensile strain ε_{ct}) is reached. Then, it reduces linearly to the maximum tensile strain of the concrete ε_{ctu}.

Besides, the constitutive model of the steel is chosen to follow the elastic-plastic behavior to demonstrate the expected behavior during the 3-point bending test. The constitutive model of the steel is shown in Fig. 5.31 (left). The steel behaves linearly till the yielding stress f_y, corresponding to yielding strain $\varepsilon_{sy} = f_y/E_s$, is reached. Then, the plastic behavior of the steel starts till it reaches the fracture strain ε_{su}, corresponding to the fracture strain f_{su}.

For simulating the poles on-site, the catenary system is simulated using geometry and
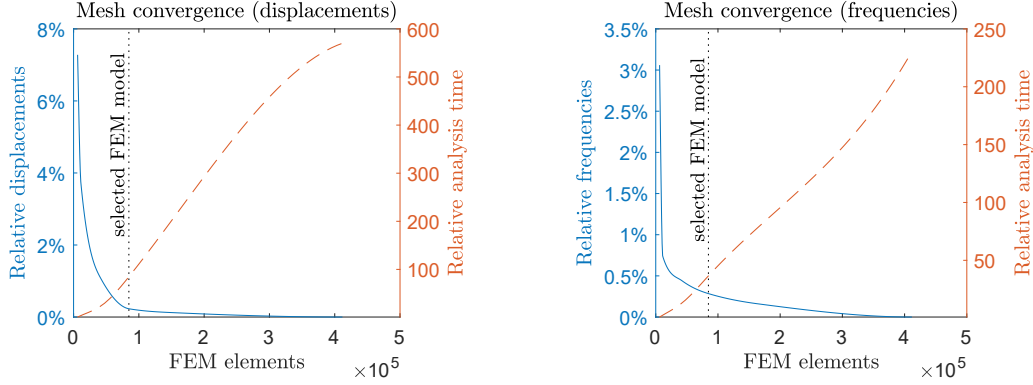
Fig. 5.30. Mesh convergence analysis: for the relative displacements of the pole (left), and for the relative first natural frequencies (right)
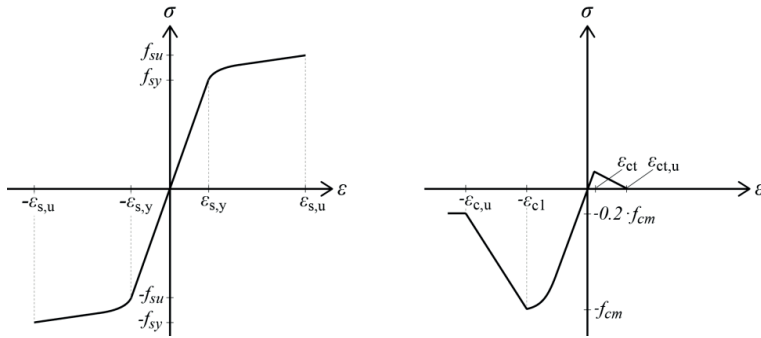
Fig. 5.31. The constitutive models of the materials: for the steel (left), and the concrete in tension and compression (right).

properties recommended by the literature [10, 11]. The cantilever attached the feeding wires to the pole is simulated as a truss circular hollow section elements, made of aluminum [180]. The cantilever truss is connected to the pole using hinge connectors, as described in the literature [181, 182]. Truss elements are used for simulating the cantilever (messenger) and contact wires with prestressing forces of 21 and 27 kN, respectively. The return wires are modeled as truss solid circular elements having axial forces calculated using the prescribed sagging and self-weight [183, 184, 185].

To accelerate the analyses in this study, surrogate models to overcome the heavy computations of the numerical models are built. The Kriging method is used to build non-parametric regression models (see, for example, [34] for more information). The quality of the regression models are evaluated by calculating the RMSE, the CoD, and the PoD of the different models.

5.6   Summary

In Chapter 5, the case study used in this research is described in detail. After providing a historical background of prestressed concrete poles and catenary poles, the geometry and properties of the poles under verification are listed. The experimental program of the experiments conducted within this work is described. Three experiments were conducted on a full-scale pole, namely, the vibration test of the un-damaged pole, the 3-point bending test, and the vibration test of the damaged pole. The measurements of the 3-point vibration test and the vibration test of the un-damaged pole are analyzed and prepared, and to be used in the PI in Chapter 7. The vibration test of the damaged pole verified the behavior of the pole in a damaged case. The analysis of corresponding measurements provides informative information to be used in developing the status monitoring approach in Chapter 8. In addition, the SHM system attached to the poles on-site is described in detail. This information to be read in conjunction with the analysis of recorded data in Chapter 6. Furthermore, the details of the numerical modeling techniques and the material constitutive models used in this study are outlined. The numerical models are essential for the PI in Chapter 7, and the simulation of the damaged pole in Chapter 8.

Chapter 6

Status Quo of the Pole

6.1 Introduction

In this chapter, the existing status of the poles monitored by the SHM system is verified. The acquired data are organized in a database, and the development of the strains of concrete and prestressing strands over the monitored period are presented. Then, the available data are analyzed using signal processing and SSI techniques to verify the behavior of the given poles during the monitoring period.

6.2 Database

The data recorded by the SHM system are organized in a database. The database is built to collect attributes of each record from data collected by the sensors, which makes classification and analysis more feasible. A table-based relational model is used to build the architecture of the database, which contains 8002 records from approximately 9000 files (the remaining files were not valid because of the wrong saving-format). The database is constructed with four types of tables that are linked together using the name of the file generated by the SHM system as a unique key that identifies each record.

   The main table provides a summary of the attributes of each listed file, such as the file name, date, sampling frequency, trigger type, temperature data, wind data, and train-passing data. The train-passing data are calculated for each listed file and classified as *no-train* or *is-train*. For is-train cases, the data are sub-classified based on number of passing trains, direction, speed, and length of the train. The sensor data derived from the corresponding `.BIN` binary files are stored in separate tables. Another type of tables is generated, which contains the results of SSI analysis for each file in both parallel and perpendicular directions. In addition, some statistical properties of each file (mean, maximum,

Fig. 6.1. Effect of the ambient temperature on the amplitude of accelerations in parallel direction X, as 2D and 3D scatter plots: for the sensor a11.

minimum values, and standard deviations) are stored in different tables.

In the following, the collected data are used to verify the existing status of the poles in-service as a result of environmental changes and different train passages.

6.2.1   Effects of Environmental Changes

Data collected in the database are used to detect the effects of environmental changes over time. The ambient temperature affects the amplitude of the recorded accelerations significantly, especially for temperature degrees above 25 °C. The same trend is derived for the data recorded by sensors a11, a12, a21, and a22 in both the parallel and perpendicular directions, as shown in Figs. 6.1 and 6.2 for sensors a11 and a12, and in Figs. 6.3 and 6.4 for sensors a12 and a22, respectively. In addition, the 3D scatter plots in Figs. 6.1 to 6.4 show that the derived trend is repeated annually.

No clear trend has been recorded for the relationship between changes in the strains of prestressing forces and changes in the ambient temperature, as shown in Figs. 6.5 and 6.6 for the DMS A, B, C, and D (for the location of the DMS, see Fig. 5.28). However, it is noted that changes to the prestressing strains decrease over time, which reflects the degradation of prestressing losses over time (see, for example, DMS A and C in Fig. 6.5 (left) and Fig. 6.6 (left)).

Ambient temperature has an impact on the strains recorded by the strain gauges attached to the concrete surface of the pole; that is, DMS A, B, C, and D (for the location of the DMS, see Fig. 5.28). Concrete strains increase by increasing the temperature, which is logical. This correlation is shown from the results of DMS A and C, as shown in Fig. 6.5 (left), and Fig. 6.6 (left).
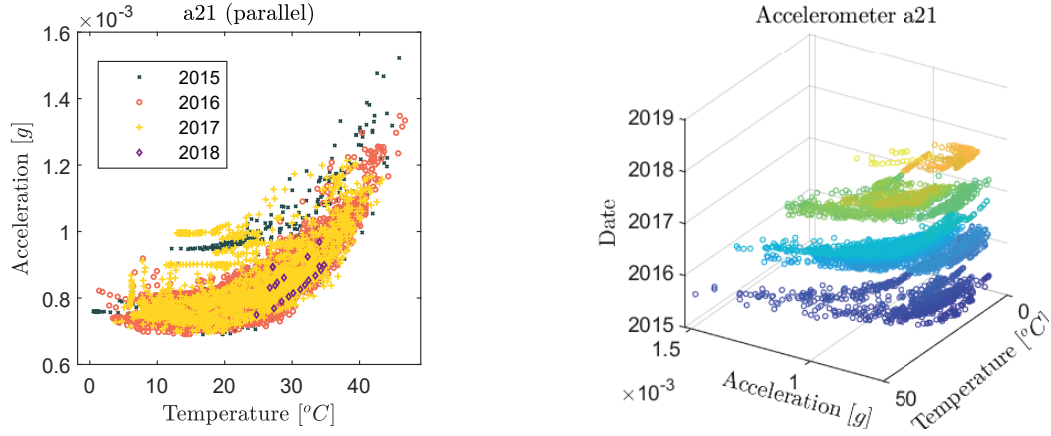
Fig. 6.2. Effect of the ambient temperature on the amplitude of accelerations in parallel direction X, as 2D and 3D scatter plots: for the sensor a21.
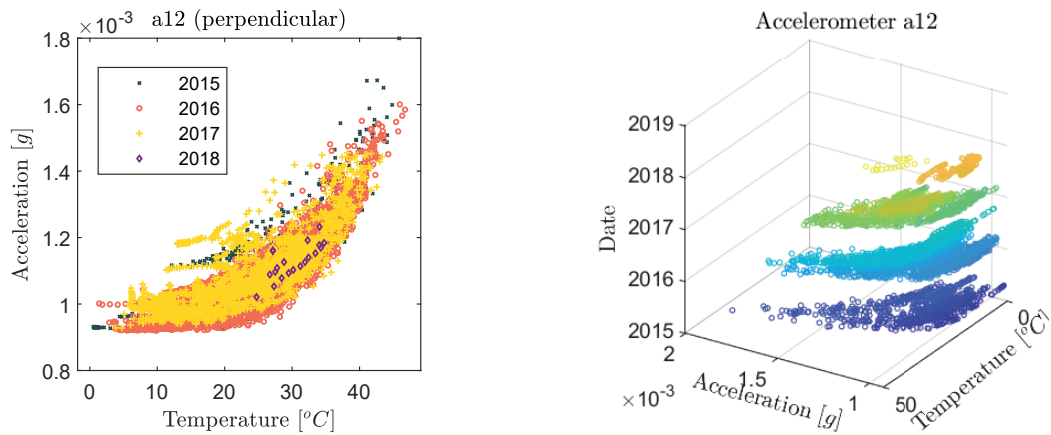
Fig. 6.3. Effect of the ambient temperature on the amplitude of accelerations in parallel direction Z, as 2D and 3D scatter plots: for the sensor a12.

As noted previously for the prestressing strains, the development of concrete strains between 2015 and 2018 in Figs. 6.7 and 6.8 shows a significant change between the strains in 2015 compared to the following years, which is associated with changes in the prestressing losses over time. It should be noted that the strains recorded by DMS D seem to be unreasonable compared to the other DMS sensors, which means that this sensor is likely to be in error and consequently is not considered in the interpretation of the pole behavior.

The scatter plot in Fig. 6.9 (left) and the histogram in Fig. 6.9 (middle) summarizes the recorded wind speed and direction over the specified period of monitoring. In addition, in Fig. 6.9 (right) the wind speed is plotted against the date of recording. The major wind comes from the southwest direction, and the maximum-recorded wind speed reached $18\,\mathrm{m\,s^{-1}}$ in 2018. It should be mentioned that according to the recorded data, no clear
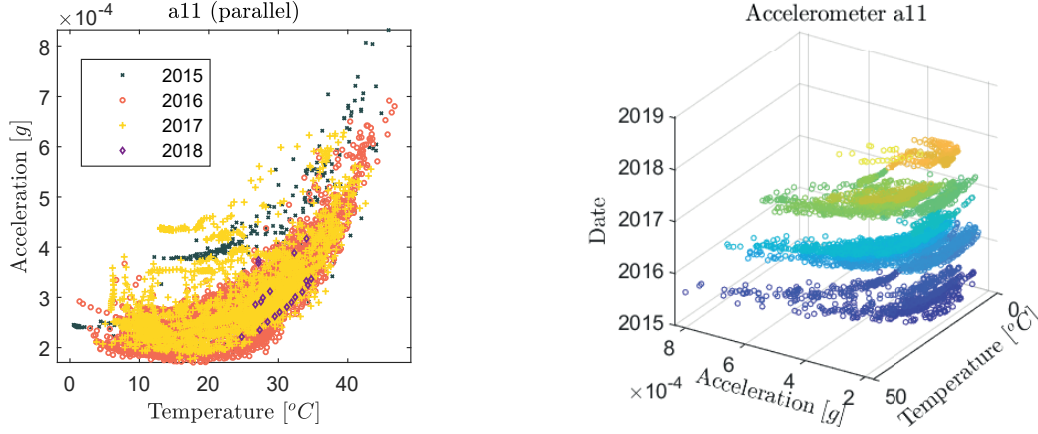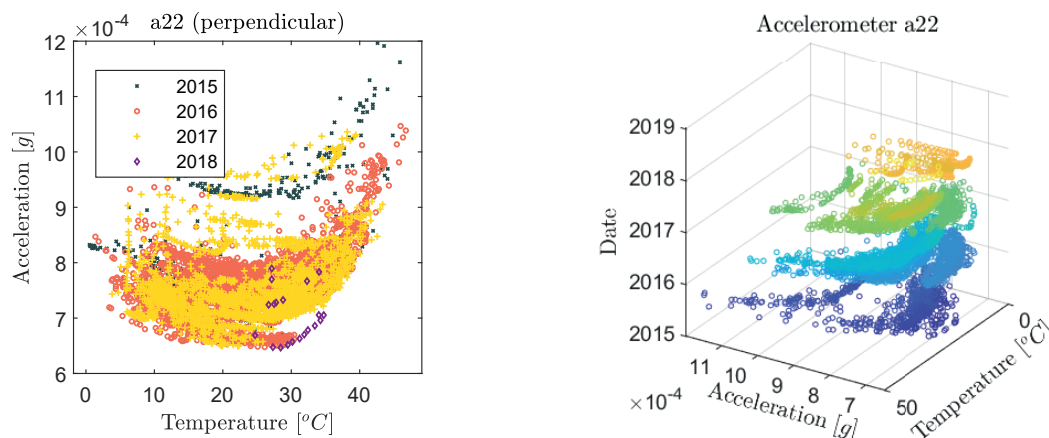
Fig. 6.4. Effect of the ambient temperature on the amplitude of accelerations in parallel direction Z, as 2D and 3D scatter plots: for the sensor a22.
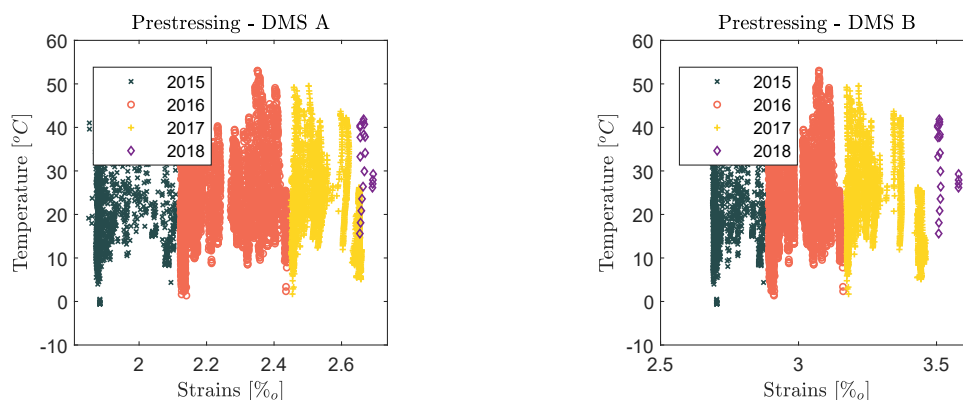
Fig. 6.5. Relation between the prestressing strains and ambient temperature at DMS A (left) and DMS B (right).

relationship can be identified between changes in the system and wind, which maintains the ambient temperature as the principle cause of changes in the entire system.

6.2.2 Effects of Train Passing

As shown in Figs. 6.10 and 6.11, the most commonly recorded train lengths are 180, 315, and 365 m. It is evident that the different train lengths have no effect on the amplitude of the measured acceleration in both the parallel and perpendicular directions. The same conclusion can be drawn from Figs. 6.12 and 6.13, as no trend can be detected between the train speed and the amplitude of the measured accelerations. However, the most frequent train speeds are 230, 200, 180, and $160 \, \mathrm{km \, h^{-1}}$.
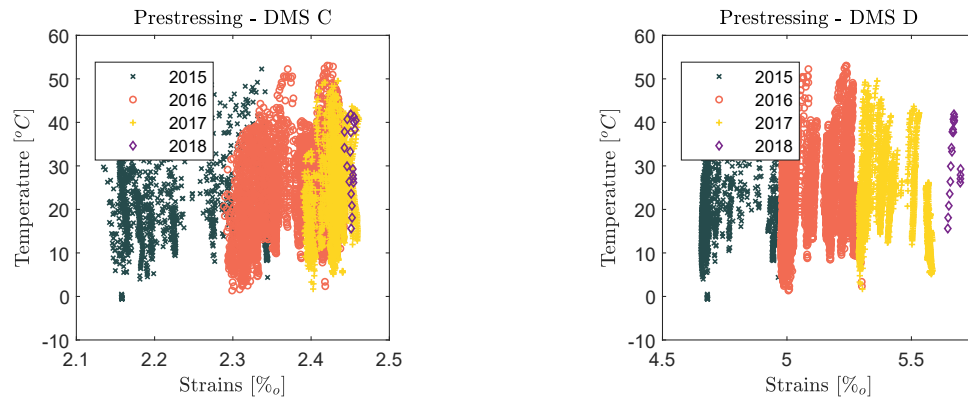
Fig. 6.6. Relation between the prestressing strains and ambient temperature at DMS C (left) and DMS D (right).
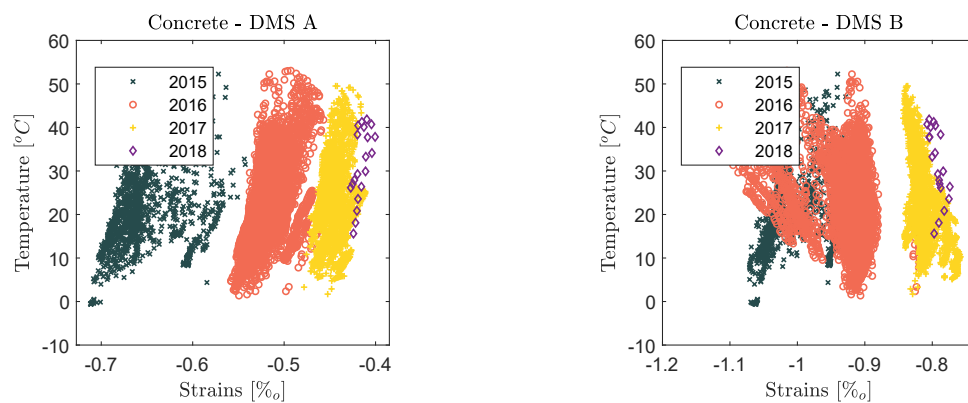
Fig. 6.7. Relation between the concrete strains and ambient temperature at DMS A (left) and DMS B (right).
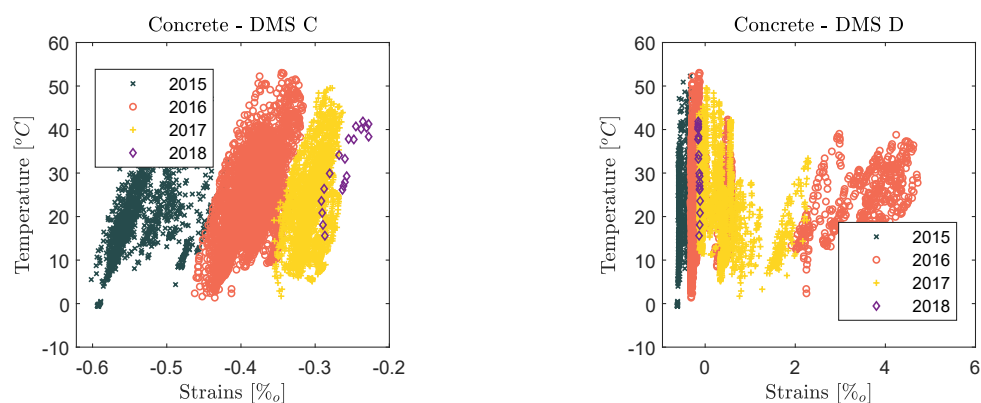
Fig. 6.8. Relation between the concrete strains and ambient temperature at DMS C (left) and DMS D (right).
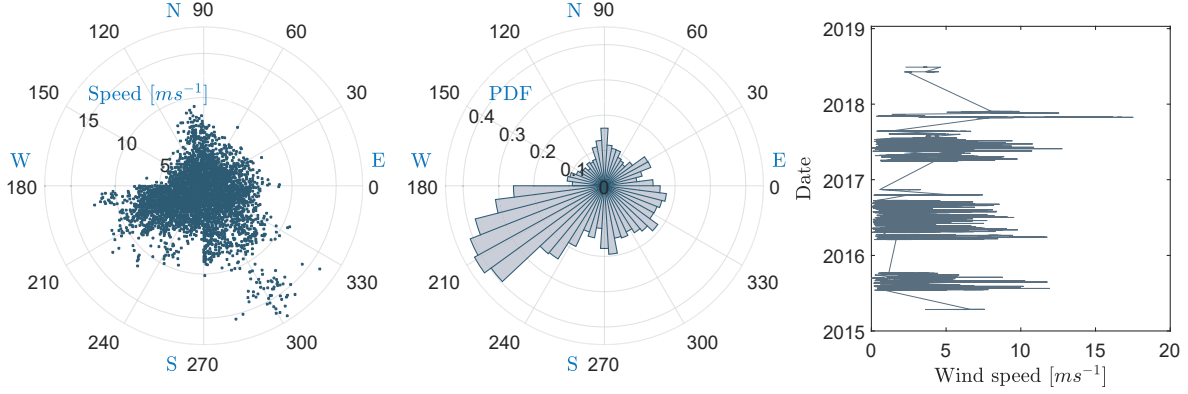
Fig. 6.9. Recorded wind data: speed and direction (left), histogram of wind directions (middle), and wind speed over time (right).
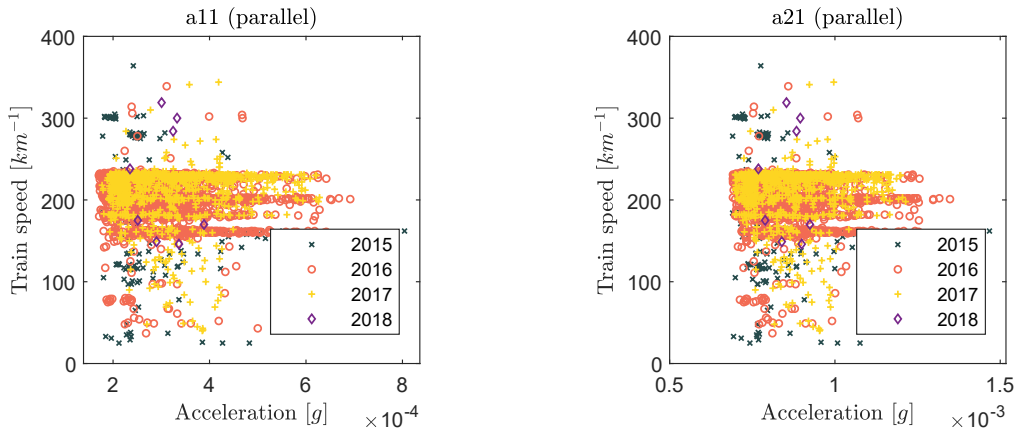
Fig. 6.10. Relation between train length and amplitude of accelerations: for sensors a11 (left) and a21 (right) in the parallel direction X.

6.3 Data Analysis Using Short-Time Fourier Transform

Using STFT described in Chapter 3, the preliminary analysis of accelerations recorded by the SHM system is completed from which the natural frequencies of the given structure are identified. A set of 45 records are selected based on date, train speed, train length, number of passing trains, and long duration records. Using these records, seven combinations are built to cover the most recorded cases of the train passing.

An example of the STFT analysis of a long-time record (900 s) with one train passing is shown in Fig. 6.14. The signal processing analysis can efficiently detect the first and second natural frequencies of the pole. However, some additional frequencies appear on the spectrogram during the train passing. To detect the effect of the train passing, the record is divided into two parts: the part during the train passing, and the part after the train

Fig. 6.11. Relation between train length and amplitude of accelerations: for sensors a12 (left) and a22 (right) in the perpendicular direction Z.
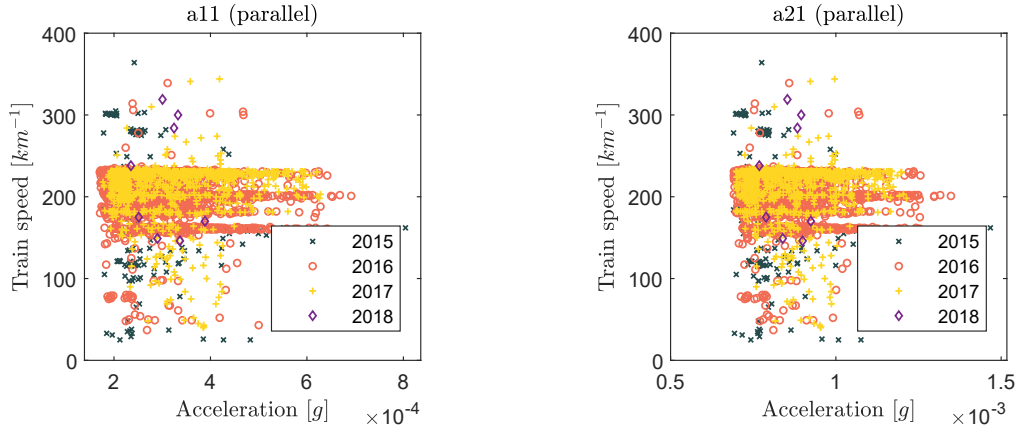
Fig. 6.12. Relation between train speed and amplitude of accelerations: for sensors a11 (left) and a21 (right) in the parallel direction X.

passing.

In Fig. 6.15, the natural frequencies of the pole detected using the sub-record after the train passing are in better quality compared to the previous results of the full record. To investigate this in more depth, the sub-record during the train passing is analyzed, as shown in Fig. 6.16. It is noted that the newly apparent frequencies between 0 and 10 Hz are more dominant than the natural frequencies of the pole. Accordingly, the ambient vibration (that is, the signal part after the train passing) is more appropriate for detecting natural frequencies than using the full signal that contains the train passing part. It can be said that train passing behaves as an added noise in the detection process. Consequently, it is recommended to use the signal outside the train passing period to obtain natural frequencies of the pole in better quality.
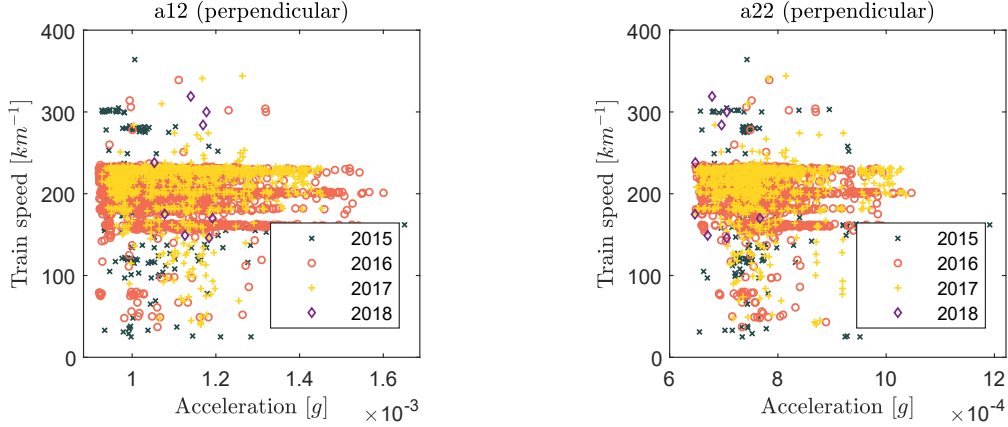
Fig. 6.13. Relation between train speed and amplitude of accelerations: for sensors a12 (left) and a22 (right) in the perpendicular direction Z.

To conclude the results of the STFT analysis, the development of natural frequencies in both the parallel and perpendicular directions is plotted in Fig. 6.17 using the derived mean values bounded by one standard deviation. The first and second natural frequencies are derived with a lower standard deviation compared to the third and fourth. In addition, no significant change in mean values of natural frequencies over the monitored period is detected.

To study the correlation between acceleration records, the concept of signal coherence is used. For each record, the coherence between signals of sensors in each direction is calculated; for example, the coherence between a11 and a21. Then, the normalized absolute change in the area under the coherence curve between different records is calculated. The closer the values are to one, the greater the correlation to the signals. It is noted that the most derived coherence values are above 0.6 in both the parallel and perpendicular directions (see Fig. 6.18), which reflects a high level of correlation between the signals of the given records. Therefore, it can be said that no significant change in the behavior of the poles can be detected.

6.4 Data Analysis Using Stochastic Subspace Identification

Accelerations recorded in the database are analyzed using the SSI procedure described in Section 5.3.1. Data recorded by sensors a11, a12, a21, and a22 (shown in Fig. 5.28) are utilized to identify natural frequencies, damping ratios, and the mode shapes of the pole in both the parallel and perpendicular directions to the train track, namely, X and Z, respectively. The results are summarized in Table 6.1 for the first four modes.

Fig. 6.14. Analysis of a full-record during train passing in the parallel direction X using signal processing methods: FFT analysis (left top), PSD analysis (left bottom), and STFT analysis (right).

Table 6.1: Dynamic characteristics of the pole using SSI: natural frequencies **f**, and damping ratios ζ. Symbols μ, σ denote mean values and standard deviations, respectively

i^{th} mode	Parallel direction X				Perpendicular direction Z			
	1st	2nd	3rd	4th	1st	2nd	3rd	4th
$\mu_{\mathbf{f}}$ [Hz]	4.13	18.28	44.78	86.73	3.33	17.02	41.74	87.25
$\sigma_{\mathbf{f}}$ [Hz]	0.07	0.24	0.82	1.62	0.06	0.19	1.64	1.34
μ_{ζ} [%]	2.01	1.38	1.66	0.93	4.19	1.79	1.84	1.04
σ_{ζ} [%]	1.17	0.75	0.91	1.18	0.93	0.71	0.87	0.91

The derived natural frequencies over considered time for both the parallel X and the perpendicular Z directions are plotted in Fig. 6.19. The values perturb around a mean value and have no trend, precisely as found in the previous STFT analysis. Moreover, it is noted that the third and fourth natural frequencies have more significant variances compared to the first and second ones. The main reason is the insufficient excitation required to identify the third and fourth natural frequencies of a good quality.

The records, in which the first four modes are identified, are selected to study the correlation between the mode shapes. Accordingly, the MAC values are calculated and plotted, as shown in Figs. 6.20 to 6.23, and as can be seen reach a value of one for all records (at least for the well-identified mode shapes, that is, the first and second modes). This means that the mode shapes are fully correlated, which shows that the pole has no damage and emphasizes that the perturbation of the natural frequencies is caused by environmental changes.
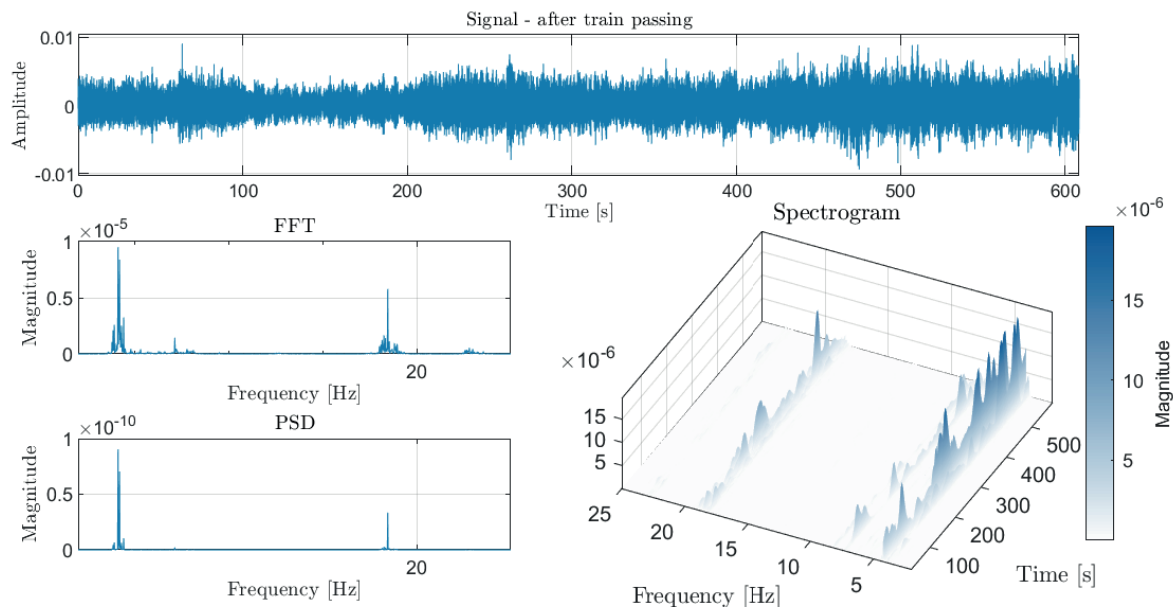
Fig. 6.15. Analysis of a sub-record after train passing in the parallel direction X using signal processing methods: FFT analysis (left top), PSD analysis (left bottom), and STFT analysis (right).

However, the MAC values of the third and fourth modes show less correlation as they have values between 0.7 and 1. It should be mentioned that the third and fourth mode shapes are not as clearly identified, precisely as in the situation of natural frequencies, as already mentioned. This is clearer in the third mode shape compared to the fourth, where most of the MAC values are between 0.9 and 1.

Furthermore, the scatter plots in Figs. 6.24 and 6.25 show no direct relationship between the changes in natural frequencies and the ambient temperature, which means that seasonal variations are most likely to be the reason behind the derived changes over time. An example is shown in Fig. 6.26 for the first mode shape in the perpendicular direction.

Finally, to describe the changes of dynamic characteristics of the pole over the monitored period, the derived natural frequencies are fitted to probability distributions, as shown in Figs. 6.27 and 6.28 for both the parallel and perpendicular directions, respectively. The derived PDF values are used in defining the un-damaged behavior of the poles that are used for the status monitoring algorithm in Chapter 7.
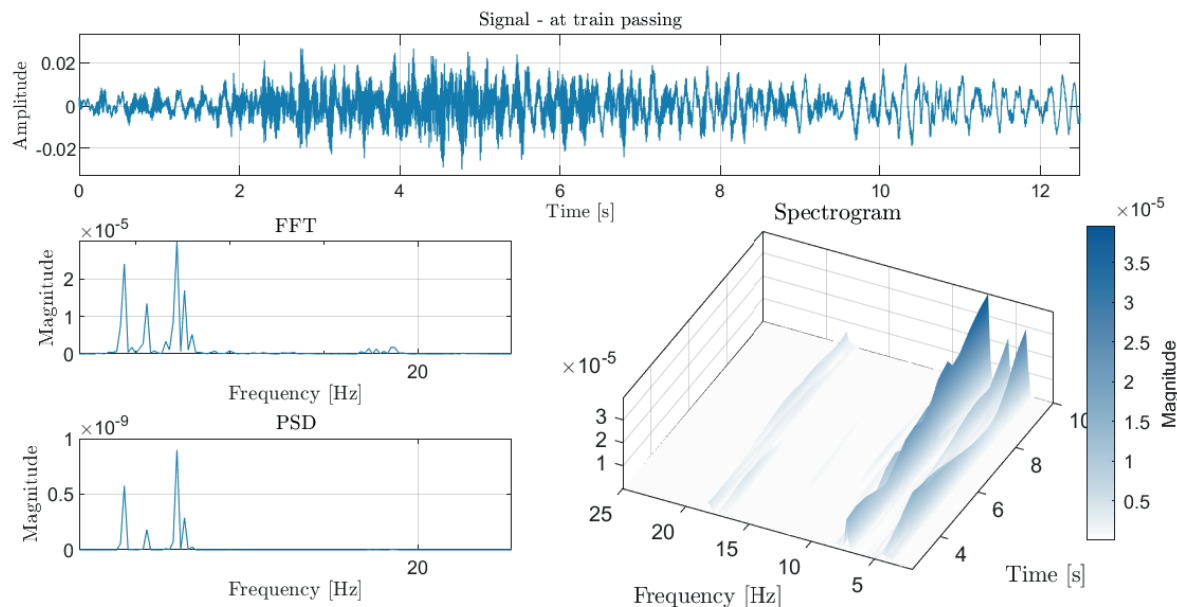
Fig. 6.16. Analysis of a sub-record within the train passing in the parallel direction X using signal processing methods: FFT analysis (left top), PSD analysis (left bottom), and STFT analysis (right).
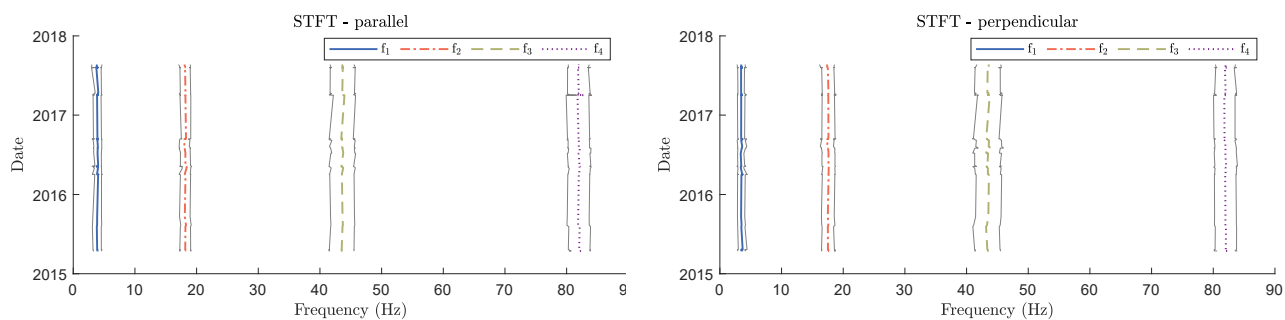
Fig. 6.17. Development of natural frequencies over time, for the first four modes calculated using signal processing methods: in the parallel direction X (left) and the perpendicular direction Z (right).
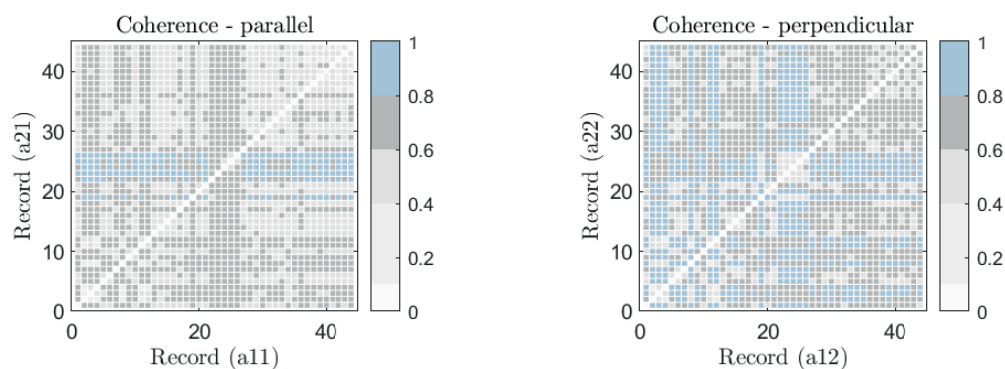
Fig. 6.18. Coherence values calculated using signal processing methods: in the parallel direction X for the sensors a11 and a21 (left), and the perpendicular direction Z for the sensors a12 and a22 (right).
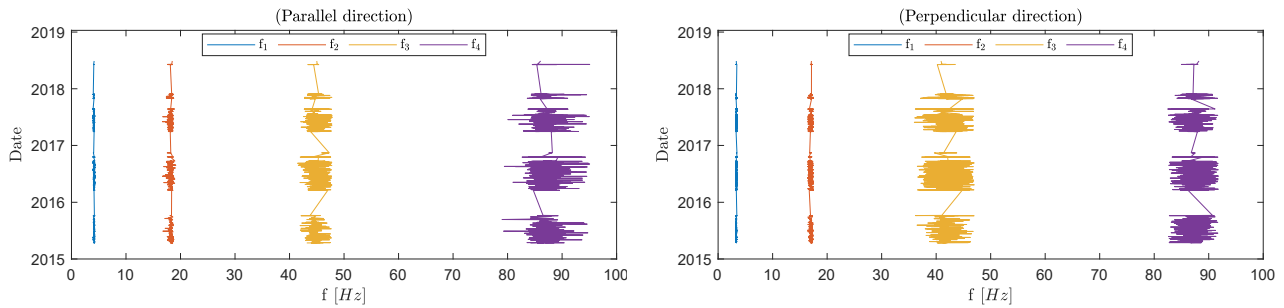
Fig. 6.19. Development of natural frequencies overtime for the first four modes calculated using the SSI method: in the parallel direction X (left), and the perpendicular direction Z (right).
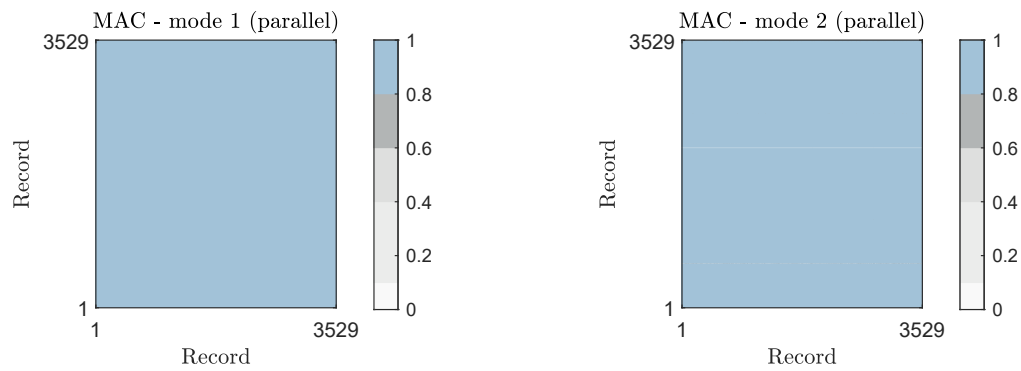
Fig. 6.20. MAC values of derived mode shapes for the first (left) and second (right) modes in the parallel direction X.
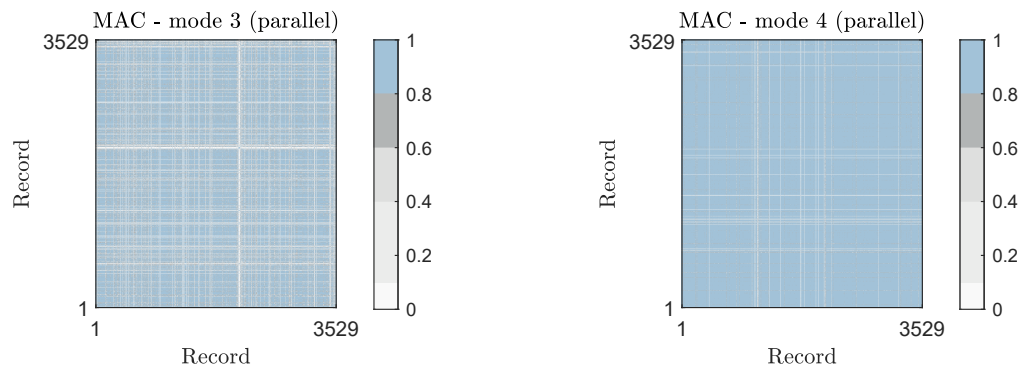
Fig. 6.21. MAC values of derived mode shapes for the third (left) and fourth (right) modes in the parallel direction X.

92
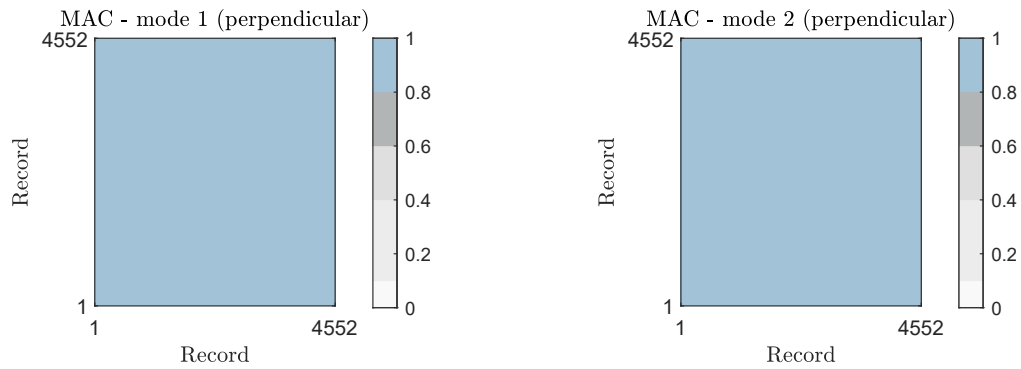
Fig. 6.22. MAC values of derived mode shapes for the first (left) and second (right) modes in the perpendicular direction Z.
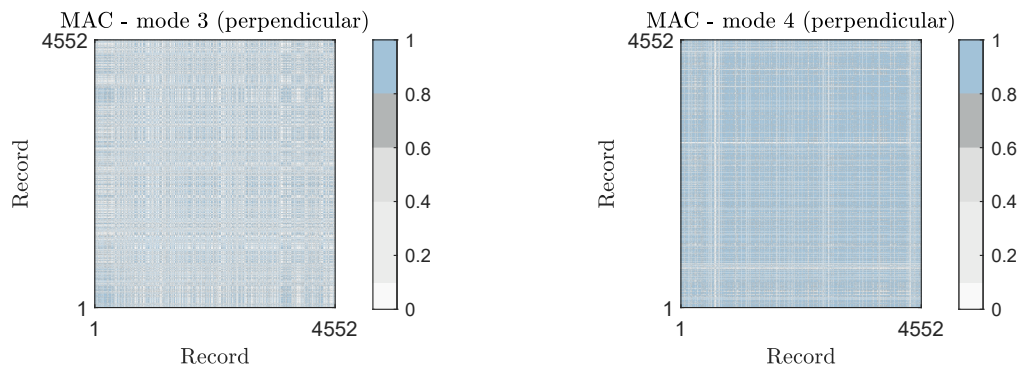
Fig. 6.23. MAC values of derived mode shapes for the third (left) and fourth (right) modes in the perpendicular direction Z.
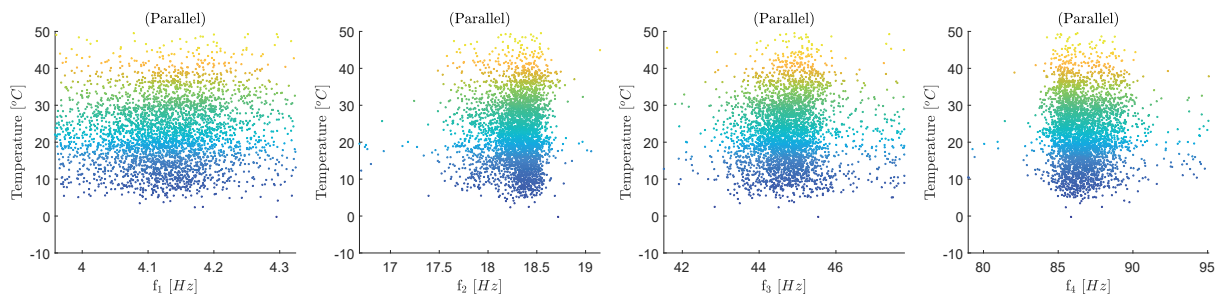
Fig. 6.24. Ambient temperature against the natural frequencies calculated using the SSI method in the parallel direction X, for the first four modes depicted from left to right, respectively.
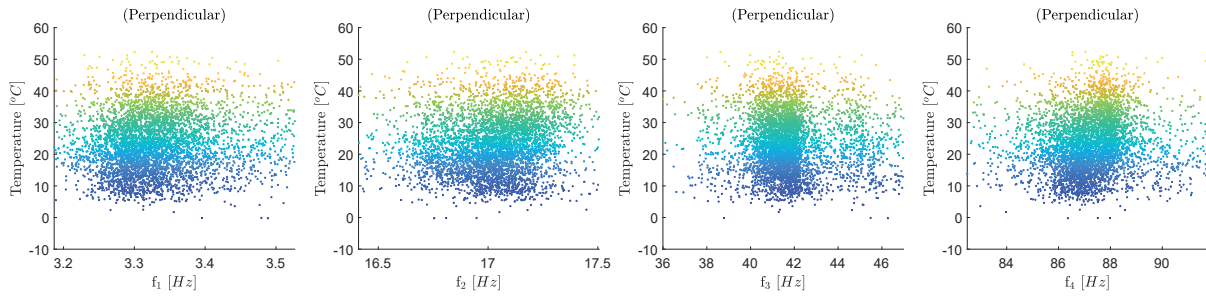
Fig. 6.25. Ambient temperature against the natural frequencies calculated using the SSI method in the perpendicular direction Z, for the first four modes depicted from left to right, respectively.
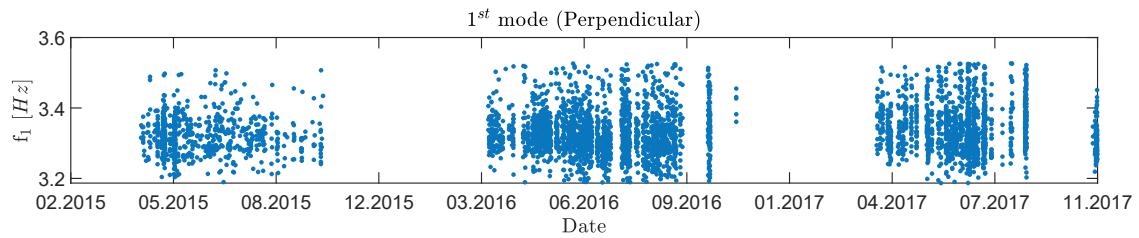
Fig. 6.26. Development of the natural frequencies overtime for the first mode, calculated using the SSI method in the perpendicular direction Z.
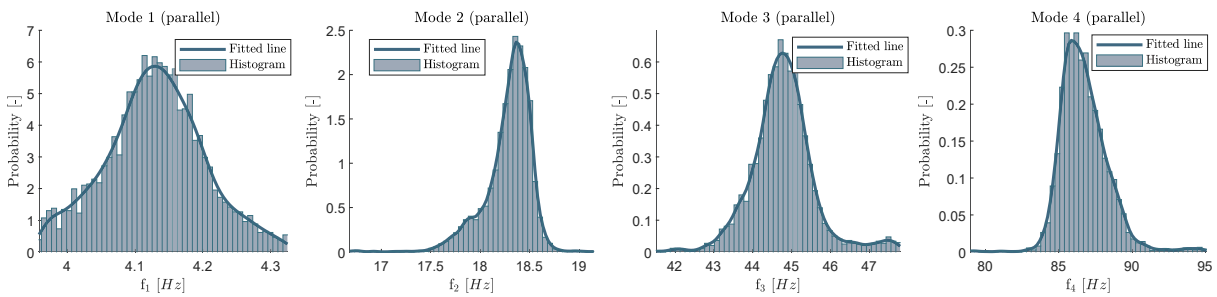
Fig. 6.27. PDF values of derived natural frequencies for the first four modes in the parallel direction X, depicted from left to right, respectively.
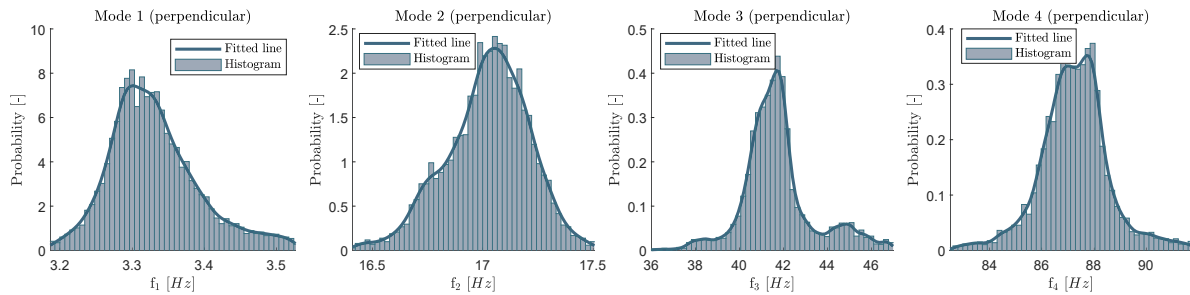
Fig. 6.28. PDF values of derived natural frequencies for the first four modes in the perpendicular direction Z, depicted from left to right, respectively.

94

6.5   Summary and Conclusion

Data recorded by the sensors of the SHM system is analyzed to build the existing status of the pole over a given time. Furthermore, system identification is made using the data recorded by the attached accelerometers. Both the signal processing and SSI techniques are used in this step. Based on the results, all indications conclude that seasonal changes are the leading cause behind the change of the dynamic characteristics of the pole in-service. For this reason, the natural frequencies of the pole fluctuate around a mean value during the specified period of monitoring. This makes the derived PDF values an excellent candidate to represent the behavior of the un-damaged poles for further checks, as in Chapter 8.

Chapter 7

Parameter Identification of the Pole

7.1 General Considerations

It is noted that each of the conducted experiments is individually imperfect for inferring the full set of unknown parameters to an acceptable quality. Moreover, the challenge arises due to the limitation of expanding the experimental program to conduct more required experiments, and the distinctive nature of the achieved measurements. This increases the complexity of the current case study and distinguishes it from other classic PI problems; however, it is an additional motivation to adapt the Bayesian approach to overcome these obstacles. The flow chart in Fig. 7.1 depicts the implementation of the proposed approach (see Section 4.1.2) to infer the unknown parameters $\boldsymbol{x}$ of the given case study using the available observations $\tilde{\boldsymbol{y}}$. To implement the proposed approach, observations of the vibration test and the 3-point bending test of the undamaged pole is used, as presented in Sections 5.3.1 and 5.3.2, respectively. This is achieved based on three tracks (T1, T2, and T3) that are shown in Table 7.1. In the tracks T1 and T2, the proposed strategies (S1 and S2, see Section 4.1.4) are applied, in parallel, using the observations of the 3-point bending test of the undamaged pole. Then, the most appropriate results of one of the applied strategies are consequently chosen. In track T3, some of identified parameters is selected as informative priors for the PI process, using the observations of the vibrations test and strategy S1.

Table 7.1: The applied tracks.

Track	Observations	Strategy	Identified parameters
T1	Bending test	S1	$\varepsilon_{PT}, f_{cm}, \varepsilon_c, f_{ctm}, E_c$
T2	Bending test	S2	$\varepsilon_{PT}, f_{cm}, \varepsilon_c, f_{ctm}, E_c$
T3	Vibration test	S1	E_c, ρ_c

For the sake of this study, the geometry parameters, the properties of the reinforcement bars, and the prestressing stands are considered as deterministic parameters $\boldsymbol{d}$. The geom-

7. PARAMETER IDENTIFICATION OF THE POLE
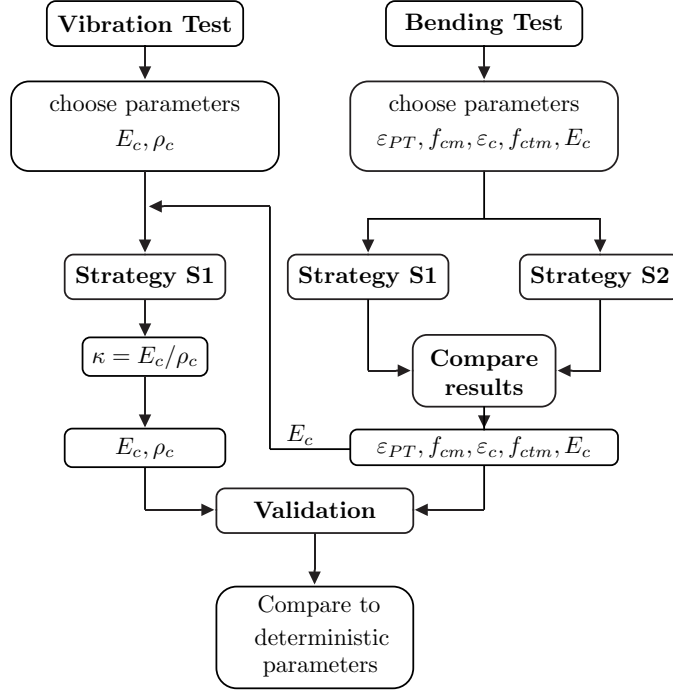
Fig. 7.1. Implementing of the proposed strategies of PI.

etry of the corresponding model $\mathcal{M}$ is built, based on the nominal values that are shown in Table 5.1. The exceptions are the thicknesses of the walls where the measured values from the laboratory are applied. The nominal properties of the prestressing and the reinforcement steel are applied as listed in Table 5.2.

From the UQ framework and the engineering point of view, the key parameters that have a significant influence on the behavior of the pole are the concrete properties and the strains of the prestressing strands. For this reason, the vector of the unknown parameters is $\boldsymbol{x} \equiv \{\varepsilon_{PT}, f_{cm}, \varepsilon_c, f_{ctm}, E_c, \rho_c\}^T$.

Except for the prestressing initial strain ε_{PT}, the prior densities of the unknown parameters $\boldsymbol{x}$ are assigned to follow PDFs of uniform distributions. This is because the prior knowledge of parameters is not enough to formulate informative priors. The priors $\pi_0(\boldsymbol{x})$ are carefully bounded, based on the available information and engineering prejudgment considering the values recommended by fib Model Code 2010 [4], that is, $\pi_0(\boldsymbol{x}) \sim \mathcal{U}(a, b)$, as listed in Table 7.2.

Based on the measurements (see Section 5.3.2), the prior distribution of ε_{PT} follows a normal distribution $\pi_0(\varepsilon_{PT}) \sim \mathcal{N}(\mu_{PT}, \sigma_{PT}^2)$ with unknown mean μ_{PT} and variance σ_{PT}^2. In this case, the literature recommends considering the conjugate priors of the hyperparameters $\boldsymbol{\theta}_x$ as the normal distribution for the unknown mean and the inverse gamma distribution

Table 7.2: The uninformative PDFs priors of the parameters.

Parameter	PDFs
Concrete compressive strength, f_{cm} [MPa]	$\mathcal{U}(80, 120)$
Concrete strain at maximum compressive stress, ε_c [‰]	$\mathcal{U}(2.5, 3.0)$
Concrete tensile strength, f_{ctm} [MPa]	$\mathcal{U}(4.0, 6.0)$
Concrete Modulus of Elasticity, E_c [GPa]	$\mathcal{U}(43, 53)$
Concrete density, ρ_c [g cm^{-3}]	$\mathcal{U}(2.1, 2.5)$

for the unknown variance [60]. Accordingly, the priors of the mean μ_{PT} and the variance σ_{PT}^2 are chosen such as $\pi_0(\mu_{PT}) \sim \mathcal{N}(3.1, 0.4)$ and $\pi_0(\sigma_{PT}^2) \sim \mathcal{IG}(5.0, 0.126)$, respectively. This corresponds with a *Maximum A Priori* $MAPr_{\sigma_{PT}^2} = 0.021$ and a standard deviation $SD_{\sigma_{PT}^2} = 0.018$. Besides, the variance of the total errors σ_{E}^2 is chosen to be a global hyperparameter θ_{E} has a uniform prior distribution $\pi_0(\sigma_{\mathrm{E}}) \sim \mathcal{U}(0.005, 0.1)$, which makes sense in this case. Moreover, due to some physical interpretations, the independency between the parameters was assumed.

7.1.1 Tracks T1 and T2 (bending test)

The proposed strategies S1 and S2 are implemented in parallel. Afterward, the results of different applied strategies are compared to detect their respective advantages. Two criteria measure the quality of the inferred parameters: the uncertainty represented by the variance of the parameters, and the shape of the posterior distribution.

The realizations of the observations $\tilde{y}_i \equiv \delta_i$ are created from the deflections δ_i of the undamaged pole. The deflection values were measured at different time steps at the specified point P1, P2, and P3 respectively, see Section 5.3.2.

Strategy S1 is applied by calculating the likelihood from Eq. (4.9) using the observation $\tilde{y}$. To apply strategy S2, the observations are divided into three subsets, based on the sensitivity indices presented in Figs. 5.15 to 5.17, that is, $K = 3$ and $\tilde{y} = \{\tilde{y}^1, \tilde{y}^2, \tilde{y}^3\}^T$. The corresponding deflection ranges of the subsets are specified in Table 7.3.

Table 7.3: The classification of the observations $\tilde{y}$ (strategy S2).

Step	Observation subset	Deflection range[1] [mm]	Sensitive parameters
1	$\tilde{y}^1$	[0 - 6]	E_c
2	$\tilde{y}^2$	(6 - 80]	$f_{ctm}, \varepsilon_{PT}$
3	$\tilde{y}^3$	(80 - 110]	f_{cm}, ε_c

[1] the deflection at mid-span (Point P1) as a reference.

In this step, the unknown parameters vector $\boldsymbol{x} \equiv \{\varepsilon_{PT}, f_{cm}, \varepsilon_c, f_{ctm}, E_c\}^T$ are inferred. It is worth mentioning that, due to the parameters independency, the posterior distribution is the product of the marginal posterior distributions, leading to consider each of them as the priors in the next step of the sequential procedure. However, the concrete density ρ_c

cannot be identified in this step because of the limitation of the conducted experiment to measure the insignificant deflection caused by the own weight of the pole, as mentioned in Section 5.3.2. Moreover, additional deterministic parameters $\boldsymbol{\xi}$ are assigned here to define the concrete constitutive model, in the corresponding numerical model, as descried Section 5.5.

At the end of the tracks T1 and T2, the unknown parameters are inferred by sampling from the posterior $\pi(\mu_{PT}, \sigma_{PT}^2, f_{cm}, \varepsilon_c, f_{ctm}, E_c, \sigma_E^2 | \boldsymbol{\delta})$. For this reason, the TMCMC algorithm is run for $N_s = 5 \cdot 10^3$ samples. Then, the statistical moments of the inferred parameters are calculated.

7.1.2 Track T3 (vibration test)

In this track, the strategy S1 is applied by using the observations vector $\tilde{\boldsymbol{y}}$ consisting of the natural frequencies that are derived in Section 5.3.1, that is, $\tilde{y}_i \equiv f_i$. Two parameters can be identified through this track corresponding to the linear behavior of the structure in the vibration test, namely, $\boldsymbol{x} \equiv \{E_c, \rho_c\}^T$.

It is known from the analytical solution of dynamic systems that $f_i \propto \sqrt{E_c/\rho_c}$. For example, given a cantilever beam has Young's modulus E, and mass density ρ. The cross section of the beam changed linearly along the its length L. The natural frequencies of the described beam is calculated [186], s follows:

$$f_i = \frac{\lambda_i^2}{2\pi L^2} \sqrt{\frac{EI_{bot}}{\rho A_{bot}}} \, , i = 1, 2, 3, \cdots , \tag{7.1}$$

where f_i is the natural frequency corresponding to the ith mode shape, λ_i is a constant; I_{bot}, A_{bot} are the moment of inertia of the cross-section and the cross-sectional area at the fixed end the cantilever, respectively.

This means that only the fixed ratio $\kappa = E_c/\rho_c$ can be identified. The values of E_c and ρ_c are unidentifiable, because any values of E_c and ρ_c that satisfy κ is valid as a solution. This phenomenon is certified in the plot of log-likelihood shown in Fig. 7.2. The flat region in the likelihood means that the observations uniquely determine the parameter values [49]. To overcome this, the posterior of E_c from track T2 is used as an informative prior in this track, as it revealed better results. This makes ρ_c identifiable and results in obtaining the posteriors of E_c and ρ_c. In this track, $5 \cdot 10^3$ samples are drawn from the posterior $\pi(E_c, \rho_c, \sigma_E^2 | \mathbf{f})$ using the TMCMC algorithm.

Fig. 7.2. 3D contours illustrate the log-likelihood of $\kappa = E_c/\rho_c$ (vibration test).

7.2 Results of Bayesian Approaches

The results of applying tracks T1 to T3 are depicted in Fig. 7.3. The solid line represents the results of the S2 strategy, whereas the dashed line shows the results of implementation of the S1 strategy. The proposed sensitivity-based strategy adds significant improvements to the quality of the inferred parameters leading to more accurate posteriors with smaller variances [142].

This is because the S2 strategy is built in a step-wise manner. In each step, it focuses only inferring highly sensitive parameters, which leads to an increase in the quality of inferred parameters. Moreover, the obtained posteriors of these sensitive parameters are used in the following step as a formative prior, which also leads to an improvement in the quality of the other parameters. On the contrary, in S1 strategy, the sensitivity of the parameters is averaged on the full set of data, which results in losing some information that is embedded in the available observations. This results in inferring parameters at a lower quality. This emphasizes that uncertainty and sensitivity are associated, as mentioned in Section 4.1.4.2.

However, the mean values of unknown parameters are inferred by both strategies with good agreement. A summary of the statistical properties of parameters is listed in Tables 7.4 and 7.5. It is clear, how much these values differ from the nominal properties that are provided in the datasheet of the structure. The inferred parameters are 20% higher than the nominal values, (see Section 5.2.2). This shows the importance of the PI process as an essential step before evaluating the behavior of the structure.

Correlations of different pairs of parameters are verified by the scatter plots of the samples. Fig. 7.4 shows the high negative correlation of parameters ε_{PT} and f_{ctm} in the model of the 3-point bending test. These two parameters are correlated with a linear
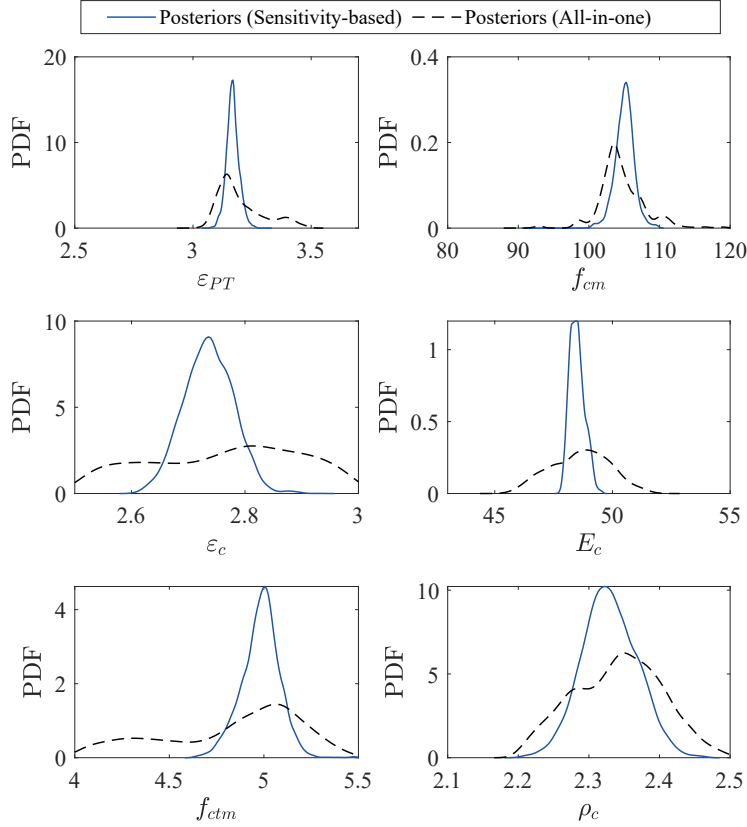
Fig. 7.3. Comparing the results of the applied Bayesian approaches: the *sensitivity-based* approach and the *All-in-one* approach.

Table 7.4: The properties of the posteriors of the identified parameters using the Bayesian strategy S1: the Maximum A Posteriori MAP, the mean value μ, and the standard deviation SD.

Parameter	ε_{PT} [‰]	f_{cm} [MPa]	ε_c [‰]	E_c [MPa]	f_{ctm} [GPa]	ρ_c [g cm^{-3}]
MAP	3.16	103.11	2.87	48.29	5.01	2.32
μ	3.20	104.63	2.76	48.63	4.83	2.34
SD	0.10	3.20	0.13	1.25	0.36	0.06

Table 7.5: The properties of the posteriors of the identified parameters using the Bayesian strategy S2: the Maximum A Posteriori MAP, the mean value μ, and the standard deviation SD.

Parameter	ε_{PT} [‰]	f_{cm} [MPa]	ε_c [‰]	E_c [MPa]	f_{ctm} [GPa]	ρ_c [g cm^{-3}]
MAP	3.16	105.36	2.73	48.06	5.11	2.32
μ	3.17	105.10	2.74	48.49	4.98	2.33
SD	0.03	1.36	0.04	0.32	0.11	0.04

Pearson coefficient of correlation $\rho_{\varepsilon_{PT},f_{ctm}} = -0.87$. From an engineering point of view, this is correct, as the higher the applied prestressing strain ε_{PT}, the lower is the required tensile strength of the concrete f_{ctm} to have the same cracking moment of the given cross section.

According to the results of track T3, the parameters E_c and ρ_c are highly correlated with a correlation coefficient of $\rho_{E_c,\rho_c} = 0.9$, as shown in Fig. 7.5. This result is expected,
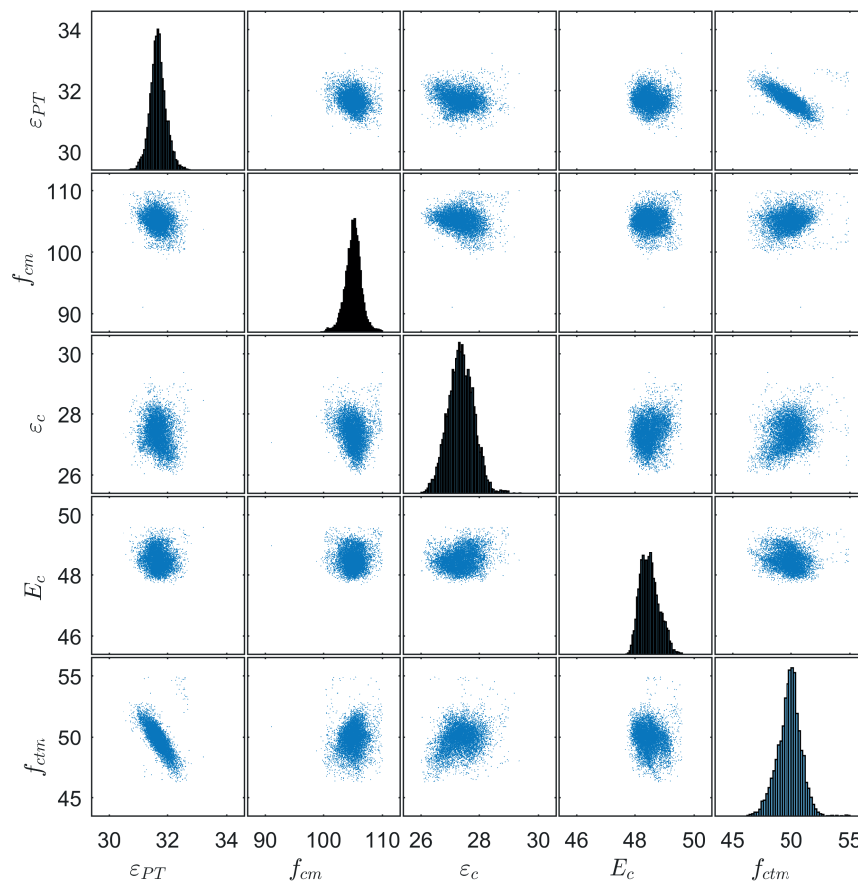
Fig. 7.4. The correlations of the identified parameters - tracks T1 and T2 (3-point bending test).

and discussed in Sections 5.3.1 and 7.1.2. However, it supports the findings of this work.
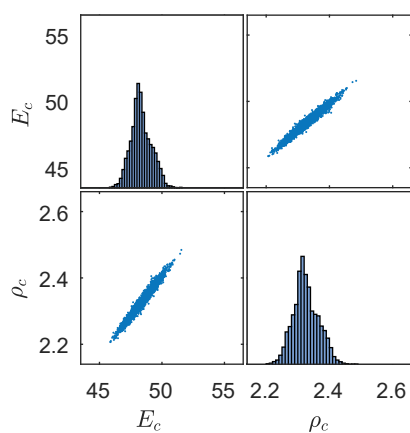
Fig. 7.5. The correlations of the identified parameters - track T3 (vibration test).

In addition, the listed hyperparameters in Table 7.6 are sampled from the posterior. The inferred MAP values of the σ_E that evaluate the total errors $\boldsymbol{\eta}$ are 0.034 and 0.041 for the observations of bending and vibration tests, respectively, which are reasonable for the types of experiments implemented, and the numerical models. Besides, the inferred values of the μ_{PT} and σ_{PT}^2 match the measured values in the laboratory to an acceptable extent, see Section 5.3.2.

Table 7.6: The properties of posteriors of the hyperparameters: the Maximum A Posteriori MAP, the mean value μ, and the standard deviation SD.

Hyperparameter	σ_E [-] [a]	σ_E [-] [b]	μ_{PT} [‰] [b]	σ_{PT}^2 [-] [b]
MAP	0.041	0.034	2.72	0.015
μ	0.040	0.029	2.86	0.023
SD	0.0067	0.0037	0.18	0.007

[a,b] Using the observations of the vibration and bending tests, respectively.

7.3 Results of the Deterministic Approach

For the identification of the parameters $\boldsymbol{x} = \{\varepsilon_{PT}, f_{cm}, \varepsilon_c, E_c, f_{ctm}, \rho_c\}^T$ of the given structure, the deterministic approach described in Section 2.5.2 is implemented. The inferred parameters are assumed to follow normal distributions. The parameters are estimated at 95% confidence level, that is, $\alpha = 0.05$. The results of this approach are summarized in Table 7.7.

Fig. 7.6 represents a comparison between the results of the applied approaches. A perfect match can be recognized for the mean values of the identified parameters, except for the mean values of the concrete density ρ_c and the tensile strength f_{ctm}, where a small bias of 3% and 2%, respectively, appeared. However, the variances of identified parameters differ considerably and show no specific trend, but in most cases the variances in Bayesian approach have higher values [55].

It is expected to have such a difference between the results of the deterministic and Bayesian approaches. This is because the Markov estimator is based on the concept of deterministic parameter identification. It may get stuck into the local minima of the cost function, mainly in the case of noisy data or unidentifiable parameters. This causes the bias of the mean values compared to Bayesian results. Besides, the Markov estimator evaluates

Table 7.7: Summary of the identified parameters using Markov estimator: the mean value μ, and the standard deviation SD.

Parameter	ε_{PT} [‰]	f_{cm} [MPa]	ε_c [‰]	E_c [MPa]	f_{ctm} [GPa]	ρ_c [g cm^{-3}]
μ	3.16	105.08	2.70	48.19	5.07	2.27
SD [%]	2.82	1.19	0.60	3.05	0.25	2.04
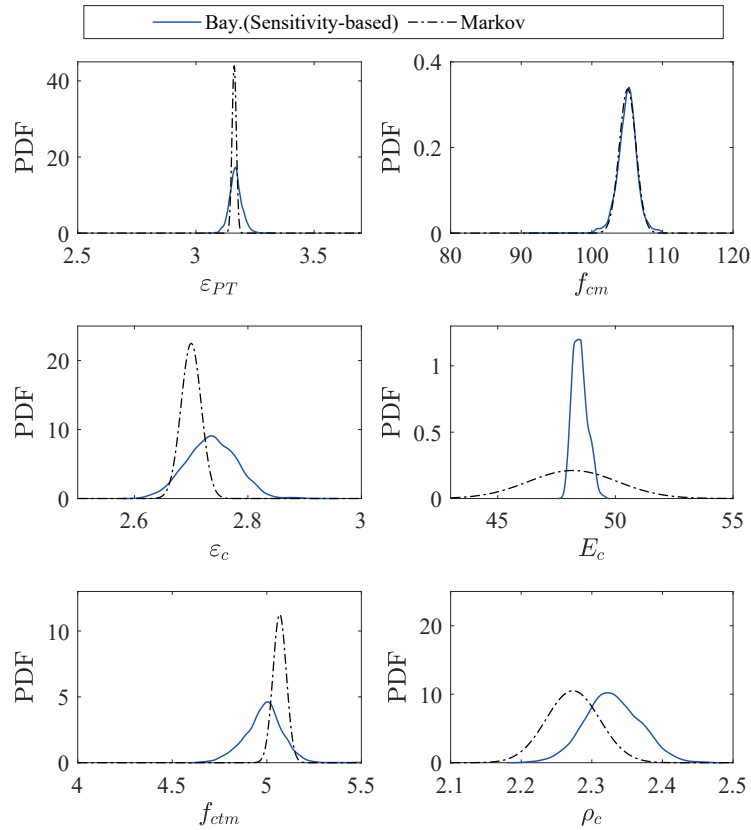
Fig. 7.6. Comparing the identified parameters of the *'sensitivity-based'* Bayesian approach and the *'Markov estimator'* deterministic approach.

the uncertainty of the parameters based on the local sensitivity at the optimized solution. This leads to considerable deviations of the variance values between the two approaches.

Considering the complexity and computational efforts, the Markov estimator can be implemented mainly for the mean values and, to some extent, as an indicator of uncertainty of the parameters. The results of the Markov estimator match the results of the Bayesian approach to an acceptable tolerance, which makes the Markov estimator a fast and straightforward tool to provide an approximation of the solution. The Bayesian approach, in comparison, requires more efforts; however, it can precisely draw the probability distributions of the identified parameters revealing some important characteristics of its distributional behavior. Besides, the Bayesian approach provides a good overview of the correlation between parameters, which leads to a better understanding of the studied problem [52].

7.4 Validation of the Results

To validate the identified parameters, the mean values of the identified parameters from strategy S2 are used as input of the FEM models. However, the results of the FEM are compared with the corresponding observations.

In the case of the bending test, the results of the FEM model are plotted against the hysteresis loops of the force-deflection derived from the measurements of the bending test. Fig. 7.7 depicts the agreement between the experimental measurements of the bending test at points P1, P2, and P3, together with the outputs of the FEM model.
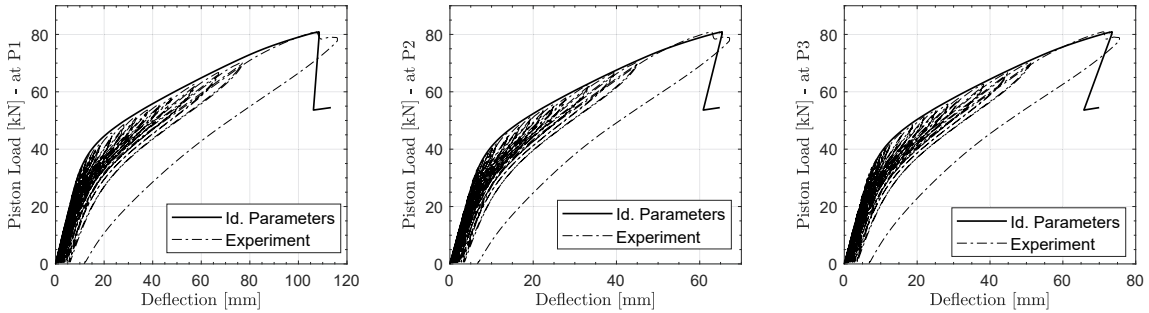
Fig. 7.7. Validation of the results using mean values of the identified parameters and the bending test model. The deflections are presented at the points P1 (left), P2 (middle), and P3 (right).

Table 7.8: Validation of the results - vibration test.

Mode shape [a]	1 - v	2 - v	3 - v	4 - v	5 - v	1 - h	2 - h	3 - h	4 - h	5 - h
$\mathbf{f}$ [Hz][b]	15.54	42.09	81.16	131.76	192.83	15.37	41.65	80.35	130.48	191.04
Difference [%][c]	0.13	1.36	0.69	0.05	0.21	1.22	1.23	0.92	0.84	0.85

[a] $(i - \mathrm{v})$ is the ith mode shape in vertical directions, and $(i - \mathrm{h})$ is the ith mode shape in horizontal directions, $i = 1, \cdots, 5$.

[b] The Natural frequencies $\mathbf{f}$ are calculated using the mean values of the identified parameters through the *'sensitivity-based'* Bayesian approach.

[c] The difference is calculated in comparison to the measured values of the natural frequencies that are listed in Table 5.3.

In the same manner, the first five natural frequencies in the horizontal and vertical direction (according to the test setup) are derived from the FEM model using the inferred parameters. The results are listed in Table 7.8. The trivial differences show that the results of the FEM model conform (with high accuracy) with the experimental observations of the vibration test.

Finally, a comparison is done between the inferred parameters, and the conventional values of the concrete properties that are specified by the different engineering standards. Accordingly, the equations of the Fib Model Code 2010 [4], which specifies the concrete properties based on the compressive strength of the concrete f_{cm}, are utilized. Thus, the

MAP values of the f_{cm} from Table 7.5 are used. The calculated properties show that the inferred parameters are in line with the recommended values of the given code with relatively acceptable tolerance, as shown by the differences in Table 7.9.

Table 7.9: The concrete properties based on the recommendation the Fib code [4] and the MAP of the $f_{cm} = 105.36$ MPa.

Parameter	f_{cm} [MPa]	ε_c [‰]	E_c [MPa]	f_{ctm} [GPa]
value	105.36	2.90	47.10	5.18
Difference [%][a]	—	6.20	3.10	1.40

[a] The differences are measured to the MAP values in Table 7.5.

7.5   Summary and Conclusion

The Bayesian probabilistic approach is applied to identify the unknown parameters of the given structure. First, the all-in-one strategy (S1) is implemented, where six parameters are inferred by utilizing the FEM model and observations of the multiple experiments.

The sensitivity-based strategy (S2) is implemented by dividing the observations into subsets based on the sensitivity of the parameters. Then, the Bayesian approach is applied in a sequential manner, considering the posterior of the current step as the prior to the subsequent step.

In both strategies, the TMCMC algorithm is used to sample from the posterior. The results showed a considerable improvement in the quality of the inferred parameters and confirmed the associations between the uncertainty and the sensitivity of the parameters. Furthermore, considering the unknown total errors as hyperparameters allowed to evaluate the total errors of the whole PI process.

The deterministic UQ framework is also implemented, where the concept of the Markov estimator is used to evaluate the uncertainty of the parameters. The results show that both frameworks matched each other with acceptable tolerance. However, the differences in results are normal because, unlike the Bayesian approach, the Markov estimator is based on the local sensitivity of parameters. Thus, the Bayesian approach is more accurate for evaluating the uncertainty of the unknown parameters despite requiring more computational effort.

In the validation step, a perfect agreement is achieved when using the mean values of the inferred parameters as inputs for the numerical model to compare results to the experimental observations. Additionally, it is proved that the inferred properties of the concrete are in line with the recommended values of the Fib Model Code 2010 for the same compressive strength.

The considerable deviation between the inferred parameters and the nominal ones draws

attention to the importance of the PI process before conducting any study on the existing structures. This emphasizes the argument at the beginning of this chapter and laid the foundations for more appropriate implementation of the subsequent phases of this study.

Chapter 8

Status Monitoring of Poles

8.1 Introduction

As verified in Chapter 6, the changes detected in natural frequencies were mainly due to seasonal, repeated, and transient actions. In other words, no damage was detected on the poles monitored by the SHM systems. To implement the proposed monitoring approach, mentioned in the Section 4.2, the behavior of the damaged poles is studied using the FEM model in Section 8.2. The natural frequencies and mode shapes of the damaged pole are compared with the healthy data of the pole obtained in Chapter 6 using the SM algorithm described in Section 4.2.2. Then, the damage identification algorithms described in Section 4.2.3 are implemented. As a result, the possible damage can be localized and quantified.

8.2 Simulation of Damaged Pole

The results in Chapter 5 show that the monitored poles are completely healthy and do not yet have any damage. In the absence of any further data of damaged poles in service, the behavior of the damaged pole is verified using FEM models. To simulate the long-term degradation of concrete over the life-time of the structure (global change), the analysis of the FEM model is completed using different values for the concrete modulus of elasticity E_c in the range of $E_c = [15-55]$ GPa, with an increment of 3 GPa. For each global value of E_c, local damages are repeated at heights $\boldsymbol{\vartheta}_a = \{0.6, 1.0, 1.50, 2.0, 2.5, 3.0, 3.5, 4.0, 5.0, 6.0, 7.0, 8.0\}^T \times 10^3$ mm, measured from the bottom of the pole. At each local damage point $\boldsymbol{\vartheta}_a$, five damage severity ratios $\boldsymbol{\alpha} = \{0, 0.25, 0.50, 0.75, 0.95\}^T$ are used. For a better interpretation of the results, the damage locations $\boldsymbol{\vartheta}_a$ are normalized in the range of $[0-1]$, such that the normalized dimensionless damage locations are $\boldsymbol{\vartheta} = \{0.01, 0.05, 0.11, 0.17, 0.21, 0.26, 0.32, 0.37, 0.47, 0.58, 0.68, 0.79\}^T$.

Fig. 8.1. Effects of changing E_c on natural frequencies **f** (global change): relative changes in **f** to the case of $E_c = 48$ GPa (left), MAC values of the first four modes for the pair of $E_c = 15$ and 55 GPa (middle), COMAC values at ten equally-spaced coordination along the pole for the pair of $E_c = 15$ and 55 GPa (right).

The severity ratio of damage α_i is defined as the depth of the damaged area to the diameter of the cross-section at the damage location ϑ_i in the considered direction. Two main directions are considered: parallel and perpendicular to the train track, that is, X, and Z respectively. The damage is simulated by reducing E_c at the damage location (local change), which is equivalent to a reduction in stiffness of the pole.

The changes in natural frequencies **f** due to global changes of E_c are calculated relative to the case of $E_c = 48$ GPa, as shown in Fig. 8.1 (left). As expected, natural frequencies are reduced by decreasing the value of global E_c with the same ratios for all mode shapes. To verify the changes of mode shapes, MAC and COMAC values for each pair of E_c values are checked. It is noted that the mode shapes of different models are fully correlated regardless of the value of E_c. As shown in Fig. 8.1 (middle) and (right), the example presents the values of MAC and COMAC values for the pair of $E_c = 15$ and 55 GPa. Consequently, using relative changes in natural frequencies is more suitable for detecting global changes rather than using the values of MAC and COMAC.

In Fig. 8.2, the surfaces describe relative changes in natural frequencies of the first four modes due to local damage with different values of damage severity $\boldsymbol{\alpha}$, and normalized damage location $\boldsymbol{\vartheta}$. The relative natural frequency $\Delta\mathbf{f}$ is defined, as follows:

$$\Delta\mathbf{f}_i = \frac{|\mathbf{f}_i^d - \mathbf{f}_i^u|}{\mathbf{f}_i^u},\tag{8.1}$$

where $\mathbf{f}_i^d$ and $\Delta\mathbf{f}_i^u$ represent the natural frequencies of the ith mode of the damaged and un-damaged pole, respectively.

The shape of each of the surfaces in Fig. 8.2 matches the shape of the corresponding mode shape [187]. It is known that the mode shape is not sensitive to damage when the damage

Fig. 8.2. Relative changes of natural frequencies $\Delta\mathbf{f}$ for the $[1^{st} - 4^{th}]$ modes, calculated for different values of damage severity $\boldsymbol{\alpha}$, and normalized damage location $\boldsymbol{\vartheta}$.

is located near the nodes of the mode shape. Similarly, this means that some surfaces are more pertinent to detecting damage at a specific location than others. However, merging the informative data from multiple surfaces provides an excellent candidate for building a damage detection algorithm that can detect the location and severity of damage along the pole.

8.3 Implementing the Status Monitoring Algorithm

To implement the SM algorithm described in Section 4.2.2, changes in natural frequencies are artificially generated using the statistical properties mentioned in Section 6.4 and the features of both the global and local changes mentioned in Section 8.2. Data for the first five years are considered for defining the reference status; that is, the un-damaged properties of the pole (see the probability distributions of the natural frequencies derived in Chapter 6). Data is generated for 5 years (commencing in 2015) with a sampling frequency of one measurement per hour. To simulate the expected future status of the poles, three damage

Fig. 8.3. Damage indices DIs of Scenario 1 using the natural frequencies $[f_1 - f_4]$: for damage severity $\alpha = 20\%$ (left), and for damage severity $\alpha = 30\%$ (right).

scenarios cover the expected damage cases use of the pole, as follows:

1. **Scenario 1 (sudden damage status)**: represents the case of local damage due to sudden damage propagation over a short period, that is, 1 month. The damage starts after 15 years. Four damage severity ratios $\alpha = \{0.2, 0.3, 0.4, 0.5\}^T$ are tested. The damage location is chosen at the bottom of the pole, such that $\vartheta = 0.05$. An example of the scenario is the loss of the prestressing forces due to failure of the bond between the concrete and strands.

2. **Scenario 2 (slow damage status)**: describes the case of local damage due to slow damage propagation that starts after 15 years and increases linearly over a long period (15 years). The maximum damage severity is considered as $\alpha = 0.95$. This scenario represents the increase of damage width over time, for example, due to creep or fatigue.

3. **Scenario 3 (global change status)**: simulates the status of an un-damaged pole with global changes over a given period (see Fig. 8.1), such as global changes due to material degradation over time, or changes in boundary conditions. The maximum change of mean values of the natural frequencies are considered as 5%.

To implement the proposed scenarios, the generated time history of the natural frequencies of the first four modes $[f_1 - f_4]$ are utilized. The damage indices of the proposed scenarios are calculated using a sliding window with a length of $w_{len} = 2$ years, and a window shift of $w_{sh} = 2$ months. Based on the reference status, the threshold is considered as 0.63, which corresponds to ACL $= 3\sigma_\lambda$ of the data.

The damage indices resulting from sudden damage status (Scenario 1) for different damage severity α are depicted in Figs. 8.3 and 8.4. As expected, damage severity has a signif-
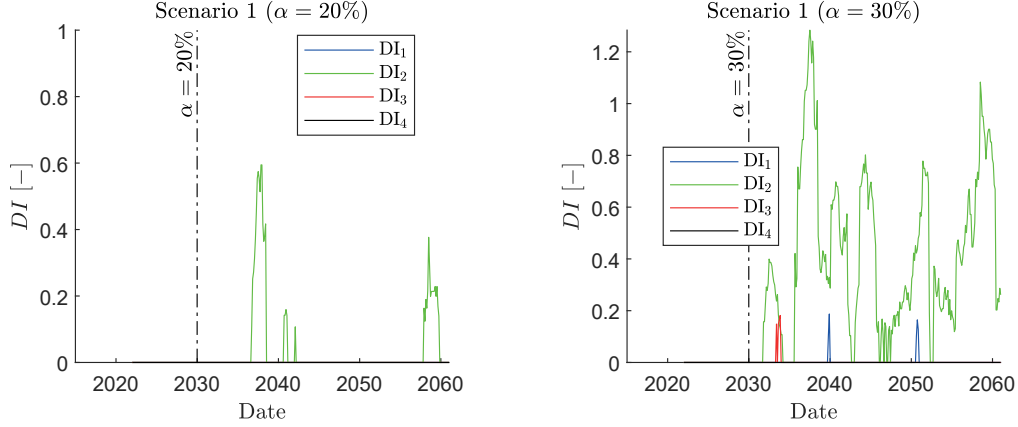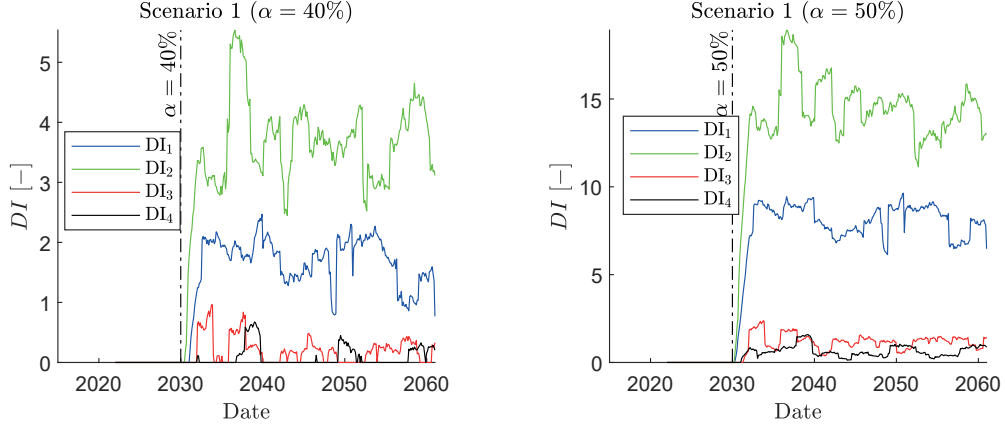
Fig. 8.4. Damage indices DIs of Scenario 1 using the natural frequencies $[f_1 - f_4]$: for damage severity $\alpha = 40\%$ (left), and for damage severity $\alpha = 50\%$ (right).
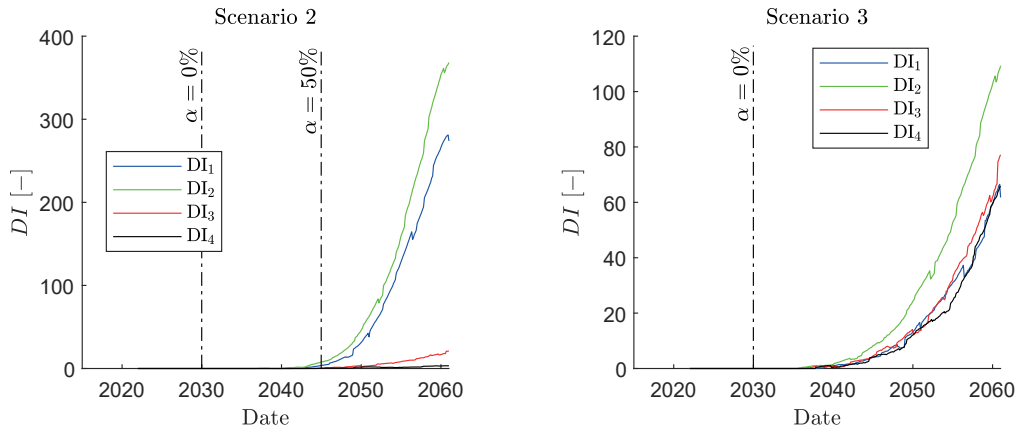
Fig. 8.5. Damage indices DIs using natural frequencies $[f_1 - f_4]$: Scenario 2 (left), and Scenario 3 (right).

icant influence on the calculated damage indices. Starting from damage severity $\alpha = 20\%$ in Fig. 8.3 (left), the damage is detected after a considerable period of crack propagation. The damage is detected by mode 2, which is the dominant mode (in this case) according to the damage location (see, for example, Fig. 8.2 for the effect of damage location ϑ and damage severity α on the relative change of the natural frequencies). For the damage severity $\alpha = 30\%$ shown in Fig. 8.3 (right), modes 1 and 3 start to be sensitive to damage. In Fig. 8.4, the damage is obviously detected on time for the damage severity $\alpha = 40\%$ and $\alpha = 50\%$. It should be noted that the relative differences between the DI_1 to DI_4 increase significantly by increasing the damage severity α.

The damage indices resulting from global changes (Scenario 3) are shown in Fig. 8.5 (right). Compared with Scenario 2, it is evident that the relative differences between DI_1 to

DI_4 are not clear. The indices DI_1 to DI_4 change simultaneously and follow the same trend as changes for natural frequencies shown in Fig. 8.1. Moreover, despite the maximum relative change in natural frequencies at the end of the considered time in both Scenarios 2 and 3 being approximately 5%, the damage indices of the dominant modes for the sudden damage scenario (Scenario 2) are three times greater than the corresponding ones for the global changes scenario (Scenario 3). Having these indicators, the damage indices for Scenario 3 can be distinguished easily from those of Scenarios 1 and 2.

In the case of slow damage status (Scenario 2), where the damage propagates gradually over long time, the damage indices are similar to those of Scenario 1. As shown in Fig. 8.5 (left), the damage is detected precisely when the damage severity reaches $\alpha = 40\%$. The relative differences between DI_1 to DI_4 are also evident, and increase dramatically by increasing the damage severity.

Consequently, besides detecting the damage, the relative sensitivity of the modes to damage can be considered a good indicator for distinguishing the scenarios of sudden local damage (Scenarios 1 and 2) from the global changes scenario (Scenario 3). Moreover, this emphasizes the importance of considering all available data from different sources using data fusion techniques to detect the damage.

As a conclusion, the damage indices are suitable for detecting the damage caused by the proposed scenarios starting from a damage severity $\alpha = 35\%$, whereas the pole shows low sensitivity to damage severity below this value for all modes, as shown Fig. 8.1. In addition, the relatively small change in relative natural frequencies due to damage severity below the $\alpha = 30\%$ is located within the variance of the identified natural frequencies listed in Table 6.1. It should be noted that small cracks are not considered severe for this type of pole because of the role of prestressing forces in closing the cracks as notified in literature (for example, [13]). As mentioned in Section 5.3.3, this phenomenon was also noticed after conducting the 3-point bending experiment (see Section 5.3.1).

8.4 Implementing Damage Identification Algorithms

In the absence of any data on the damaged poles in service, artificial measurements are generated using the FEM simulation mentioned in Section 8.2. The locations of the sensors are chosen to be equally distributed along the pole using distances of $d_{sn}^a = \{500, 1000, 1500, 2000, 2500\}^T$ mm, corresponding to normalized dimensionless distances of $d_{sn} = \{0.05, 0.11, 0.16, 0.21, 0.26\}^T$. The artificial measurements are created using combinations of damage location ϑ, damage severity α (see, Section 8.2), and distances between sensors. The artificial modal curvatures and natural frequencies are perturbed using Gaussian noise with coefficients of variation of $0, 1, 3, 5$, and 8% in addition to a bias of 1% of the no-noise values. In total,

Fig. 8.6. Damage localization of damaged pole using curvature algorithm: in the vertical direction (left), and in the horizontal direction (right), according to the experimental setup

1500 records of artificial measurements are generated and utilized for implementing the proposed damage identification algorithms. Both the CDI and FDI algorithms are applied using the first four mode shapes and natural frequencies. For easy interpretation of results, normalized dimensionless damage location in the range $[0 - 1]$ is used [144].

8.4.1 Validation of the Curvature-based Damage Identification Algorithm

The CDI algorithm is validated using measurements from the tested damaged pole mentioned in Section 5.3.3. The modal curvatures of the first five modes of both damaged and undamaged pole are utilized. These results coincide with the results shown in Figs. 5.25 and 5.26. In addition, Fig. 8.6 (left) shows that the damage is localized to reasonable accuracy in the vertical direction (the direction of main cracks), keeping in mind that the cracks are spread along the pole mainly in the middle part of the pole (see Fig. 5.18). As discussed in Section 5.3.3, and shown in Fig. 8.6 (right), the results of horizontal direction are less able to localize the damage; however, they still provide some useful information.

The efficiency of the CDI algorithm is based on the number of sensors, distances between sensors, and the accuracy of calculated modal curvatures. Therefore, it is noted that the damage is localized accurately when the damage is close to one of the sensors. However, the CDI algorithm provides an informative prior that could be used in conjunction with other damage detection algorithms to localize the damage precisely; for example, using the normalized fitted lines in Fig. 8.6 as an informative prior.
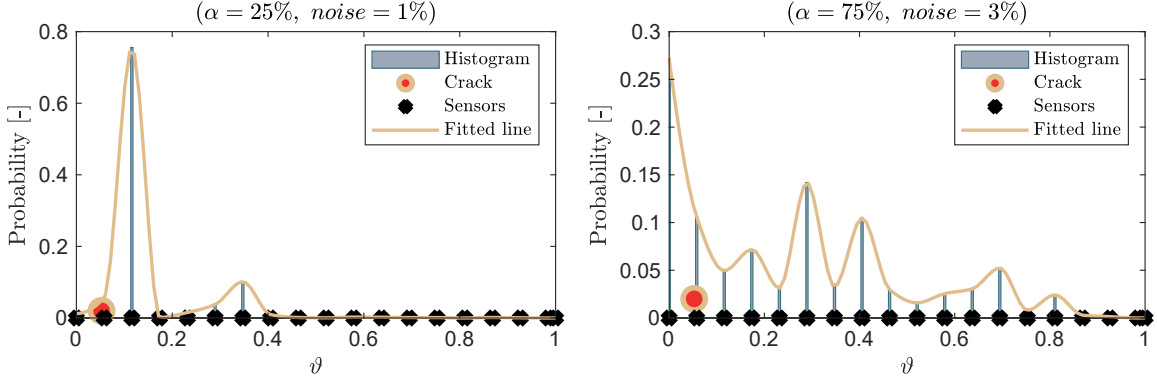
Fig. 8.7. Localizing the damage $\hat{\vartheta}$ using the curvature algorithm: for $\vartheta = 0.05$, $\alpha = 25\%$, $noise = 1\%$, and $d_{sn} = 0.05$ (left); for $\vartheta = 0.05$, $\alpha = 75\%$, $noise = 3\%$, and $d_{sn} = 0.05$ (right).
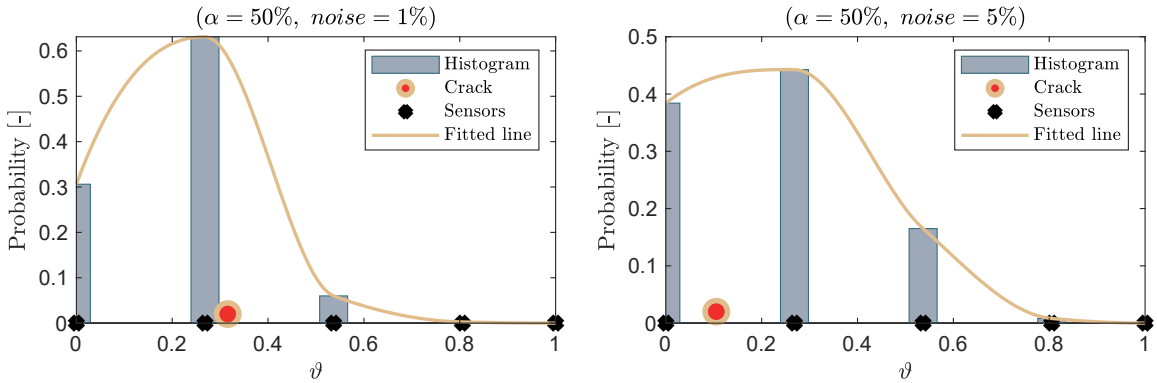
Fig. 8.8. Localizing the damage $\hat{\vartheta}$ using the curvature algorithm: for $\vartheta = 0.32$, $\alpha = 50\%$, $noise = 1\%$, and $d_{sn} = 0.26$ (left); for $\vartheta = 0.11$, $\alpha = 50\%$, $noise = 5\%$, and $d_{sn} = 0.26$ (right).

8.4.2 Implementing the Curvature-based Damage Identification Algorithm

By implementing the CDI algorithm, it is noted that its accuracy is sensitive to damage severity α, noise level, and distance between damage location and adjacent sensor. Examples of implementing this algorithm using artificial measurements in the direction perpendicular to the train track Z are shown in Figs. 8.7 and 8.8. The histograms and fitted lines present the probability of the damage location along the pole. The algorithm provides a higher probability to the points around the damage location, which makes it a good prior for localizing the damage. However, it is evident that for distances between sensors of $d_{sn} = [2000-2500]$ mm, more informative priors are achieved (even with high noise level) compared with the cases of smaller distances between sensors [144].

8.4.3 Implementing the Frequency-based Damage Identification Algorithm

As a new signal is recorded by the SHM system, the natural frequencies of the structure can be evaluated using signal processing, or SSI methods, as mentioned in Sections 6.3 and 6.4. Consequently, the FDI algorithm is implemented using the artificial measurements. The CDI algorithm is used to build informative priors to damage locations $\pi_0(\vartheta)$. Uninformative priors of damage severity α are used, such that $\pi_0(\alpha) \sim \mathcal{U}(0.0, 1.0)$. The posteriors are derived by implementing the TMCMC algorithm for 1000 samples [144].
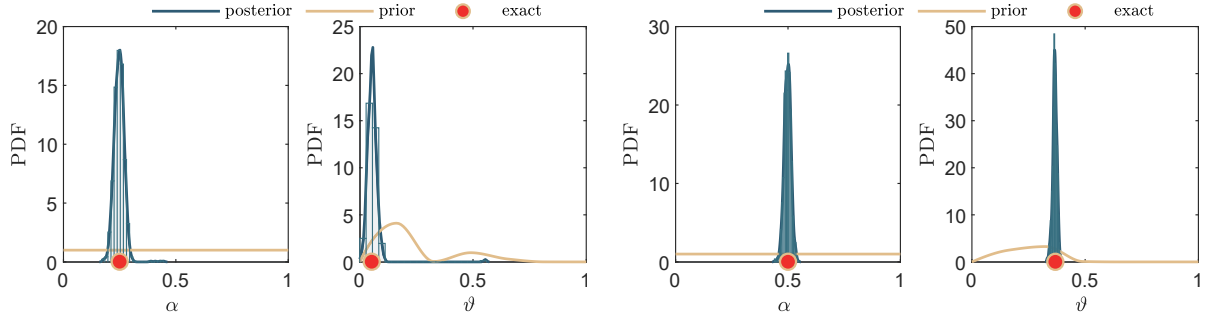
Fig. 8.9. Identified damage severity $\hat{\alpha}$, and damage location $\hat{\vartheta}$, using frequency-based algorithm for ($noise = 1\%$): $\vartheta = 0.05$, and $\alpha = 25\%$ (left); $\vartheta = 0.37$, and $\alpha = 50\%$ (right).
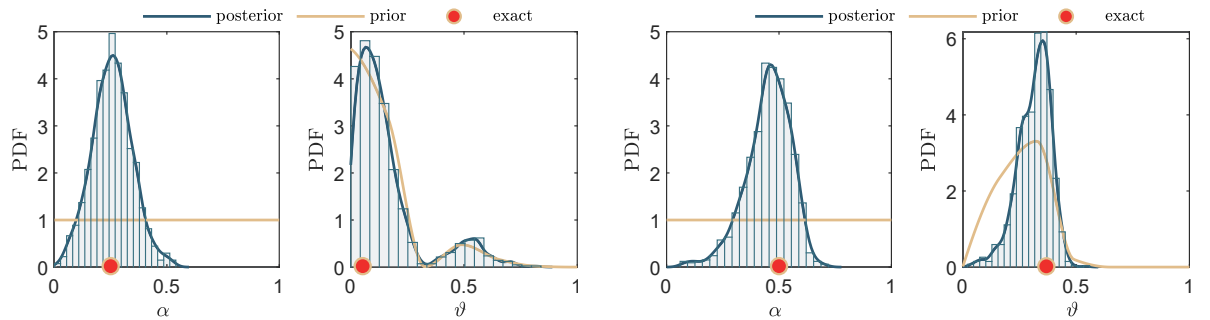
Fig. 8.10. Identified damage severity $\hat{\alpha}$, and damage location $\hat{\vartheta}$, using frequency-based algorithm for ($noise = 5\%$): $\vartheta = 0.05$, and $\alpha = 25\%$ (left); $\vartheta = 0.37$, and $\alpha = 50\%$ (right).

Examples of the results of the FDI algorithm are depicted in Figs. 8.9 and 8.10, for noise levels of 1 and 5%, respectively. The posteriors of the identified location $\hat{\vartheta}$ and the identified severity $\hat{\alpha}$ are shown for selected damages at different locations and severities. The FDI algorithm identifies the damage characteristics to an acceptable accuracy. The noise level significantly affects the variances of the identified damage parameters.

To evaluate the efficiency of the FDI, the Re-constructed Errors (ReErr) are calculated using 1500 records of artificial measurements. The ReErr is defined as the absolute difference

Fig. 8.11. Reconstructed error (ReErr) of the identified damage location $\hat{\vartheta}$ using frequency-based algorithm: the MAP values $\hat{\vartheta}^{MAP}$ (left), the standard deviation $\sigma_{\hat{\vartheta}}$ (right).

Fig. 8.12. Box-plot of reconstructed error (ReErr) of the identified damage location $\hat{\vartheta}$, classified based on noise level: the MAP values $\hat{\vartheta}^{MAP}$ (left), the standard deviation $\sigma_{\hat{\vartheta}}$ (right).

between the artificial damage and MAP values of the identified damage characteristics; that is, $(\hat{\alpha}^{MAP}, \hat{\vartheta}^{MAP})$. The precision of the results is measured by standard deviations of the posteriors; that is, $(\sigma_{\hat{\alpha}}, \sigma_{\hat{\vartheta}})$.

The *ReErr* and their σ are shown in Figs. 8.11 and 8.15 for *ReErr* of $\hat{\vartheta}^{MAP}$ and $\hat{\alpha}^{MAP}$, respectively. For a better interpretation of the results, standard box-plots are used to evaluate the statistical properties of the *ReErr* at each pair of noise levels and damage severity α. For greater clarity, the box-plots are classified based on noise level, α, and d_s, as shown in Figs. 8.12 to 8.14, and Figs. 8.16 to 8.18 for the *ReErr* of $\hat{\vartheta}^{MAP}$, and $\hat{\alpha}^{MAP}$, respectively.

As shown in Fig. 8.11 (left), the *ReErr* of identified damage location $\hat{\vartheta}^{MAP}$ increases by increasing the noise level, and decreases by increasing damage severity α, which is expected. It is evident that the efficiency of the FDI algorithm increases dramatically starting from

Fig. 8.13. Box-plot of reconstructed error (ReErr) of the identified damage location $\hat{\vartheta}$, classified based on damage severity: the MAP values $\hat{\vartheta}^{MAP}$ (left), the standard deviation $\sigma_{\hat{\vartheta}}$ (right).

damage severity $\alpha = 0.5$. Then, it continues with good accuracy up to noise level of 0.05. The standard deviations of the identified damage location $\sigma_{\hat{\vartheta}}$, shown in Fig. 8.11 (right), follows the same trend; however, these are more affected by the noise levels even for the cases of high damage severity, for example, $\alpha = 0.95$.

The box-plots in Fig. 8.12 provide a more accurate representation of the effect of the noise level on the $ReErr$ of $\hat{\vartheta}^{MAP}$. The maximum values of $ReErr$ reach reasonable limits even for a high level of noise; that is, 0.1 for the noise level of 0.08 with a maximum standard deviation of 0.24. In contrast, the $ReErr$ in Fig. 8.13 reaches a maximum value of 0.17 at low damage severity $\alpha = 0.25$, and decreases dramatically for damage severity up to 75%. The same is concluded for the corresponding standard deviations, which touch the maximum value of 0.23 at damage severity $\alpha = 0.25$. The results in Fig. 8.14 fluctuate around converged values with a simple preference for the cases of $d_s = 0.26$ considering the values of the $ReErr$ of $\hat{\vartheta}^{MAP}$ and their $\sigma_{\hat{\vartheta}}$. However, outliers can be seen in the box-plots that count less than 0.35% of the verified data, according to the definition of standard box-plots. Then, they have no significant effects on the efficiency of the current results.

The $ReErr$ of identified damage severity $\hat{\alpha}^{MAP}$ shown in Fig. 8.15 follows the same trend, as in the case of $\hat{\vartheta}^{MAP}$. It is noted from Fig. 8.15 (right) that the standard deviations $\sigma_{\hat{\alpha}}$ are less scattered compared with similar cases of $\sigma_{\hat{\vartheta}}$. Unlike the $\hat{\vartheta}^{MAP}$, the $ReErr$ of identified damage severity $\hat{\alpha}^{MAP}$ is more sensitive to the level of noise than the damage severity. It reaches a maximum value of 0.21 at a noise level of 0.08 (see Fig. 8.16), in comparison with 0.12 at a damage severity of 0.25, as shown in Fig. 8.17. The effects of d_s on the $ReErr$ of identified damage severity $\hat{\alpha}^{MAP}$ are similar to those of the $ReErr$ of identified damage severity $\hat{\vartheta}^{MAP}$ described previously, as shown in Fig. 8.18.

In conclusion, the FDI algorithm is able to identify the location $\hat{\vartheta}$ and the severity $\hat{\alpha}$
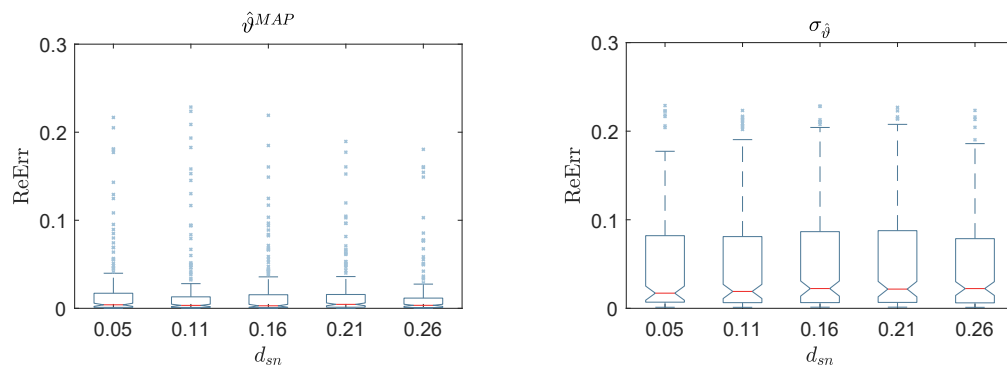
Fig. 8.14. Box-plot of reconstructed error (ReErr) of the identified damage location $\hat{\vartheta}$, classified based on the distances between sensors d_{sn}: the MAP values $\hat{\vartheta}^{MAP}$ (left), the standard deviation $\sigma_{\hat{\vartheta}}$ (right).
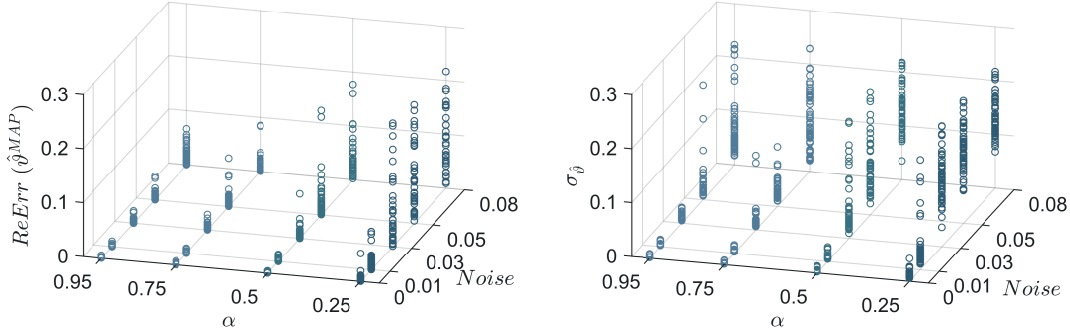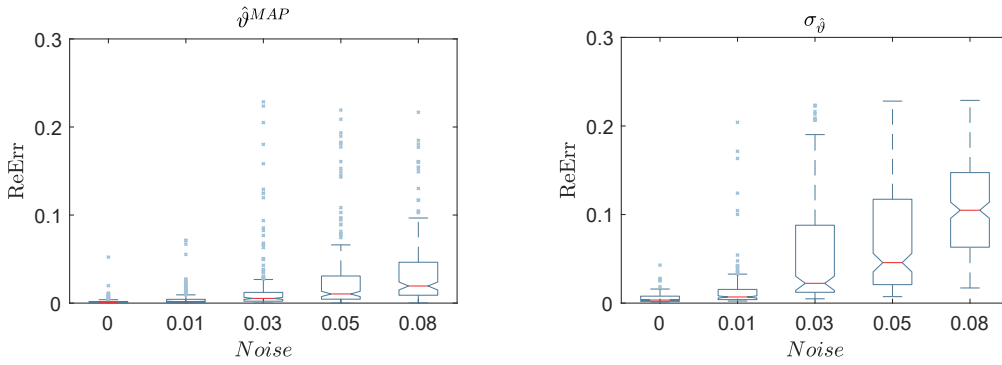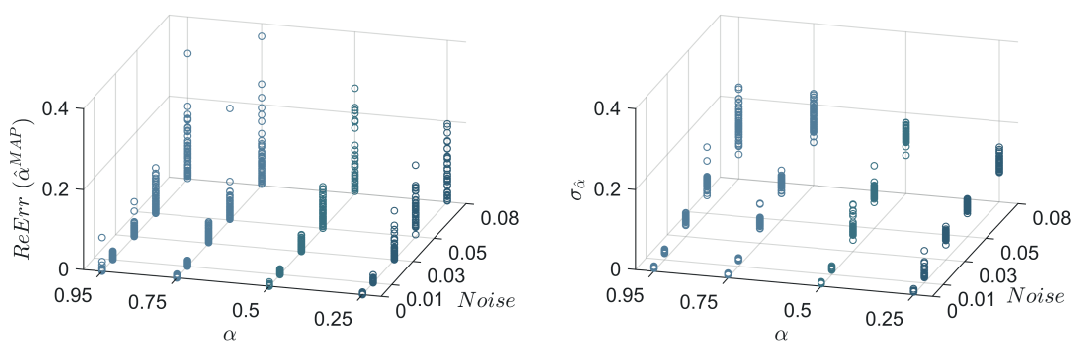

Fig. 8.15. Reconstructed error (ReErr) of the identified damage severity $\hat{\alpha}$ using frequency-based algorithm: the MAP values $\hat{\alpha}^{MAP}$ (left), the standard deviation $\sigma_{\hat{\alpha}}$ (right).
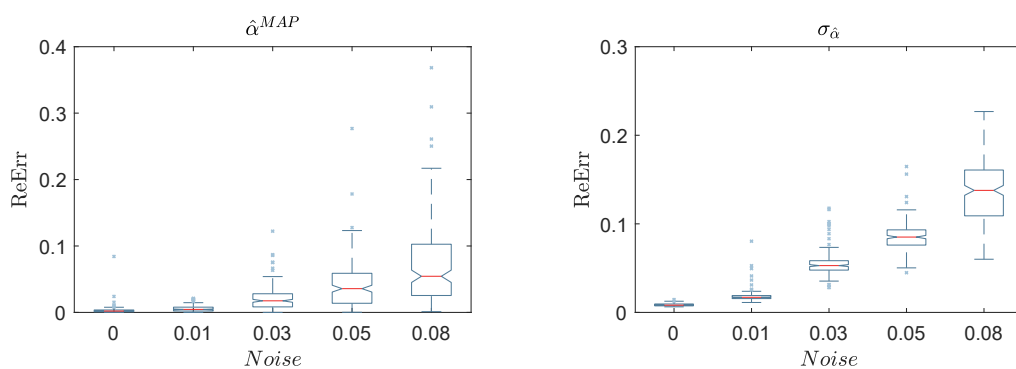
Fig. 8.16. Box-plot of reconstructed error (ReErr) of the identified damage location $\hat{\alpha}$, classified based on noise level: the MAP values $\hat{\alpha}^{MAP}$ (left), the standard deviation $\sigma_{\hat{\alpha}}$ (right).
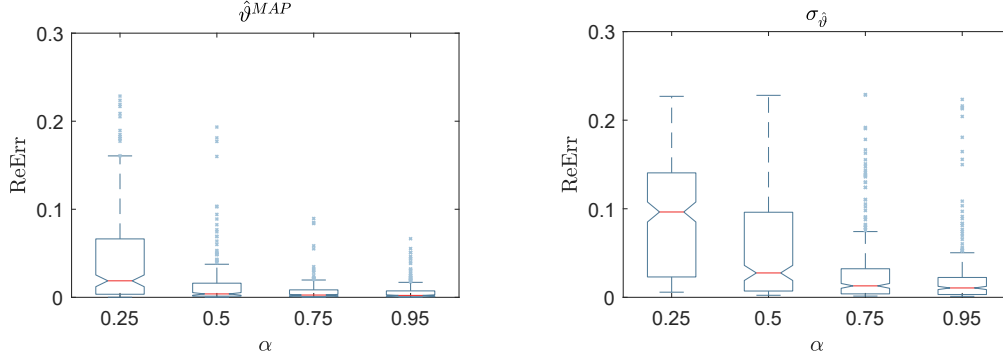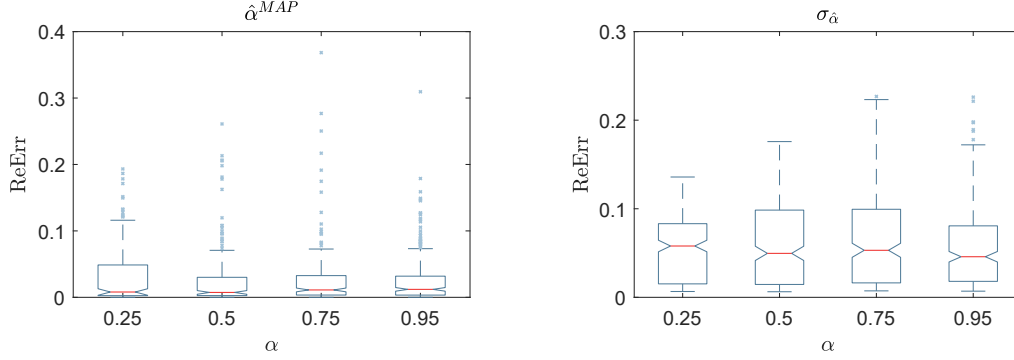
Fig. 8.17. Box-plot of reconstructed error (ReErr) of the identified damage location $\hat{\alpha}$, classified based on damage severity: the MAP values $\hat{\alpha}^{MAP}$ (left), the standard deviation $\sigma_{\hat{\alpha}}$ (right).
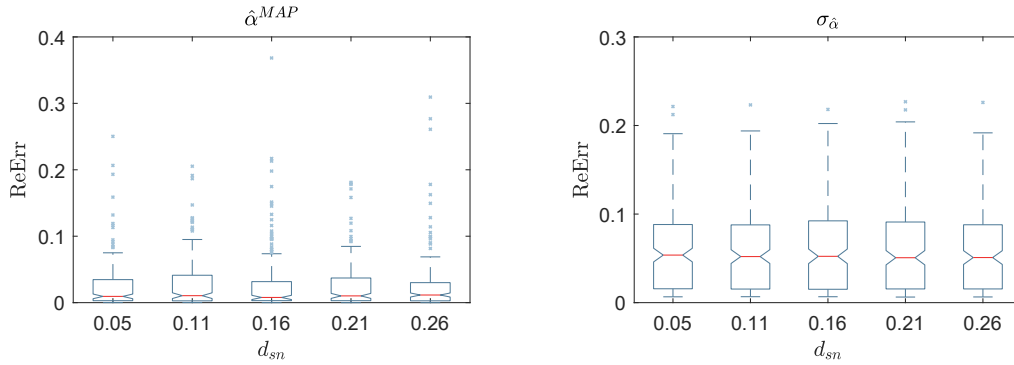
Fig. 8.18. Box-plot of reconstructed error (ReErr) of the identified damage location $\hat{\alpha}$, classified based on the distances between sensors d_{sn}: the MAP values $\hat{\alpha}^{MAP}$ (left), the standard deviation $\sigma_{\hat{\alpha}}$ (right).

of the damage to an acceptable maximum error $ReErr$ of 0.12 at a noise level of 0.05. It should be kept in mind that the maximum values of the standard box-plots correspond to a probability of 0.35% at the tails of the probability distribution of data. This means that $\hat{\vartheta}$ is localized within a maximum error of $1150\,\mathrm{mm}$, and $\hat{\alpha}$ is quantified with a maximum offset of 0.12 from real damage severity.

8.5 Summary and Conclusion

In this chapter, the vibration-based status monitoring approach proposed in Section 4.2 is implemented. The SM algorithm, the CDI algorithm, and the FDI algorithm are validated and tested using the database recorded by the SHM system, the identified parameters of the pole, and the results of SI. The proposed monitoring algorithm uses a logistic function for classifying the status of the pole as either damaged, or un-damaged status. The algorithm is

able to detect the damaged case for the damage severity efficiently above 30%. The proposed CDI algorithm offers a higher probability to the points around the damage location, which makes it a suitable prior for localizing the damage, even with a high noise level. The FDI algorithm is applied using the artificial measurements derived from the finite element models of the damaged poles. This algorithm is able to identify the location and the severity of the damage efficiently in form of probability distributions, which quantifies the uncertainty of the results. The algorithm identifies the damage to a maximum error of 0.12 at a high noise level of 5%.

Consequently, the proposed approach and algorithms included here achieve the aim of this research in creating a mechanism to trace the status of the poles and provide an alarm when damage occurs. Moreover, it is possible to determine the location and severity of damage efficiently with acceptable accuracy even in cases of high noise levels. The proposed approach is characterized by ease, and rapid application, because the required inputs can be derived using simple signal processing or even using SSI techniques for more informative data. In addition, this approach is built based on the natural frequencies of the poles, which can be retrieved using a fewer number of accelerometers in comparison with other available approaches described in the literature. Furthermore, this approach utilizes the benefit of data fusion in merging the informative data from multiple sources and methods to increase the quality and accuracy of the expected results. Further, the proposed approach is introduced in a stochastic UQ framework represented in the Bayesian inference, which quantifies the uncertainty of results caused by different sources of data and methods that are used in applying this approach.

Part III

Conclusions and Outlook

Chapter 9

Conclusions

9.1 Summary and Conclusion

The use of electrified transportation is increasing, particularly with global efforts to mitigate greenhouse gas emissions that contribute to climate change and global warming. Questions regarding the integrity of catenary poles (which carry the catenary system along the routes of electrified transportation systems) still exist. Prestressed, spun-cast concrete poles are good alternatives to the classic poles made from wood and steel, because they are cheaper, have a longer operational life, and lower lifetime costs, making them more feasible.

This study contributes to verifying the characteristics of catenary poles that support the electrification system along high-speed train tracks. Using a stochastic UQ framework, the work utilizes the concept of data fusion for the optimal use of data derived from multiple sources to verify the behavior of given poles. Mainly, three sources of data were used: measurements of experiments conducted on full-scale poles, detailed numerical models, and data recorded using the SHM system over a period of four years.

In this research, a vibration-based status monitoring approach that traces the status of the pole over time was presented. This approach consisted of three algorithms: the SM, the CDI, and the FDI. The proposed approach was characterized by ease and rapid application, because the required inputs could be derived using simple signal processing, or even using SSI techniques for more informative data. In addition, this approach was developed based on the natural frequencies of the poles, which could be retrieved using fewer accelerometers in comparison with other available approaches discussed in the literature. The approach utilized the benefit of data fusion in merging the informative data from multiple sources and methods to increase the quality and accuracy of the expected results. Further, the proposed approach was introduced in a stochastic UQ framework, represented in the Bayesian inference, which quantifies the uncertainty of results caused by different sources

of data and methods that are used in applying this approach. Consequently, the proposed approach and the algorithms included here achieved the aim of this research in creating a mechanism to trace the status of the poles and provide an alarm when damage occurs. Moreover, this approach identified the location and severity of damage with acceptable accuracy, even in cases of high levels of noise.

The existing status of the poles was retrieved by analyzing the data recorded by the SHM system installed on selected poles on-site. SI was made using signal processing and SSI techniques. As a result, it is indicated that seasonal changes are the leading cause of changing dynamic characteristics of the pole. Therefore, PDF values were built to describe the fluctuation of the natural frequencies of the pole around a mean value during the specified period of monitoring. Besides describing the behavior of the poles, these outcomes were utilized to develop the status monitoring approach and the numerical simulation of the damaged pole.

In the framework of the experimental program, three experiments were conducted on a full-scale pole, as follows: the vibration test of the un-damaged pole, the 3-point bending test, and the vibration test of the damaged pole. The measurements of the 3-point vibration test and the vibration test of the un-damaged pole were analyzed and prepared to be used in the PI process. The vibration test of the damaged pole verified the behavior of the pole in a damaged case. The analysis of corresponding measurements provided useful information to be used in developing the status monitoring approach. Furthermore, the details of the numerical modeling techniques and the material constitutive models used in this study were outlined. The numerical models were essential for PI and the simulation of the damaged pole.

In the PI process, the Bayesian probabilistic approach was applied to identify the unknown parameters of the given structure. First, the empirical Bayesian approach was implemented through an all-in-one strategy (S1), where six parameters were inferred by utilizing the FEM model and observations of the multiple experiments. To improve the quality of inferred parameters, an adapted sequential Bayesian approach was proposed. This approach was implemented through the sensitivity-based strategy (S2) by dividing the observations into subsets based on the sensitivity of the parameters. Then, the Bayesian approach was applied sequentially by considering the posterior of the current step as a priori to the subsequent step. In both strategies, the TMCMC algorithm was used to sample from the posterior. The results demonstrated considerable improvement in the quality of the inferred parameters and confirmed the associations between the uncertainty and the sensitivity of the parameters. Furthermore, considering the unknown total errors as hyperparameters resulted in evaluating the total errors of the whole PI process. In the validation step, perfect

agreement was achieved when using the mean values of the inferred parameters as inputs for the numerical model to compare results to the experimental observations. In addition, it was proven that the inferred properties of the concrete are in line with the recommended values of Fib Model Code 2010 for the same compressive strength. The considerable deviation between the inferred and nominal parameters draws attention to the importance of the PI process before conducting any study on existing structures. This emphasized the argument at the beginning of this chapter and laid the foundations for more appropriate implementation of the subsequent phases of the study.

9.2 Future Works

Applying the proposed SM algorithm looks very promising when applied together with the algorithms included here to other types of cantilever structures, such as the poles support the power transmission lines, antenna masts, chimneys, and wind turbines. Moreover, this approach can be developed to be valid for monitoring bridges. Furthermore, more efforts are required to use the concept of data fusion for the optimal use of methods and data derived from multiple sources in enhancing the outcomes of the PI and SHM. Bayesian inference is the correct approach in this instance, despite its heavy computations. Different data can be utilized, and at the same time, the uncertainty of different parameters can be considered.

A further improvement is needed to integrate the concept of parameter sensitivity in the PI process, mainly when time-dependent measurements are utilized. It is proposed to integrate the sensitivity analysis within the sampling algorithm (such as TMCMC in the Bayesian approach) for further automation of the PI process.

It should be emphasized that it is necessary to apply DoE procedures before installing any SHM system [188]. Efforts should be paid to define the goals behind installing SHM systems, the expected outputs, and how much these findings are useful for the monitoring process of the given structure later. It is recommended that pre-analysis of the structure of interest (for example, using FEM) is conducted as a part of the DoE procedures. This preliminary analysis is essential for exploring the behavior of the given structure, defining sensitive parameters, and afterward designing an appropriate SHM system, such as types, locations, and number of the sensors.

As a perspective for monitoring catenary poles used for electric train systems, the author suggests using fiber optic sensors (namely, Fiber Bragg Gratings (FBGs)) that can be embedded in the concrete during the production of poles. The main benefit of FBG is that it can be used as multi-sensors for measuring several physical parameters in the same fiber at different locations along the pole; for example, strain and temperature [92, 85]. Besides, FBGs are insensitive to external perturbations and electromagnetic interference [108]. To

simplify data collection, each pole is provided with a Radio-frequency Identification (RFID) sensor that stores the data temporally [189]. The stored data is wireless-transferred periodically from the RFIDs to specific trains passing nearby the pole [190]. Then, the data is collected from trains and stored in a database. Finally, the proposed monitoring algorithms in this study can be implemented to verify the status of poles under monitoring.

References

[1] B. H. Thacker, S. W. Doebling, F. M. Hemez, M. C. Anderson, J. E. Pepin, E. A. Rodriguez, Concepts of model verification and validation, Tech. rep., Los Alamos National Lab. (2004). xi, 10, 11

[2] D. He, Q. Gao, W. Zhong, A numerical method based on the parametric variational principle for simulating the dynamic behavior of the pantograph-catenary system, Shock and Vibration 2018. xi, 56, 57

[3] Europoles GmbH & Co. KG, Catenary poles: Carrier systems for urban mass transit and mainline rail traffic, [Accessed 01 March 2019].
URL https://www.europoles.com/en/products/catenary-poles.html xi, 2, 56, 58

[4] Fib, Model Code for Concrete Structures 2010, International Federation for Structural Concrete (Fib), 2013. doi:10.1002/9783433604090. xix, 76, 98, 106, 107

[5] G. Hill, O. Heidrich, F. Creutzig, P. Blythe, The role of electric vehicles in near-term mitigation pathways and achieving the uk's carbon budget, Applied Energy 251 (2019) 113111. 1

[6] F. T. Princiotta, Global climate change and the mitigation challenge, in: Global Climate Change-The Technology Challenge, Springer, 2011, pp. 1–50. 1

[7] CER, EU Strategy for long-term greenhouse gas emissions reductions - The crucial role of rail, electronically, Bruxelles, Belgium (November 2018). 1

[8] Directorate-General for Mobility and Transport (European Commission), EU TRANSPORT in figures – Statistical pocketbook 2019, EU publications, Publications Office of the European Union, Luxembourg, 2019. doi:10.2832/729667. 1

[9] Siemens AG, eHighway - Elektrifizierter Straßengüterverkehr, electronically, München, Germany (2017). doi:www.siemens.com/mobility/eHighway. 1

REFERENCES

[10] K. Rießberger, U. Gerber, R. Linsel, K. Meißner, H. Rahn, E. Lay, E. Jänsch, T. Mölter, J. Pachl, A. Heppe, et al., Handbuch Eisenbahninfrastruktur, 3rd Edition, Springer-Verlag, 2019. 1, 78

[11] F. Kiessling, R. Puschmann, A. Schmieder, E. Schneider, Contact lines for electric railways: planning, design, implementation, maintenance, 3rd Edition, John Wiley & Sons, 2018. 1, 78

[12] J. Rodgers, E. Thomas, Prestressed concrete poles: State-of-the-art, PCI Journal 29 (5) (1984) 52–103. 1, 55

[13] A. Fam, Development of a novel pole using spun-cast concrete inside glass-fiber-reinforced polymer tubes, PCI journal 53 (3) (2008) 100–113. 1, 2, 55, 114

[14] W. J. Oliphant, D. C. Sherman, Prestressed Concrete Transmission Pole Structures, American Society of Civil Engineers, 2012. `doi:10.1061/9780784412114`. 1, 55

[15] BFT International, High-performance precast concrete elements for overhead transmission poles, Bauverlag Issue 05/2019.
URL `https://www.bft-international.com/en/artikel/bft_High-performance_precast_concrete_elements_for_overhead_transmission_poles_3356947.html` 2

[16] J. Remitz, M. Wichert, M. Empelmann, Ultra-high performance spun concrete poles–part I: Load-bearing behaviour, Proceedings of HPC/CIC 2017 (Paper no. 54). 2, 56

[17] R. M. Measures, Structural Monitoring with Fibre Optic Technology, 1st Edition, ACADEMIC PRESS, 2001. `doi:10.1088/0957-0233/12/9/708`. 2

[18] D. C. Montgomery, Design and analysis of experiments, John wiley & sons, 2017. 2

[19] E. de Rocquigny, N. Devictor, S. Tarantola, Uncertainty in industrial practice: a guide to quantitative uncertainty management, John Wiley & Sons, 2008. 7, 10, 12

[20] P. F. Dunn, Measurement and data analysis for engineering and science, CRC press, 2014. 7, 10

[21] R. B. Ash, C. A. Doléans-Dade, Probability and measure theory, Academic Press, 2000. 7

[22] D. Bigoni, A. Engsig-Karup, Uncertainty quantification with applications to engineering problems, DTU Compute, 2014. 7, 15, 19

REFERENCES

[23] R. C. Smith, Uncertainty quantification: theory, implementation, and applications, Vol. 12, Siam, 2013. 7, 11, 22

[24] J. P. Hessling, Uncertainty Quantification and Model Calibration, Intech, 2017. 7, 8

[25] S. O. Funtowicz, J. R. Ravetz, Uncertainty and quality in science for policy, Vol. 15, Springer Science & Business Media, 1990. 7

[26] T. J. Sullivan, Introduction to Uncertainty Quantification, Vol. 63, Springer, 2015. doi:10.1007/978-3-319-23395-6. 8, 12, 16

[27] B. M. Ayyub, G. J. Klir, Uncertainty modeling and analysis in engineering and the sciences, Chapman and Hall/CRC, 2006. 8, 10, 12

[28] A. Etz, J. Vandekerckhove, Introduction to Bayesian inference for psychology, Psychonomic Bulletin & Review 25 (1) (2018) 5–34. 8, 11

[29] M. J. Bayarri, J. O. Berger, The interplay of Bayesian and frequentist analysis, Statistical Science (2004) 58–80 .doi:10.1214/088342304000000116. 8

[30] J. M. Hilbe, R. S. de Souza, E. E. O. Ishida, Bayesian Models for Astrophysical Data: Using R, JAGS, Python, and Stan, Cambridge University Press, 2017. doi:10.1017/CBO9781316459515. 9

[31] J. VanderPlas, Frequentism and Bayesianism: a python-driven primer, arXiv preprint arXiv:1411.5018. 9

[32] M. J. Bayarri, J. O. Berger, R. Paulo, J. Sacks, J. A. Cafeo, J. Cavendish, C.-H. Lin, J. Tu, A framework for validation of computer models, Technometrics 49 (2) (2007) 138–154. 11

[33] G. A. Seber, C. Wild, Nonlinear regression, Wiley-Interscience, 2003. 11, 17

[34] D. G. Krige, A Statistical Approach to Some Basic Mine Valuation Problems on the Witwatersrand, Journal of the Chemical, Metallurgical and Mining Society of South Africa 52 (6) (1951) 119–139. 11, 78

[35] S. Särkkä, Bayesian filtering and smoothing, Vol. 3, Cambridge University Press, 2013. 11, 22

[36] Y. M. Marzouk, H. N. Najm, L. A. Rahn, Stochastic Spectral Methods for Efficient Bayesian Solution of Inverse Problems, Journal of Computational Physics 224 (2) (2007) 560–586. doi:10.1016/j.jcp.2006.10.010. 11, 21

REFERENCES

[37] C. M. Bishop, Pattern Recognition and Machine Learning (Information Science and Statistics), Springer-Verlag, Berlin, Heidelberg, 2006. 11, 21

[38] J. P. Hessling, Introductory chapter: Challenges of uncertainty quantification, in: J. P. Hessling (Ed.), Uncertainty Quantification and Model Calibration, IntechOpen, Rijeka, 2017, Ch. 1. `doi:10.5772/intechopen.69517`. 12

[39] J. S. Rosenthal, A first look at rigorous probability theory, 2nd Edition, World Scientific Publishing Company, 2006. 12

[40] D. Williams, Probability with martingales, Cambridge university press, 1991. 12

[41] R. Durrett, Probability: theory and examples, Cambridge university press, 2010. 12

[42] A. Tarantola, Inverse Problem Theory and Methods for Model Parameter Estimation, Society for Industrial and Applied Mathematics, 2005. `doi:10.1137/1.9780898717921`. 14, 16

[43] R. C. Aster, B. Borchers, C. H. Thurber, Parameter Estimation and Inverse Problems, second edition Edition, Academic Press, 2013. `doi:10.1016/B978-0-12-385048-5.00030-6`. 14, 15, 23

[44] E. Simoen, C. Papadimitriou, G. Lombaert, On prediction error correlation in Bayesian model updating, Journal of Sound and Vibration 332 (18) (2013) 4136–4152. `doi:10.1016/j.jsv.2013.03.019`. 15, 31

[45] BIPM, IEC, IFCC, ILAC, ISO, IUPAC, OIML, Evaluation of measurement data - supplement 1 to the "Guide to the expression of uncertainty in measurement," Propagation of distributions using a Monte Carlo method, Bureau International des Poids et Mesures, JCGM 101. 15

[46] BIPM, IEC, IFCC, ILAC, ISO, IUPAC, OIML, Evaluation of measurement data - supplement 2 to the "Guide to the expression of uncertainty in measurement" - Extension to any number of output quantities, Bureau International des Poids et Mesures, JCGM 102. 15

[47] J. V. Beck, K. J. Arnold, Parameter Estimation in Engineering and Science, Wiley, New York, 1977. 15

[48] B. Lei, G. Xu, M. Feng, F. Van der Heijden, Y. Zou, D. de Ridder, D. M. Tax, Classification, parameter estimation and state estimation: an engineering approach using MATLAB, John Wiley & Sons, 2017. 15

REFERENCES

[49] F. Alkam, T. Lahmer, Solving non-uniqueness issues in parameter identification problems for pre-stressed concrete poles by multiple bayesian updating, in: M. Voigt, Proske (Eds.), 15th International Probabilistic Workshop & 10th Dresdner Probabilistik Workshop, TUDPress, Dresden, 2017, pp. 303–315. 15, 100

[50] P. C. Hansen, Discrete Inverse Problems: Insight and Algorithms, Vol. 7, Siam, 2010. `doi:10.1137/1.9780898718836`. 15, 16

[51] J. Idier, Bayesian Approach to Inverse Problems, John Wiley & Sons, 2013. 16, 18

[52] F. Alkam, T. Lahmer, On the quality of identified parameters of prestressed concrete catenary poles in existence of uncertainty using experimental measurements and differenterent optimization methods, in: W. Desmet, B. Pluymers, D. Moens, W. Rottiers (Eds.), 28th International Conference on Noise and Vibration Engineering, ISMA 2018 and 7th International Conference on Uncertainty in Structural Dynamics, USD 2018, KU Leuven-Departement Werktuigkunde, Leuven, Belgium, 2018, pp. 3913–3923. 16, 105

[53] H. Banks, A. Cintrón-Arias, F. Kappel, Parameter selection methods in inverse problem formulation, in: Mathematical modeling and validation in physiology, Springer, 2013, pp. 43–73. 16

[54] T. Lahmer, E. Rafajłowicz, On the optimality of harmonic excitation as input signals for the characterization of parameters in coupled piezoelectric and poroelastic problems, Mechanical Systems and Signal Processing 90 (2017) 399–418. `doi:10.1016/j.ymssp.2016.12.024`. 17

[55] F. Alkam, T. Lahmer, Quantifying the uncertainty of identified parameters of prestressed concrete poles using the experimental measurements and different optimization methods, Engineering and Applied Sciences 4 (4) (2019) 84. `doi:10.11648/j.eas.20190404.13`. 17, 104

[56] D. Calvetti, E. Somersalo, An Introduction to Bayesian Scientific Computing: Ten Lectures on Subjective Computing, Vol. 2, Springer Science & Business Media, 2007. `doi:10.1007/978-0-387-73394-4`. 18, 22

[57] C. A. L. Bailer-Jones, Practical Bayesian Inference: A Primer for Physical Scientists, Cambridge University Press, 2017. `doi:10.1017/9781108123891`. 19, 20, 21, 22

[58] J. Kaipio, E. Somersalo, Statistical and computational inverse problems, Vol. 160, Springer Science & Business Media, 2006. 19

REFERENCES

[59] J. B. Nagel, B. Sudret, A unified framework for multilevel uncertainty quantification in Bayesian inverse problems, Probabilistic Engineering Mechanics 43 (2016) 68–84. 19

[60] A. Gelman, J. B. Carlin, H. S. Stern, D. B. Rubin, Bayesian Data Analysis, third edition Edition, Vol. 2, Chapman & Hall/CRC Boca Raton, FL, USA, 2014. 20, 99

[61] A. M. Stuart, Inverse problems: a Bayesian perspective, Acta Numerica 19 (2010) 451–559. 20

[62] J. L. Beck, L. S. Katafygiotis, Updating Models and Their Uncertainties. I: Bayesian Statistical Framework, Journal of Engineering Mechanics 124 (4) (1998) 455–461. `doi:10.1061/(ASCE)0733-9399(1998)124:4(455)`. 20

[63] W. R. Gilks, S. Richardson, D. Spiegelhalter, Markov chain Monte Carlo in practice, Chapman and Hall/CRC, 1995. 21

[64] P. Green, K. Worden, Bayesian and Markov Chain Monte Carlo Methods for Identifying Nonlinear systems in The Presence of Uncertainty, Phil. Trans. R. Soc. A 373 (2051) (2015) 20140405. `doi:10.1098/rsta.2014.0405`. 21, 23

[65] W. K. Hastings, Monte Carlo sampling methods using Markov chains and their applications, Biometrika 57 (1970) 97–109. 21

[66] S. Chib, E. Greenberg, Understanding the Metropolis-Hastings algorithm, The American statistician 49 (4) (1995) 327–335. 22

[67] F. Liang, C. Liu, R. Carroll, Advanced Markov Chain Monte Carlo methods: learning from past samples, Vol. 714, John Wiley & Sons, 2011. 23

[68] P. Congdon, Bayesian statistical modelling, Vol. 704, John Wiley & Sons, 2007. 23

[69] J. L. Beck, S.-K. Au, Bayesian updating of structural models and reliability using Markov Chain Monte Carlo simulation, Journal of engineering mechanics 128 (4) (2002) 380–391. 23

[70] J. Ching, Y.-C. Chen, Transitional Markov Chain Monte Carlo Methods for Bayesian Model Updating, Model Class Selection, and Model Averaging, Journal of engineering mechanics 133 (7) (2007) 816–832. `doi:10.1061/(ASCE)0733-9399(2007)133:7(816)`. 23, 24

REFERENCES

[71] S. H. Cheung, J. L. Beck, Bayesian model updating using hybrid Monte Carlo simulation with application to structural dynamic models with many uncertain parameters, Journal of engineering mechanics 135 (4) (2009) 243–255. 24

[72] W. Betz, I. Papaioannou, D. Straub, Transitional Markov Chain Monte Carlo: observations and improvements, Journal of Engineering Mechanics 142 (5) (2016) 04016016. 24, 25

[73] P. Angelikopoulos, C. Papadimitriou, P. Koumoutsakos, X-TMCMC: Adaptive kriging for Bayesian inverse modeling, Computer Methods in Applied Mechanics and Engineering 289 (2015) 409–428. 25

[74] C. R. Farrar, K. Worden, Structural Health Monitoring.: A Machine Learning Perspective, John Wiley & Sons, 2012. `doi:10.1002/9781118443118`. 27, 28, 31, 38

[75] J.-A. Goulet, A. Der Kiureghian, B. Li, Pre-posterior optimization of sequence of measurement and intervention actions under structural reliability constraint, Structural Safety 52 (2015) 1–9. `doi:10.1016/j.strusafe.2014.08.001`. 27

[76] G. Song, C. Wang, B. Wang, Structural health monitoring (SHM) of civil structures, Multidisciplinary Digital Publishing Institute, 2017. `doi:10.3390/app7080789`. 27

[77] S. Akhtar, Review of nondestructive testing methods for condition monitoring of concrete structures, Journal of construction engineering 2013. `doi:0.1155/2013/834572`. 27

[78] P. C. Chang, S. C. Liu, Recent research in nondestructive evaluation of civil infrastructures, Journal of materials in civil engineering 15 (3) (2003) 298–304. 27

[79] B. Li, Uncertainty quantification in vibration-based structural health monitoring using bayesian statistics, Ph.D. thesis, UC Berkeley (2016). 27, 31

[80] S. Doebling, C. Farrar, M. Prime, D. Shevitz, Damage identification and health monitoring of structural and mechanical systems from changes in their vibration characteristics: A literature review.`doi:10.2172/249299`. 27, 30, 31

[81] J. X. Yan, C. S. Liu, T. Z. Liu, L. L. Zhao, A review on advances of damage identification methods based on vibration, in: Key Engineering Materials, Vol. 413, Trans Tech Publ, 2009, pp. 277–283. `doi:10.4028/www.scientific.net/KEM.413-414.277`. 27, 31, 32

REFERENCES

[82] Y. An, E. Chatzi, S.-H. Sim, S. Laflamme, B. Blachowski, J. Ou, Recent progress and future trends on damage identification methods for bridge structures, Structural Control and Health Monitoring 26 (10) (2019) e2416. `doi:10.1002/stc.2416`. 27, 34

[83] P. C. Chang, A. Flatau, S. Liu, Health monitoring of civil infrastructure, Structural health monitoring 2 (3) (2003) 257–267. 28

[84] A. Rytter, Vibrational based inspection of civil engineering structures, Ph.D. thesis, Denmark, ph.D.-Thesis defended publicly at the University of Aalborg, April 20, 1993: 206 pp. (1993). 28, 30

[85] G. Rajan, B. G. Prusty, Structural health monitoring of composite structures using fiber optic methods, CRC press, 2016. 28, 127

[86] C. R. Farrar, K. Worden, New trends in vibration based structural health monitoring, CISM Courses and Lectures, Springer Science & Business Media, 2012, Ch. An Introduction to Structural Health Monitoring, pp. 1–18. 28

[87] D. J. Ewins, Modal testing: theory and practice, 2nd Edition, Vol. 15, Research studies press Letchworth, 2000. 28

[88] K. G. McConnell, P. S. Varoto, Vibration testing: theory and practice, 2nd Edition, John Wiley & Sons, 2008. 28

[89] R. Brincker, C. Ventura, Introduction to operational modal analysis, John Wiley & Sons, 2015. 28

[90] W. Heylen, S. Lammens, P. Sas, et al., Modal analysis theory and testing, Vol. 200, Katholieke Universiteit Leuven Leuven, Belgium, 1997. 29

[91] L. Zhang, R. Brincker, An overview of operational modal analysis: Major development and issues, 2005. 29

[92] H. Sohn, C. R. Farrar, F. M. Hemez, J. J. Czarnecki, A review of structural health review of structural health monitoring literature 1996-2001. 29, 30, 31, 33, 127

[93] R. J. Barthorpe, On model-and data-based approaches to structural health monitoring, Ph.D. thesis, University of Sheffield (2010). 29

[94] X. Kong, C.-S. Cai, J. Hu, The state-of-the-art on framework of vibration-based structural damage identification for decision making, Applied Sciences 7 (5) (2017) 497. `doi:doi.org/10.3390/app7050497`. 29

REFERENCES

[95] I. Gonzalez, R. Karoumi, Bwim aided damage detection in bridges using machine learning, Journal of Civil Structural Health Monitoring 5 (5) (2015) 715–725. `doi: 10.1007/s13349-015-0137-4`.
URL `https://doi.org/10.1007/s13349-015-0137-4` 29

[96] A. C. Neves, I. González, J. Leander, R. Karoumi, Structural health monitoring of bridges: a model-free ann-based approach to damage detection, Journal of Civil Structural Health Monitoring 7 (5) (2017) 689–702. `doi:10.1007/s13349-017-0252-5`.
URL `https://doi.org/10.1007/s13349-017-0252-5` 29

[97] C. M. Bishop, Pattern recognition and machine learning, springer, 2006. 29

[98] K. Worden, New trends in vibration based structural health monitoring, CISM Courses and Lectures, Springer Science & Business Media, 2012, Ch. Structural Health Monitoring using Pattern Recognition, pp. 183–246. 29

[99] C. M. Bishop, Novelty detection and neural network validation, IEE Proceedings-Vision, Image and Signal processing 141 (4) (1994) 217–222. 29

[100] K. Worden, G. Manson, N. R. Fieller, Damage detection using outlier analysis, Journal of Sound and Vibration 229 (3) (2000) 647–667. `doi:10.1006/jsvi.1999.2514`. 29

[101] D. C. Montgomery, Introduction to statistical quality control, 6th Edition, John Wiley & Sons, 2009. 29

[102] J. Kullaa, New trends in vibration based structural health monitoring, CISM Courses and Lectures, Springer Science & Business Media, 2012, Ch. Vibration-Based Structural Health Monitoring Under Variable Environmental or Operational Conditions, pp. 107–182. 29, 50

[103] A. Deraemaeker, E. Reynders, G. De Roeck, J. Kullaa, Vibration-based structural health monitoring using output-only measurements under changing environment, Mechanical systems and signal processing 22 (1) (2008) 34–56. `doi:10.1016/j.ymssp. 2007.07.004`. 29

[104] K. Worden, G. Manson, The application of machine learning to structural health monitoring, Philosophical Transactions of the Royal Society A: Mathematical, Physical and Engineering Sciences 365 (1851) (2006) 515–537. `doi:10.1098/rsta.2006.1938`. 29

[105] D. Balageas, C.-P. Fritzen, A. Güemes, Structural health monitoring, Vol. 90, John Wiley & Sons, 2010. `doi:10.1002/9780470612071`. 30

REFERENCES

[106] A. K. Tangirala, Principles of system identification: theory and practice, Crc Press, 2014. 30

[107] M. Friswell, J. E. Mottershead, Finite element model updating in structural dynamics, Vol. 38, Springer Science & Business Media, 1995. `doi:10.1007/978-94-015-8508-8`. 30

[108] H.-P. Chen, Y.-Q. Ni, Structural health monitoring of large civil engineering structures, Wiley Online Library, 2018. 30, 32, 127

[109] M. Masjedian, M. Keshmiri, A review on operational modal analysis researches: classification of methods and applications, 2009, pp. 707–718. 30

[110] R. Brincker, L. Zhang, P. Andersen, Modal identification of output-only systems using frequency domain decomposition, Smart materials and structures 10 (3) (2001) 441. `doi:10.1088/0964-1726/10/3/303`. 30

[111] P. Van Overschee, B. De Moor, Subspace algorithms for the stochastic identification problem, Automatica 29 (3) (1993) 649–660. `doi:10.1016/0005-1098(93)90061-W`. 30, 34

[112] B. Peeters, G. De Roeck, Stochastic System Identification for Operational Modal Analysis: A Review , Journal of Dynamic Systems, Measurement, and Control 123 (4) (2001) 659–667. `doi:10.1115/1.1410370`. 30

[113] V. Gattulli, Implementation of identification methodologies on large-scale structures, in: Identification Methods for Structural Health Monitoring, Springer, 2016, pp. 1–34. `doi:10.1007/978-3-319-32077-9`. 31

[114] E. Simoen, G. Lombaert, Bayesian Parameter Estimation, Springer International Publishing, Cham, 2016, pp. 89–115. `doi:10.1007/978-3-319-32077-9_4`. 31

[115] M. W. Vanik, J. L. Beck, S.-K. Au, Bayesian probabilistic approach to structural health monitoring, Journal of Engineering Mechanics 126 (7) (2000) 738–745. `doi:10.1061/(ASCE)0733-9399(2000)126:7(738)`. 31

[116] S. K. Au, Bayesian Operational Modal Analysis, Springer International Publishing, Cham, 2016, pp. 117–135. `doi:10.1007/978-3-319-32077-9_5`. 31

[117] C. Papadimitriou, Bayesian Uncertainty Quantification and Propagation: State-of-the-Art Tools for Linear and Nonlinear Structural Dynamics Models, Springer International Publishing, Cham, 2016, pp. 137–170. `doi:10.1007/978-3-319-32077-9_6`. 31

REFERENCES

[118] J. Ching, M. Muto, J. L. Beck, Structural model updating and health monitoring with incomplete modal data using gibbs sampler, Computer-Aided Civil and Infrastructure Engineering 21 (4) (2006) 242–257. 31

[119] Y. Huang, C. Shao, B. Wu, J. L. Beck, H. Li, State-of-the-art review on bayesian inference in structural system identification and damage assessment, Advances in Structural Engineering 22 (6) (2019) 1329–1351. arXiv:https://doi.org/10.1177/1369433218811540, doi:10.1177/1369433218811540. 31

[120] M. Liggins II, D. Hall, J. Llinas, Handbook of multisensor data fusion: theory and practice, CRC press, 2001. 31

[121] J. R. Raol, Multi-sensor data fusion with MATLAB, CRC press, 2009. 31

[122] A. W. Smyth, T. Kontoroupi, P. T. Brewick, Efficient Data Fusion and Practical Considerations for Structural Identification, Springer International Publishing, Cham, 2016, pp. 35–49. doi:10.1007/978-3-319-32077-9_2. 31

[123] H. Guo, Structural damage detection using information fusion technique, Mechanical Systems and Signal Processing 20 (5) (2006) 1173–1188. doi:10.1016/j.ymssp.2005.02.006. 31

[124] Y. Bao, Y. Xia, H. Li, Y.-L. Xu, P. Zhang, Data fusion-based structural damage detection under varying temperature conditions, International journal of structural stability and dynamics 12 (06) (2012) 1250052. doi:10.1142/S0219455412500526. 31

[125] G. Sha, M. Cao, W. Xu, D. Novák, Structural damage identification using multiple mode fusion curvature mode shape method, in: Structural Health Monitoring and Integrity Management: Proceedings of the 2nd International Conference of Structural Health Monitoring and Integrity Management (ICSHMIM 2014), Nanjing, China, 24-26 September 2014, CRC Press, 2015, p. 163. 31, 34, 52

[126] S. W. Doebling, C. R. Farrar, M. B. Prime, et al., A summary review of vibration-based damage identification methods, Shock and vibration digest 30 (2) (1998) 91–105. 31, 32

[127] J. J. Moughty, J. R. Casas, A state of the art review of modal-based damage detection in bridges: development, challenges, and solutions, Applied Sciences 7 (5) (2017) 510. doi:10.3390/app7050510. 31, 34

REFERENCES

[128] E. Reynders, G. De Roeck, Vibration-based damage identification: The z24 bridge benchmark, Encyclopedia of earthquake engineering 482 (2014) 1–8. `doi:10.1007/978-3-642-36197-5_72-1`. 32

[129] G. Sha, M. Radzieński, M. Cao, W. Ostachowicz, A novel method for single and multiple damage detection in beams using relative natural frequency changes, Mechanical Systems and Signal Processing 132 (2019) 335–352. `doi:10.1016/j.ymssp.2019.06.027`. 32

[130] W. M. West, Illustration of the use of modal assurance criterion to detect structural changes in an orbiter test specimen, 1986. 33

[131] Y. L. Xu, Y. Xia, Structural health monitoring of long-span suspension bridges, 1st Edition, CRC Press, 2011. 33

[132] A. Pandey, M. Biswas, M. Samman, Damage detection from changes in curvature mode shapes, Journal of sound and vibration 145 (2) (1991) 321–332. `doi:10.1016/0022-460X(91)90595-B`. 33

[133] D. Capecchi, J. Ciambella, A. L. Pau, F. Vestroni, Damage identification in a parabolic arch by means of natural frequencies, modal shapes and curvatures, Meccanica 51 (2016) 2847–2859. `doi:10.1007/s11012-016-0510-3`. 34

[134] R. Brincker, P. Andersen, Understanding Stochastic Subspace Identification, 2006, pp. 279–311. 35

[135] E. Reynders, K. Maes, G. Lombaert, G. De Roeck, Uncertainty quantification in operational modal analysis with stochastic subspace identification: validation and applications, Mechanical Systems and Signal Processing 66 (2016) 13–30. `doi:10.1016/j.ymssp.2015.04.018`. 35

[136] B. Peeters, G. De Roeck, Reference-based stochastic subspace identification for output-only modal analysis, Mechanical systems and signal processing 13 (6) (1999) 855–878. `doi:10.1006/mssp.1999.1249`. 35

[137] P. Van Overschee, B. De Moor, Subspace identification for linear systems: Theory—Implementation—Applications, Springer Science & Business Media, 2012. 35

[138] Y.-C. Liu, C.-H. Loh, Y.-Q. Ni, Stochastic subspace identification for output-only modal analysis: application to super high-rise tower under abnormal loading condition, Earthquake Engineering & Structural Dynamics 42 (4) (2013) 477–498. `doi:10.1002/eqe.2223`. 36

REFERENCES

[139] T. Giannakopoulos, A. Pikrakis, Introduction to audio analysis: a MATLAB® approach, Academic Press, 2014. 36

[140] J. C. Santamarina, D. Fratta, Discrete signals and inverse problems, An Introduction for Engineers and Scientists. UK: Wiley & Sons. 37

[141] E. Layer, K. Tomczyk, Signal transforms in dynamic measurements, Springer, 2015. `doi:10.1007/978-3-319-13209-9`. 37, 39

[142] F. Alkam, I. Pereira, T. Lahmer, Qualitatively-improved identified parameters of pre-stressed concrete catenary poles using sensitivity-based bayesian approach, Results in Engineering 6 (2020) 100104. `doi:https://doi.org/10.1016/j.rineng.2020.100104`. 46, 47, 48, 101

[143] J. Patterson, A. Gibson, Deep learning: A practitioner's approach, " O'Reilly Media, Inc.", 2017. 50

[144] F. Alkam, T. Lahmer, Eigenfrequency-based bayesian approach for damage identification in catenary poles, Infrastructures 6 (4). `doi:10.3390/infrastructures6040057`. 51, 52, 115, 116, 117

[145] M. Liggins, D. Hall, J. Llinas, Handbook of Multisensor Data Fusion: Theory and Practice, Second Edition, Electrical Engineering & Applied Signal Processing Series, Taylor & Francis, 2008. 52

[146] F. H. Fouad, D. Sherman, R. J. Werner, Spun prestressed concrete poles–past, present, and future, Concrete international 14 (11) (1992) 25–29. 55

[147] C. Müller, M. Empelmann, F. Hude, T. Adam, Schleuderbetonstützen aus hochfester bewehrung und ultrahochfestem beton: Anlässlich des 475-jahr-jubiläums des stahlwerks annahütte, Beton-und Stahlbetonbau 107 (10) (2012) 690–699. 55

[148] F. H. Fouad, R. J. Detwiler, High-strength materials for spun concrete poles., PCI Journal 57 (3) (2012) 27–32. 55

[149] M. E. Kuebler, Torsion in helically reinforced prestressed concrete poles, Master's thesis, University of Waterloo (2008). 55

[150] M. Kuebler, M. A. Polak, Torsion tests on spun-cast prestressed concrete poles, PCI journal 57 (2) (2012) 120–141. 55

[151] PCI Committee on Prestressed Concrete Poles, Guide for the design of prestressed concrete poles, PCI Journal 42 (6) (1997) 94–34. 56

REFERENCES

[152] DIN EN 12843:2004-11, Precast concrete products - masts and poles; german version EN 12843:2004, Standard, Deutsche Institut für Normung e.V., Berlin, Germany (Nov. 2004). 56

[153] F. H. Fouad, N. L. Scott, E. Calvert, M. Donovan, Performance of spun prestressed concrete poles during hurricane andrew, PCI journal 39 (2) (1994) 102–110. `doi: 10.15554/pcij.03011994.102.110`. 56

[154] A. M. Ibrahim, Behaviour of pre-stressed concrete transmission poles under high intensity wind, Ph.D. thesis, University of Western Ontario (2017). 56

[155] W. H. Dilger, A. Ghali, S. Mohan Rao, Improving durability and performance of spun-cast concrete poles, PCI journal 41 (2) (1996) 68–90. `doi:10.15554/pcij.03011996. 68.90`. 56

[156] M. Wichert, J. Remitz, M. Empelmann, Ultra-high performance spun concrete poles– part II: Tests on grouted pole joints, Proceedings of HPC/CIC 2017 (Paper no. 55). 56

[157] S. Chen, C. K. Ong, K. Antonsson, Modal behaviors of spun-cast pre-stressed concrete pole structures, Proceeding of IMAC–XXIV (2006) 1831–1836. 56

[158] S.-E. Chen, K. Dai, Modal characteristics of two operating power transmission poles, Shock and Vibration 17 (4, 5) (2010) 551–561. 56

[159] K. Dai, S. Chen, D. Smith, Vibration analyses of electrical transmission spun-cast concrete poles for health monitoring, in: Nondestructive Characterization for Composite Materials, Aerospace Engineering, Civil Infrastructure, and Homeland Security 2012, Vol. 8347, International Society for Optics and Photonics, 2012, p. 834702. 56

[160] G. Kouroussis, O. Verlinden, D. P. Connolly, M. C. Forde, Estimation of railway vehicle speed using ground vibration measurements, 21st International Congress on Sound and Vibration (ICSV21), Beijing, China, 2014, pp. 1–8. 57

[161] D. Connolly, G. Kouroussis, P. Woodward, P. A. Costa, O. Verlinden, M. Forde, Field testing and analysis of high speed rail vibrations, Soil Dynamics and Earthquake Engineering 67 (2014) 102–118. 57

[162] D. Connolly, G. Kouroussis, O. Laghrouche, C. Ho, M. Forde, Benchmarking Railway Vibrations–track, Vehicle, Ground and Building Effects, Construction and Building Materials 92 (2015) 64–81. `doi:10.1016/j.conbuildmat.2014.07.042`. 57

REFERENCES

[163] P. Ampunant, F. Kemper, I. Mangerig, M. Feldmann, Train–induced aerodynamic pressure and its effect on noise protection walls, in: A. Cunha, E. Caetano, P. Ribeiro, G. Müller (Eds.), 9th International Conference on Structural Dynamics, EURODYN 2014, 2014, pp. 3739–3743, ISBN: 978-972-752-165-4. 57

[164] O. V. Van, J.-P. Massat, E. Balmes, Waves, modes and properties with a major impact on dynamic pantograph-catenary interaction, Journal of Sound and Vibration 402 (2017) 51–69. 57

[165] J. Pombo, J. Ambrósio, Influence of pantograph suspension characteristics on the contact quality with the catenary for high speed trains, Computers & Structures 110 (2012) 32–42. 57

[166] L. Göbel, F. Mucha, I. Kavrakov, L. Abrahamczyk, M. Kraus, Einfluss realer Materialeigenschaften auf numerische Modellvorhersagen: Fallstudie Betonmast, Bautechnik 95 (1) (2018) 111–122. `doi:10.1002/bate.201600091`. 58

[167] L. Abrahamczyk, F. Alkam, A. H. Hisham, L. Göbel, Z. Jaouadi, M. Kraus, I. Kavrakov, D. Legatiuk, F. Mucha, S. Rau, GRK 1462 - Reference Project "poles": monitoring system, lab experiments and long-term measurements, in: L. Abrahamczyk, D. Legatiuk, F. Werner (Eds.), GRK 1462 International Workshop 2017. 26th - 28th April. Coupled Numerical and Experimental Models in Structural Engineering, Weimar, Germany, 2017, ISBN: 978-3-95773-239-2. 58

[168] M. Deeb, Relibility of vibration-based nonstructive inspection methods for damage detection in structural engineering, Ph.D. thesis, Bauhaus-Universität Weimar, Weimar, Germany (May 2018). 58

[169] L. Göbel, F. Mucha, Z. Jaouadi, I. Kavrakov, D. Legatiuk, L. Abrahamczyk, M. Kraus, K. Smarsly, Monitoring the structural response of reinforced concrete poles along high-speed railway tracks, in: Proceedings International RILEM Conference on Materials, Systems and Structures in Civil Engineering–Conference segment on Reliability, Technical University of Denmark Lyngby, Denmark, 2016, pp. 1–10. 58, 73

[170] L. Abrahamczyk, Z. Jaouadi, U. Kähler, D. Legatiuk, Methoden zur Identifikation von Zugvorbeifahrten aus kontinuierlichen Messdaten, Bautechnik 95 (7) (2018) 485–493. `doi:10.1002/bate.201700115`. 58

[171] E. Reynders, M. Schevenels, G. De Roeck, Macec 3.3: A matlab toolbox for experimental and operational modal analysis. 61

REFERENCES

[172] D. Halpern, H. B. Wilson, L. H. Turcotte, Advanced mathematics and mechanics applications using MATLAB, Chapman and Hall/CRC, 2002. 61

[173] E. Bentz, M. P. Collins, Response-2000 Manual, [Accessed 05 March 2019].
URL http://www.ecf.utoronto.ca/~bentz/r2k.htm 62

[174] Versuchstechnische Einrichtung (VTE), Versuchsdokumentation ICE-Neubaustrecke vde 8.2 bei oberklobikau - Teil 1, Tech. rep., Bauhaus-Universität Weimar (June 2014). 73

[175] H. B. Motra, Quality assessment methods for experimental models in structural engineering, Ph.D. thesis, Bauhaus-Universität Weimar, Weimar, Germany, ISBN: 978-3-95773-196-8 (June 2015). 73

[176] MATLAB, version 9.2.0 (R2017a), The MathWorks Inc., Natick, Massachusetts, 2017. 74

[177] J. Lubliner, J. Oliver, S. Oller, V. Oñate, A plastic-damage model for concrete, International Journal of Solids and Structures 25 (3) (1989) 299–326. doi:10.1016/0020-7683(89)90050-4. 75

[178] M. Batikha, F. Alkam, The Effect of Mechanical Properties of Masonry on the behavior of FRP-strengthened Masonry-infilled RC Frame under Cyclic Load, Composite Structures 134 (2015) 513–522. doi:10.1016/j.compstruct.2015.08.105. 75

[179] ABAQUS/Standard User's Manual, Version 6.9, Dassault Systèmes Simulia Corp, United States, 2017. 76

[180] Prysmian Group, Railway Main Line Cables, electronically, Pikkala, Finland (2019).
URL https://www.prysmiangroup.com/ 78

[181] PFISTERER, Railway Catenary Systems - Solutions for Overhead Line, electronically, Winterbach, Germany (2016).
URL https://www.pfisterer.com/ 78

[182] elcowire, OVERHEAD CATENARY WIRE, electronically, Mannheim, Germany (2017).
URL https://www.elcowire.com/ 78

[183] E. Costello, Length of a hanging cable, Undergraduate Journal of Mathematical Modeling 4 (1) (2011) 4. doi:10.5038/2326-3652.4.1.4. 78

[184] W.-X. Ren, M.-G. Huang, W.-H. Hu, A parabolic cable element for static analysis of cable structures, Engineering Computations 25 (4) (2008) 366–384. 78

[185] P. Broughton, P. Ndumbaro, The analysis of cable and catenary structures, Thomas Telford, 1994. 78

[186] R. D. Blevins, Formulas for Dynamics, Acoustics and Vibration, John Wiley & Sons, Ltd, 2015. `doi:10.1002/9781119038122`. 100

[187] J. Hu, R. Y. Liang, An integrated approach to detection of cracks using vibration characteristics, Journal of the Franklin Institute 330 (5) (1993) 841–853. 110

[188] I. Reichert, P. Olney, T. Lahmer, Influence of the error description on model-based design of experiments, Engineering Structures 193 (2019) 100–109. 127

[189] P. Romano, P. Brito, Degradation monitoring systems for a bim maintenance approach, in: Sustainable Construction and Building Materials, IntechOpen, 2018. `doi:10.5772/intechopen.81433`. 128

[190] E. Schäfer, RFID-Sensortransponder für Industrieanwendungen, [Accessed 21 October 2019] (2019).
URL `https://www.elmug.de/assets/elmug4future-2019/` 128

Ehrenwörtliche Erklärung

Ich erkläre hiermit ehrenwörtlich, dass ich die vorliegende Arbeit ohne unzulässige Hilfe Dritter und ohne Benutzung anderer als der angegebenen Hilfsmittel angefertigt habe. Die aus anderen Quellen direkt oder indirekt übernommenen Daten und Konzepte sind unter Angabe der Quelle gekennzeichnet.

Weitere Personen waren an der inhaltlich-materiellen Erstellung der vorliegenden Arbeit nicht beteiligt. Insbesondere habe ich hierfür nicht die entgeltliche Hilfe von Vermittlungs- bzw. Beratungsdiensten (Promotionsberater oder anderer Personen) in Anspruch genommen. Niemand hat von mir unmittelbar oder mittelbar geldwerte Leistungen für Arbeiten erhalten, die im Zusammenhang mit dem Inhalt der vorgelegten Dissertation stehen.

Die Arbeit wurde bisher weder im In- noch im Ausland in gleicher oder ähnlicher Form einer anderen Prüfungsbehörde vorgelegt.

Ich versichere ehrenwörtlich, dass ich nach bestem Wissen die reine Wahrheit gesagt und nichts verschwiegen habe.

Weimar, 01 April 2020

Feras Alkam

Academic Curriculum Vitae

Feras Alkam

Institute of Structural Mechanics

Bauhaus-Universität Weimar

Marienstraße 15, 99423 Weimar, Germany

Email: feras.alkam@uni-weimar.de

Date of Birth: May 08$^{\text{th}}$, 1977

Place of Birth: Damascus, Syria

Education

- Ph.D: Institute of Structural Mechanics, Bauhaus-University Weimar, Germany, 2015 – 2020.

- M.Sc.: Master in Structural Engineering, Damascus University, Syria, 2012 – 2014.

- Dipl.-Ing.: Diploma in Structural Engineering, Damascus University, Syria, 2000 – 2001.

- B.Sc.: Bachelor in Structural Engineering, Damascus University, Syria, 1995 – 1999.

Research Interests

- Uncertainty quantification, Bayesian inference, Damage detection, Structural health monitoring, Machine learning, Bridge design and monitoring

Publications

Accepted/Published International Journals (PhD Study)

1. F. Alkam, T. Lahmer, Eigenfrequency-based bayesian approach for damage identification in catenary poles, Infrastructures 6 (4) (2021) 57. doi:10.3390/infrastructures6040057.

2. F. Alkam, I. Pereira, T. Lahmer, Qualitatively-improved identified parameters of pre-stressed concrete catenary poles using sensitivity-based bayesian approach, Results in Engineering 6 (2020) 100104. doi:10.1016/j.rineng.2020.100104.

3. F. Alkam, T. Lahmer, Quantifying the uncertainty of identificationed parameters of prestressed concrete poles using the experimental measurements and different optimization methods, Engineering and Applied Sciences 4 (4) (2019) 84. doi:10.11648/j.eas.20190404.13.

Published International Journals (Master Study)

1. M. Batikha; F. Alkam, The Effect of Mechanical Properties of Masonry on the behavior of FRP-strengthened Masonry-infilled RC Frame under Cyclic Load, Composite Structures 134 (2015) 513–522. doi:10.1016/j.compstruct.2015.08.105

International Conference/Workshop Publications

1. F. Alkam; T. Lahmer, On the quality of identified parameters of prestressed concrete catenary poles in existence of uncertainty using experimental measurements and different optimization methods, in Proceedings of ISMA2018 & USD2018, KU Leuven, Belgium, 2018, pp. 3913–3923.

2. F. Alkam; T. Lahmer, Solving non-uniqueness issues in parameter identification problems for pre-stressed concrete poles by multiple Bayesian updating, in Proceedings of the 15th International Probabilistic Workshop & 10th Dresdner Probabilistic Workshop, TUDpress, 2017, pp. 303–315.

3. L. Abrahamczyk; F. Alkam; A. H. Hisham; L. Göbel; Z. Jaouadi; M. Kraus; I. Kavrakov; D. Legatiuk; F. Mucha; S. Rau, GRK 1462 - Reference Project "poles": monitoring system, lab experiments and long-term measurements, in: GRK 1462 International Workshop 2017. 26th - 28th April, Weimar, Germany, 2017, ISBN: 978-3-95773-239-2.

Presentations

1. F. Alkam; T. Lahmer, Bayesian Inference for solving Inverse Problems, PhD Course "Applied and Computational Mathematics in Engineering Application", Aveiro, Portugal, 2018

2. F. Alkam; T. Lahmer, Solving Non-Uniqueness Issues in Parameter Identification problems for Pre-stressed Concrete Poles by Multiple Bayesian Updating, SAMM 2017, Braunschweig, Germany, 2017.

3. F. Alkam; L. Göbel; A. H. Hisham; S. Rau., On the Quality of Material Parameters Obtained by Different Identification Approaches, Graduiertenkolleg 1462, Bauhaus-Universität Weimar, Germany, 2017.

Last updated: April 13, 2021